

UNIVERSITÄT
BAYREUTH

Lehrstuhl für Kristallographie

Characterization of phase transitions by the analysis of crystal structures

Abhandlung zur Erlangung des akademischen Grades eines
Doktors der Naturwissenschaften

vorgelegt von
Joachim Angelkort

1. Gutachter: Prof. Dr. Sander van Smaalen
2. Gutachter: Prof. Dr. Hans F. Braun

Tag der Einreichung: 15. Juli 2009
Tag des Kolloquiums: 18. Dezember 2009

Danksagung

Ich danke Prof. Dr. van Smaalen für die Möglichkeit, am Lehrstuhl für Kristallographie an spannenden Projekten mitgearbeiten haben zu dürfen. Er stand jederzeit für Diskussionen und Beratungen zur Seite. Sein Engagement sowie sein hoher Anspruch an den Einsatz seiner Mitarbeiter trugen wesentlich zum Gelingen der durchgeführten Experimente bei.

Ein großes Dankeschön gilt Dr. Schönleber, der an der Betreuung der Doktoranden des Lehrstuhls Teil hatte. Viele Diskussionen mit ihm führten zu einem besseren Verständnis kristallographischer Sachverhalte.

Ich danke Alfred Suttner für die Synthese von Kristallen und Franz Fischer für die fortlaufende Reparatur und Instandhaltung der technischen Geräte, deren Eigenleben ihn oft zur Entwicklung von unkonventionellen, gut funktionierenden Methoden veranlasste.

Weiterhin danke ich allen derzeitigen und einstigen Mitarbeitern des Institutes, die für ein angenehmes und fast familiäres Arbeitsklima gesorgt haben.

Meiner Mutter und meinem Bruder

Contents

1	Introduction	1
2	Theoretical background	5
2.1	Theory of structural phase transitions in crystals	5
2.1.1	Continuous phase transitions	6
2.1.2	Discontinuous phase transitions	7
2.2	The spin-Peierls transition	9
3	Experimental techniques	11
3.1	Generation of X-ray radiation	11
3.1.1	Conventional X-ray radiation	11
3.1.2	Synchrotron radiation	12
3.1.3	Monochromatization	13
3.2	Single-crystal X-ray Diffractometers	14
3.2.1	Experiments on a Mach3 diffractometer	18
3.2.2	Experiments on a MAR345 dtb diffractometer	20
3.3	Control of the crystal temperature	20
3.4	Crystal preparation	22
4	Crystal chemistry of selected transition-metal compounds	25
4.1	The transition-metal trihalides	25
4.1.1	Phase transitions of α -TiX ₃ (X = Cl, Br)	27
4.1.2	Phase transition of β -TiX ₃ (X = Cl, Br, I)	28
4.2	The transition-metal oxyhalides	29
4.2.1	Crystal structures and magnetic behavior	29
4.2.2	Phase transitions of TiOCl and TiOBr	31
4.2.3	Magnetic structures of FeOCl, CrOCl and VOCl	32

5	Phase transition and crystal structure of the monomeric Europium(II) thiolate $\text{Eu}(\text{SC}_{36}\text{H}_{49})_2$	35
5.1	Introduction	35
5.2	Results and Discussion	36
5.3	Conclusions	44
5.4	Experimental Section	44
6	Low- and high-temperature crystal structures of TiI_3	47
6.1	Introduction	47
6.2	Experimental section	51
6.3	Structure refinements	53
6.4	Discussion	56
6.4.1	TiI_3 and RuBr_3 structure types	56
6.4.2	The phase transition	60
6.5	Conclusions	61
7	Magnetoelastic coupling in CrOCl	63
7.1	Introduction	63
7.2	Experimental	65
7.3	Results	66
7.3.1	Magnetic Susceptibility and magnetization	66
7.3.2	X-ray diffraction	69
7.4	Discussion	73
7.5	Conclusions	76
8	Inhomogeneous thermal expansion of layered CrOCl	77
8.1	Introduction	77
8.2	Experimental	79
8.3	Discussion	81
9	Summary	83
10	Zusammenfassung	87
A	Supplementary material: $\text{Eu}(\text{SC}_{36}\text{H}_{49})_2$	91
B	Supplementary material: TiI_3	101

C	Crystal twinning of TiI_3	103
D	Monoclinic angle in the unit cell of CrOCl	105
E	Measured reflection profiles of CrOCl	107
E.1	Profiles of 2θ -dependent ω -scans	108
E.1.1	Profiles measured on reflection (0 -2 5)	108
E.1.2	Profiles measured on reflection (2 0 4)	110
E.1.3	Profiles measured on reflection (2 -2 0)	112
E.2	Scans on superstructure reflections of CrOCl	114
E.3	Profile fitting for determination of the peak positions of CrOCl	117
F	Additional structural parameters of CrOCl at different temperatures	119
	Bibliography	123
	Parts of this thesis published in the scientific literature	133
	List of Figures	137
	List of Tables	140
	Erklärung	141

Chapter 1

Introduction

Symmetry is a property of one or several objects by which the geometrical shape of the object or the geometrical interrelation between the objects is described. In the case of a crystal structure the symmetry interrelates equal kinds of atoms to be located at certain positions in space. One uses the term pseudo symmetry to refer to a crystal structure which does not differ much from a structure with a higher symmetry. The existence of a pseudo symmetry can be revealed by the finding that the examined lattice parameters of the unit cell are in conflict with the demands of the underlying symmetry or by the indication that some atoms of the structure are displaced contradictory to the supposed symmetry.

Often the atoms of a particular chemical compound can be arranged to different crystal structures giving rise to the formation of different stable phases. A phase is a volume of matter which is physically and chemically homogeneous and which can be assigned to one of the three states (gaseous, liquid, solid). Changes of system parameters like pressure and temperature can cause a transformation of one state of matter into another termed phase transition. In contrast to the gaseous state in which any combination of gases forms a homogeneous mixture, i.e. a single phase, different phases can coexist in liquids as well as in the solid state. The gaseous and liquid phases are states of highest symmetry, while the crystalline state can have different symmetries according to one of the 230 space groups. Additional possibilities occur for the so-called aperiodic crystals. Phase transitions between different solid states can be continuous or discontinuous (Chapter 2). At the transition point of a discontinuous phase transitions different phases coexist. In this thesis the term domain is used to indicate a small block in a large piece of matter, which is in one of several states or which possesses one of several orientations

of the lattice of a particular phase.

This thesis deals with the analysis of crystal structures of selected compounds, their temperature-dependent changes and the interpretation of these changes with respect to the occurrence of solid state phase transitions. The investigated crystal structures were studied by means of single-crystal X-ray diffraction experiments carried out on several inorganic compounds of the first row transition elements and on one organometallic compound. Crystal structures at different temperatures define the structural changes caused by the phase transitions and provide information about the transition mechanisms.

The multitude of crystallite orientations in X-ray powder diffraction (XRPD) experiments allow a measurement of the reflection intensities just through a variation of the detector position along the scattering angle 2θ . In single-crystal X-ray diffraction (SXRD) experiments, however, a reflection can only be measured if the position of the detector and the crystal orientation simultaneously fulfill the reflection condition. The additional degrees of freedom in SXRD experiments arising from the ability to orient the single-crystal in the three dimensions of space allow to determine reflection intensities of different reflections separately even if they occur at the same scattering angle and would, thus, coincide in XRPD diagrams. The comparison of reflection intensities of hypothetical symmetry equivalent reflections measured by SXRD can help to recognize the occurrence of a pseudo symmetry.

Often pseudo symmetry forms, however, simultaneously with the generation of twin domains at the phase transition from a high- into a low-temperature phase by symmetry reduction. The twin domains are then interrelated by twinning operators equal to some symmetry operators of the space group of the high-temperature phase that are not symmetry of the low-temperature phase. Dependent on the twinning rule, certain reflections split into several peaks arising from the different domains while other reflections appear as single maxima, because of a coincidence of the single domain contributions. Due to the overlap of the single domain contributions the intensities of reflections generated by just one domain can not be measured independently. Additionally, if the effect of peak splitting is small it is obscured by the spread of the wavelength spectra of conventional X-ray radiation and its divergence. To prove for the existence of a reflection splitting, diffraction experiments have to be carried out using almost perfect monochromatic radiation, e.g. highly monochromatized synchrotron radiation.

The experimental work for this thesis which was carried out by using synchrotron

radiation was performed at the beamline D3 of the HASYLAB facility of DESY (Hamburg). Other SXR D experiments were measured on a Nonius Mach3 four-circle diffractometer and a Mar345 image plate diffractometer installed at the laboratory of Crystallography of the university Bayreuth.

In chapter 2 a short description is given of the theory of phase transitions, and the phenomenological occurrence of spin-Peierls transitions is outlined.

Chapter 3 is dedicated to the methodological concepts with which the single-crystal experiments were carried out. The properties of conventional and synchrotron radiation as well as the experimental setup of the diffractometers used for the experiments are described. For the adjustment of the crystal temperatures during SXR D measurements different types of cooling systems were applied. Their conception and the sample preparation suitable for their successful performance are also discussed.

In chapter 4 a crystal-chemical description of the structural properties of the families of transition-metal trihalides and transition-metal oxyhalides is given. Although in this thesis only the influence of the phase transition in chain-structured trihalide TiI_3 was examined, a comparison to the layer-structured trihalides is undertaken to draw conclusions about the orientation of the magnetic spin moments in both compounds.

Initially, the research on the organometallic compound with the chemical composition $\text{Eu}(\text{SC}_{36}\text{H}_{49})_2$ was carried out to examine the chemical bonding and the reactivity between the metal atoms and the ligand molecules by the application of charge density calculations. This purpose was hindered by the occurrence of a phase transition found at a temperature of $T_c = 119$ K. The study on the low-temperature and the high-temperature structures, however, also provided information about the chemical bonding. Chapter 5 reports about the structural analysis carried out for the two structures, which also includes a comparison of selected calculated atomic valences.

TiOCl and TiOBr belong to a family of isostructural transition-metal compounds MOX with $M = \text{Ti}, \text{V}, \text{Cr}, \dots$ and $X = \text{Cl}, \text{Br}$. For a comparison of their already well known structural and magnetic properties with another homologous compound fruitless attempts have been undertaken to crystalize TiOI . The product of the failed synthesis, however, contained crystals of TiI_3 which were studied by SXR D (Chapter 6). Indications of a phase transition found at a transition temperature of $T_c = 323$ K and the low- and high-temperature crystal structures of TiI_3 are

presented. The crystal structures at three different temperatures were compared to unravel the origin of the phase transition. It is shown that the phase transition from the high- to the low-temperature phase is accompanied by a dimerization on chains of titanium atoms. The magnitude of dimerization of different halide compounds is compared to outline the influence of the matrix effect resulting from the different halogen atoms.

Investigations on the compound CrOCl were carried out to determine the influence of a cation exchange in the MOX structure type on the magnetic behavior and the distortion of the crystal structure in the low-temperature phase. In chapter 7 it is shown that the orthorhombic high-temperature phase of CrOCl transforms at a transition temperature of $T_c = 13.5$ K into a monoclinic low-temperature phase. The phase transition is set into relation with results of magnetic susceptibility measurements. The anisotropic thermal expansion of CrOCl is discussed in chapter 8 by a comparison of lattice parameters and structural characteristics determined for four different temperatures.

Chapter 2

Theoretical background

2.1 Theory of structural phase transitions in crystals

Phase transitions can be classified into continuous and discontinuous transitions characterizing the change of structural parameters and the inner energy at the transition temperature. At a discontinuous phase transition at least two phases coexist in an equilibrated state. The first derivative of the inner energy, the entropy, changes at the transition abruptly. In a continuous phase transition just one phase is engaged changing its thermodynamic quantities continuously in dependence on the system parameters. Because for the latter type of phase transition a discontinuity of the heat capacity is observed and this thermodynamic quantity constitutes the second derivative of the inner energy the transition is also termed as second-order phase transition and the discontinuous transition is called consequently a first-order phase transition.

In the following a description of the theory of phase transitions is given starting with a derivation of the fundamental relations of a second-order phase transition using Landau theory. The information gained will be used to explain the process of a first-order transition. The description follows the argumentation in *International Tables of Crystallography, Volume D: Physical Properties of Crystals* (2006). Because all the experiments carried out for this thesis were performed at ambient pressure the following only refers to phase transitions due to variations of the temperature.

2.1.1 Continuous phase transitions

The continuous character of a second-order phase transition results from a temperature-dependent atomic displacement \mathbf{u} of one or more atoms in the unit cell of the low-temperature phase away from atomic positions which are special positions in the unit cell of the high-temperature phase. The displacements can be expressed in terms of the three components u_x , u_y and u_z representing the atomic displacements parallel to the lattice directions. Nonzero displacement components define the order parameter η of the transition. The atomic displacements in the low-temperature phase are realized through the reduction of the space group symmetry at the phase transition to a subgroup symmetry of the high-temperature phase. The temperature-dependent atomic displacements in the low-temperature structure constitute equilibrated states in which the free energy F adopts minimal values resulting in the free energy to be left invariant by the phase transition. The free energy can be expressed as a function $F(T, \eta)$ presuming that the free energy is a continuous and derivable function and that also the displacement \mathbf{u} is changing continuously. For temperatures close to the transition temperature the free energy can be approximated by a Taylor series. For a second-order phase transition the symmetry demand of the free energy requires the disappearance of terms with odd degrees. By a truncation of the Taylor series of F at the term of fourth degree, and assuming a linear dependence of the term of second degree the free energy can be expressed as:

$$F = F_0(T) + \frac{\alpha(T_c - T)}{2}\eta^2 + \frac{\beta}{4}\eta^4. \quad (2.1)$$

In this equation α is an odd function of $(T - T_c)$ and changes its sign at the transition temperature and β represents a positive constant. The condition for the occurrence of a minimal free energy is:

$$\frac{\partial F}{\partial \eta} = 0; \quad \frac{\partial^2 F}{\partial \eta^2} > 0. \quad (2.2)$$

For $T > T_c$ the solution is $\eta = 0$ and for $T < T_c$ it is

$$\eta^0 = \pm \sqrt{\frac{\alpha}{\beta}(T - T_c)}. \quad (2.3)$$

The two solutions of η^0 obtained by (2.3) correspond to the two possible displacements along the z -axis differing from each other only by the displacement direction (Fig. 2.1 a).

Examples for a second-order phase transition are ferromagnetic-paramagnetic and order-disorder transitions.

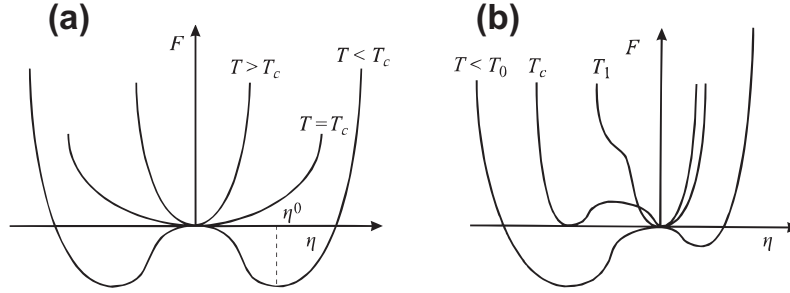


Figure 2.1: Changes of the free energy at different temperatures effected by a variation of the order parameter η of a continuous phase transition (a) and a discontinuous phase transition (b). The temperature T_0 in (b) represents the observed phase transition temperature (Tab. 2.1). Minimal values of the free energy correspond to the equilibrium values. Graphics were taken from *International Tables of Crystallography, Volume D: Physical Properties of Crystals* (2006).

2.1.2 Discontinuous phase transitions

A coexistence of two phases implies from the thermodynamical standpoint of view an equilibration of their chemical potentials μ . The temperature dependence of the chemical potential and the free energy are related to the change of the entropy S , because the pressure p is constant and the volume changes dV associated with solid state transitions are generally small,

$$\begin{aligned} d\mu &= -s \cdot dT + V \cdot dp \\ dF &= -s \cdot dT - p \cdot dV. \end{aligned} \quad (2.4)$$

In analogy to expression (2.1) the free energy can be approximated by a Taylor series in which, however, the symmetry condition of F allows the occurrence of third degree terms. The equation can be written as:

$$F = F_0 + \frac{\alpha(T - T_0)}{2}\eta^2 + \frac{\delta}{3}\eta^3 + \frac{\beta}{4}\eta^4 \quad (2.5)$$

with T_0 standing for the observed phase transition temperature, α standing for an odd function of $(T - T_0)$ whose sign changes at the phase transition and δ and β representing some positive constants. The minimum of the free energy is determined by:

$$\frac{\partial F}{\partial \eta} = \eta [\alpha(T - T_0) + \delta\eta + \beta\eta^2] = 0. \quad (2.6)$$

Table 2.1: Number, specification and location of extremal points of the free energy as a function of the temperature. The labeling of the temperatures are equivalent to the labeling in Fig. 2.1 b.

Temperature	No.	Specification	η
$T > T_1$	1	minimum	0
$T_c < T < T_1$	2	minimum	0
		local minimum	$1/2\beta[-\delta \pm \sqrt{\delta^2 + 4\alpha\beta(T_0 - T)}]$
$T_0 < T < T_c$	2	local minimum	0
		minimum	$1/2\beta[-\delta \pm \sqrt{\delta^2 + 4\alpha\beta(T_0 - T)}]$
$T < T_0$	3	maximum	0
		minimum	$1/2\beta[-\delta + \sqrt{\delta^2 + 4\alpha\beta(T_0 - T)}]$
		minimum	$1/2\beta[-\delta - \sqrt{\delta^2 + 4\alpha\beta(T_0 - T)}]$

The solutions of the equation are $\eta = 0$ and

$$\eta = \frac{1}{2\beta} \left[-\delta \pm \sqrt{\delta^2 + 4\alpha\beta(T_0 - T)} \right]. \quad (2.7)$$

The shape of the free energy curve changes with temperature and exhibits one, two or three extremal points. The curvature of the graph can be classified into four temperature ranges which are confined by the three characteristic temperatures T_1 , T_c and T_0 (Tab. 2.1 and Fig. 2.1 b). For a temperature above T_1 only one solution for the state of equilibrium of the free energy exists while at temperatures between the temperature T_1 and T_0 two solutions exist of which one represents a metastable state and the other a stable state. Due to this metastability the high-temperature structure can be preserved down to the temperature T_0 where the metastability is revoked. This implies that the phase transition from the high- into the low-temperature phase is in virtue often not observed at T_c but at the lower temperature T_0 .

The order parameter η is a measure for the propagation of the phase transition. Its temperature dependency is given by:

$$\eta = A \cdot \left(\frac{T - T_c}{T_c} \right)^\gamma \quad (2.8)$$

with γ standing for a critical exponent, T_c for the transition temperature and A for a constant.

2.2 The spin-Peierls transition

A Peierls transition is a metal-insulator transition which is associated with the dimerization of an atom chain causing gaps in the band structure.

Also for a spin-Peierls pairing of magnetic moments a dimerization of atoms is observed in the low-temperature phase. But in contrast to the Peierls transition the dimerization in the spin-Peierls transition is the consequence of an antiferromagnetic coupling of the spins of electrons on neighboring atoms. Spin-Peierls pairing and the antiferromagnetic order can be differentiated by the distance over which the coupling of the magnetic moments is established and by the effect the coupling has on the nuclear structure. While the spin-Peierls pairing is formed by a coupling of electron singlets of neighboring atoms the antiferromagnetic interaction results from a long-range order interaction of the magnetic moments and does not affect the crystal structures. The spin-Peierls pairing, however, is associated with a structural change originating from the atomic displacements of the coupling atoms to atom pairs resulting in a phase transition. The transition can be a first- or a second-order phase transition (Penson et al. (1976)).

If the paired spin moments are forming one dimensional antiferromagnetic spin chains then the interaction can be described by the quantum mechanical exchange integral based on the Heisenberg model (Chesnut (1966)). Using the exchange interaction J and the spin vectors \vec{S}_1 and \vec{S}_2 the exchange energy E of two coupling spin moments is determined through:

$$E = -2J\vec{S}_1 \cdot \vec{S}_2. \quad (2.9)$$

The existence of a spin-Peierls transition was theoretically predicted by (Chesnut (1966)) and experimentally proven by the discovery of spin chain instabilities in both organic and metal-organic compounds (Bray et al. (1975); Jacobs et al. (1976)). Later it was found that also the inorganic compounds CuGeO_3 (Hase et al. (1993)) and TiOCl (Seidel et al. (2003); Shaz et al. (2005)) undergo spin-Peierls transitions.

Chapter 3

Experimental techniques

3.1 Generation of X-ray radiation

3.1.1 Conventional X-ray radiation

Conventional X-ray radiation used for laboratory experiments is generated either in X-ray tubes or by rotating anodes through fast electrons impinging on a metal target in vacuum. The emitted X-ray radiation consists of a continuous spectrum of Bremsstrahlung, and, if the energy of the electron beam is high enough, characteristic radiation with a discrete energy distribution. The characteristic radiation is generated through intra atomic electron transitions within the metal atoms induced by a removal of core electrons after collisions with irradiating electrons. The photon energies of the characteristic radiation correspond to energy differences between electron levels whose locations in an energy level diagram are specific for the element used as target. The most intense characteristic radiation is the $K_{\alpha 1}$ -line (in IUPAC-notation: K-L₃-line) which results from the transition of electrons from the L₃-level into the K-level. Its intensity is two times higher than the intensity of the $K_{\alpha 2}$ -line (K-L₂-line) resulting from the transition L₂ → K. Prior to its experimental application the radiation is monochromatized to the K_{α} -lines employing a monochromator. The average wavelength of the Mo- K_{α} radiation is 0.7107 Å.

In rotating anode devices the electron beam is focused on a rotating, water cooled cylinder. Due to the dissipation of the thermal energy of the beam over the lateral area rotating anodes can produce higher X-ray intensities than sealed X-ray tubes.

3.1.2 Synchrotron radiation

Another source for X-ray radiation is provided by particle accelerators in which electrons or positrons are forced to travel on a closed path emitting synchrotron radiation of a continuous spectra by crossing magnetic fields. To compensate the loss of their kinetic energy resulting from the radiation emission, the particles are accelerated in electric fields of radio-frequency. The storage system is divided into straight sections in which so called insertion devices are implemented and sections in which the beam is redirected by bending magnets. In the insertion devices periodic magnetic fields are generated by which an oscillation of the particles about their traveling direction is induced resulting in an increase of the emitted synchrotron radiation and an optimization of the wavelength spectra.

The main advantages of the synchrotron radiation over conventional X-ray radiation for single-crystal X-ray diffraction experiments arise from its properties to be tuneable in a wide spectral range and to possess a low beam divergence, a high intensity and a high spectral brilliance. The magnitude of the X-ray absorption by a crystal is dependent on the crystal size and the absorption coefficient of the compound forming the crystal. The absorption coefficient is dependent on the energy of the radiation. The ability to tune the wavelength at synchrotron facilities permits minimization of the absorption by the crystal (Fig. 3.1). Likewise, the tunability allows to perform X-ray experiments using wavelengths which are not attainable by conventional X-ray sources. The low beam divergence of the synchrotron radiation results from a distortion of the angular distribution of the relativistic traveling charged particles (Aslanov et al. (1998)). By lowering the beam divergence the width of reflections in X-ray diffraction is reduced.

The photon fluxes provided by synchrotron facilities are about $10^4 - 10^5$ times higher than in rotating anodes and reach 10^{13} - 10^{23} photons s^{-1} mm^{-2} $mrad^{-2}$ for 0.1% bandwidth (Giacovazzo et al. (2002)). In the storage system of the synchrotron facility Hasylab (DESY, Hamburg) positrons divided into five bunches are employed to generate synchrotron radiation. The critical wavelength of this synchrotron is 0.773 Å ($\simeq 16.04$ keV). Due to the drastic decrease of intensities towards the lower wavelengths, the useful limit for X-ray experiments is 0.41 - 0.35 Å ($\simeq 30$ -35 keV) at Hasylab.

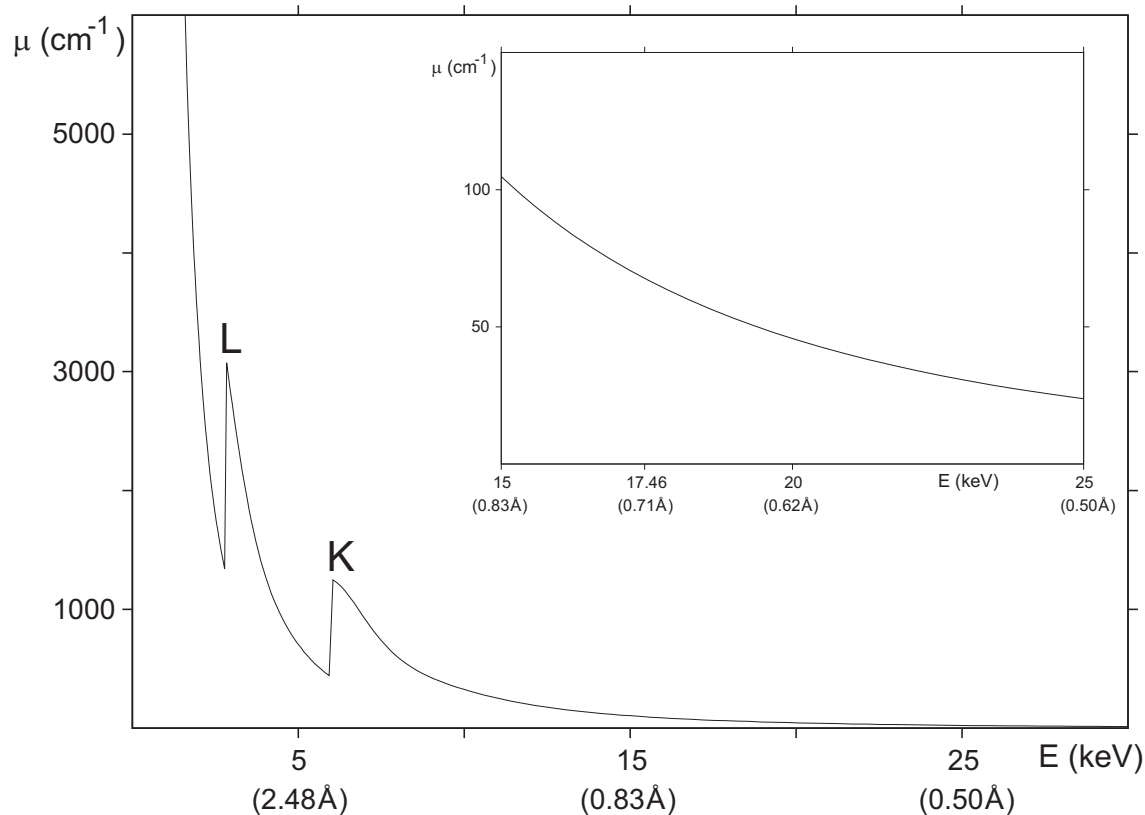


Figure 3.1: Energy dependence of the absorption coefficient of CrOCl calculated by using the software XOP (Del Rio and Dejeus (1998)). Wavelengths corresponding to the radiation energies are set in parentheses. The inset represents a magnified section of the high-energy region.

3.1.3 Monochromatization

For the monochromatization of conventional X-ray radiation single-crystal monochromators are often employed. The monochromatization is carried out by the diffraction of X-ray radiation on a monochromator crystal causing a wavelength dependent occurrence of reflection maxima at different scattering angles. For the monochromatization of Mo- K_{α} radiation frequently a monochromator crystal of graphite is used. The monochromator crystal is oriented in that way that a strong reflection at low scattering angle provides monochromatized radiation. To focus the beam on the sample bent monochromators can be used. To reduce the aberration which results from the crystal bending the crystal surface has to be ground so that the curvature

of the surface possess a certain radius which is different from the curvature of the diffracting planes.

The wavelength of synchrotron radiation can be tuned to a small bandwidth ($\Delta\lambda/\lambda \sim 10^{-4} - 10^{-5}$) of the continuous radiation spectrum by employing a double crystal monochromator. The wavelength is tunable by tilting one of two, almost parallel monochromator crystals, but this requires that the radiation possesses a low beam divergence making the double crystal monochromator not applicable for the monochromatization of conventional X-ray radiation.

Because of their low expansion coefficient at low temperatures the monochromator crystals are often manufactured of silicon or germanium. Thus, the effect of beam misalignment induced through the thermal expansion of the crystals resulting from changes of the radiation fluxes can be diminished. At the beamline D3 at the Hasylab (DESY, Hamburg) the crystals are, however, calibrated for enduring use and are not cooled. It is expected that the temperature of the crystals changes only at the beginning of every new exposure by the beam and that the crystals adopt after some seconds a stable equilibration temperature.

X-rays are reflected by mirrors if the angle of incidence is smaller than a critical angle. The critical angle is wavelength dependent and the radiation of a wavelength essentially smaller than the wavelength corresponding to the critical angle is absorbed by the mirror material. Mirrors are therefore used to preselect an energy range of a radiation spectrum. Toroid mirrors are furthermore employed to focus the beam.

3.2 Single-crystal X-ray Diffractometers

Single-crystal X-ray diffractometers are instruments which are used to orient the crystal in an X-ray beam and to detect the radiation scattered from it. The crystal orientation is accomplished by the goniometer of the diffractometer. Depending on the number of rotation axes present in the goniometer, diffractometers are named one-, two-, three-, etc. circle diffractometers. In a one-circle diffractometer the crystal is rotated about one predefined axis and the detector stays during measurement fixed. The goniometers of two-, three- and four-circle diffractometers generally allow a rotation of the detector and the additional rotation axis are used to increase the degrees of freedom of orienting the crystal.

Two kinds of four-circle goniometer geometries can be distinguished namely the

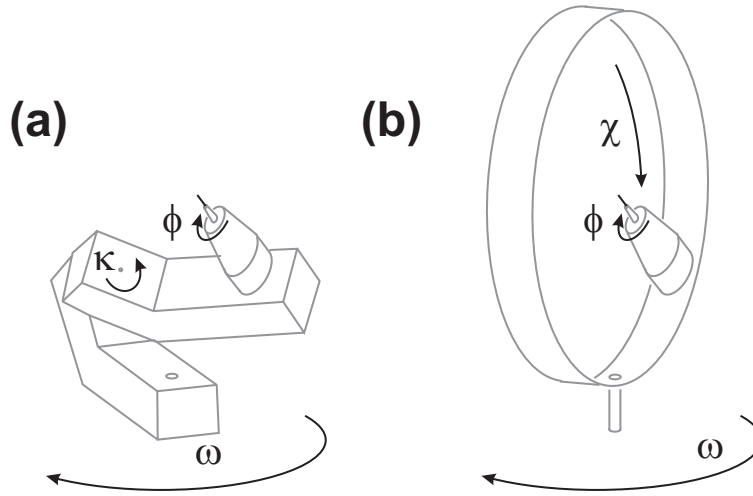


Figure 3.2: Arrangement of the crystal rotating axes in goniometers possessing κ -geometry (a) and Euler-geometry (b). The crystal orientation in sketch (a) and (b) are the same.

Euler-geometry and the κ -geometry (Fig. 3.2). Diffractometers of both designs were used for the performance of the experimental work for this thesis. The diffractometer Mach3 by Nonius is built in κ -geometry. It was employed for testing of crystals as well as for measuring of reflection profiles used for a determination of the crystal shape. The Huber diffractometer installed at the beamline D3 of HasyLab is constructed in the Euler geometry. The shift of the ϕ -axis from the equatorial plane of the Euler-cradle enables to mount a closed-cycle cryostat (Fig. 3.3). Profiles on selected reflections were measured by means of a point detector. In both the κ - and the Euler geometry one axis, the ω -axis, is oriented parallel to the 2θ -axis which is the axis for rotation of the detector. On the ω -block the other two axes are mounted (Fig. 3.2). In the Euler-geometry the two axes are the χ - and the ϕ -axis. The χ -axis is oriented perpendicular to the ω -axis and by its rotation the ϕ -axis is tilted from the ω -axis.

In the κ -geometry the tilting of the ϕ -axis is accomplished by a rotation about the κ -axis. The κ - and ω -axis enclose a specific angle which is set for the diffractometer Mach3 exactly to 50 deg. Apart different values for κ and χ same crystal orientations in the κ - and Euler-geometry are distinguished by different values of ω . The angles of the two geometries are, however, trigonometrically related and most diffractometer software allow a transformation between them. Goniometers designed in κ -geometry can be successfully used in combination with an open flow

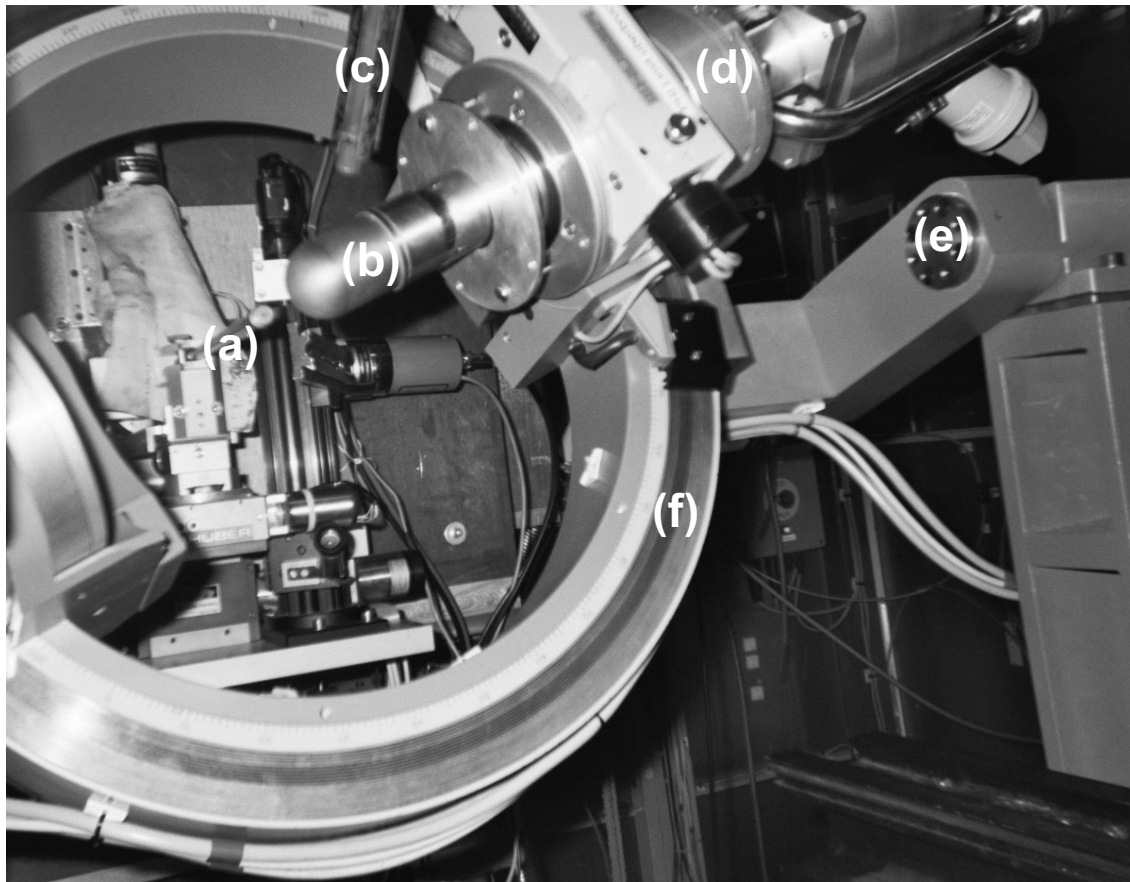


Figure 3.3: Experimental setup at beamline D3 (DESY, Hamburg) used for measurements of peak profiles. Primary beam collimator (a), outer beryllium cylinder (b), detector collimator (c), cryostat (d), ω -axis (e), Euler-cradle (f).

cooling systems since the access to the crystal along the opened side of the omega axis is not hindered through the bulky Euler-cradle (Fig. 3.2).

Point detectors are measuring the amount of photons irradiated at one position. The Huber and Mach3 diffractometer used for the experiments were equipped with NaI(Tl)-scintillation counters. The NaI(Tl)-scintillation detector possesses a low energy selectivity and can detect photons of a broad wavelength spectrum. In this kind of detector incident X-ray photons are converted to electrical signals using a scintillation crystal which absorbs the X-ray photons under generation of excited atom states. The excited states have a short life time ($\sim 2.5 \times 10^{-7}$ s (Aslanov et al. (1998))) and emit by their decay visible light of a defined wavelength that is amplified

by a photomultiplier to generate a photoelectron current. The measurement of reflection profiles can be accomplished by rotating the crystal (e.g. to perform ω -scans), by rotating the detector (2θ -scans) or both the detector and the crystal (ω - 2θ -scans). The inspection of reflection profiles allow an assessment of the crystal quality and can reveal the occurrence of a twinning indicated by a splitting or a broadening of reflection peaks. The background intensity of measurements carried out by using a point detector can be reduced through the application of adjustable detector slits and a collimator. Point detectors can, furthermore, be used to accomplish ψ -scans which allow a semi-empirical approximation of the crystal shape used for absorption correction of measured reflection intensities.

The one-circle goniometers are often combined with either an image plate or a CCD (charge coupled device) detector. Both kinds of detectors are area detectors. The measurement with these instruments is performed by rotating the crystal during exposure by a constant velocity. The diffraction patterns measured during each incremental rotation are stored as electronic images, so called frames, by the computer system controlling the measuring process.

The photoactive layers in the image plate contain fine-grained particles of Eu-doped barium halides. The diffraction information is stored within these layers by a photoinduced transfer of electrons from the europium ions to the halide vacancies. The energetically unfavored charge distribution in the layers can be readout by a laser causing a luminescence detectable by a scanner. Unlike photographic films, where the recorded information is stored permanently, image plates are reusable by deleting their information content by white light. Because image plate detectors possess a low noise level and a high dynamic range they are especially suitable for the measurement of weak reflections beside strong ones (Giacovazzo et al. (2002)).

CCD-cameras are constructed of independent semiconductor elements combined to arrays detecting the X-ray photons. Because their signals result from a generation of electron-hole pairs which have a low energy level CCD-detectors have a high dark current. Due to higher flux rates their use is more convenient for measurements with synchrotron or neutron radiation.

During the measurement using an area detector several reflections are measured simultaneously on each frame, thus, the experiment time is much shorter than the measurements carried out by employing a point detector. Reflection intensities determined by point detectors are, however, more precise than the ones measured by area detectors, because the counting statistics of point detectors lead to smaller standard uncertainties (Giacovazzo et al. (2002); Aslanov et al. (1998)).

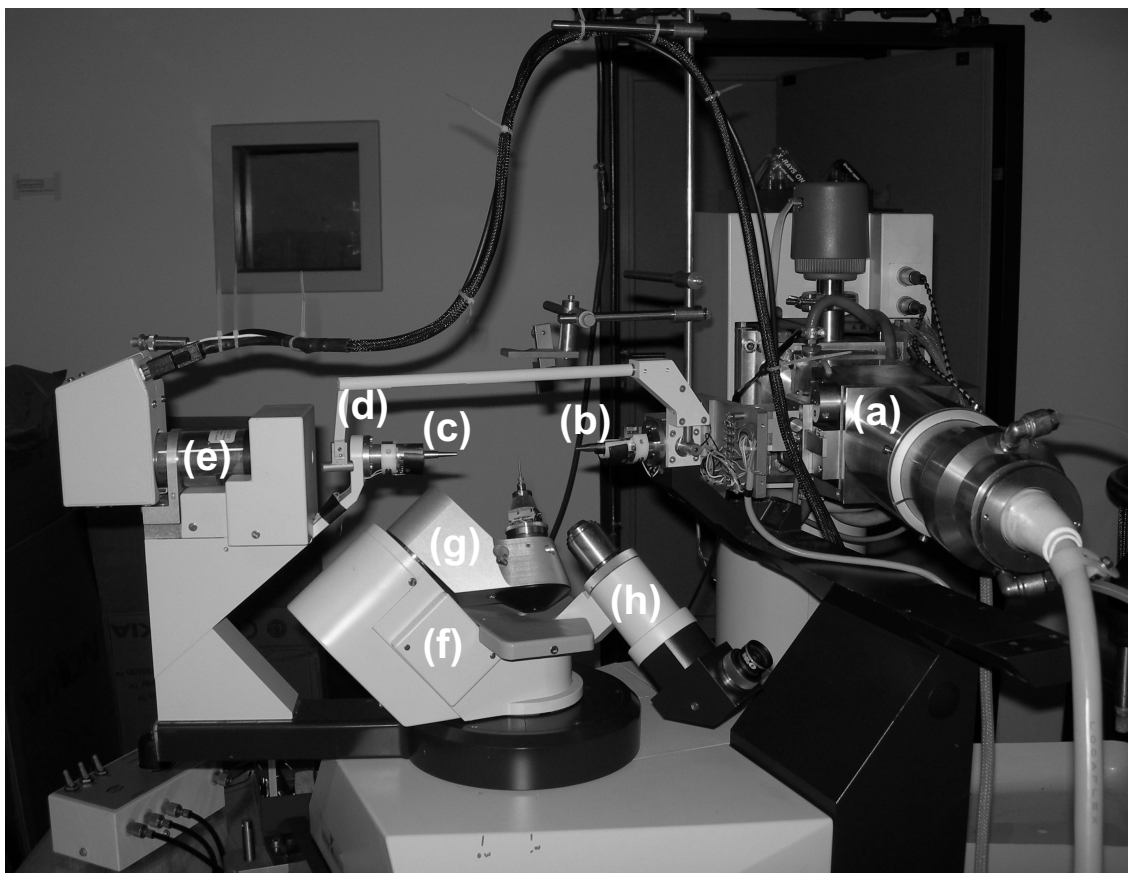


Figure 3.4: Setup of a Mach3 diffractometer using the κ -geometry (installed at the laboratory of crystallography, university of Bayreuth). (a) rotating anode, (b) beam collimator, (c) detector collimator, (d) beam stop, (e) detector, (f) ω -block of the goniometer on which the κ -block (g) and a microscope (h) are mounted.

3.2.1 Experiments on a Mach3 diffractometer

The Nonius Mach3 diffractometer is a four-circle diffractometer designed in κ -geometry (Fig. 3.4). The X-ray radiation used for the experiments was generated by a rotating anode using a beam current of 75 mA and an acceleration voltage of 55 kV. The diffracted radiation was detected by a photomultiplier whose signal was corrected to a deadtime loss smaller 1% of the counting rate.

The quality of crystals were checked by performing ω -scans on strong reflections distributed over the three lattice directions of the crystal. Beside an occurrence of peak splitting the peak width was the main criteria by which crystals were se-

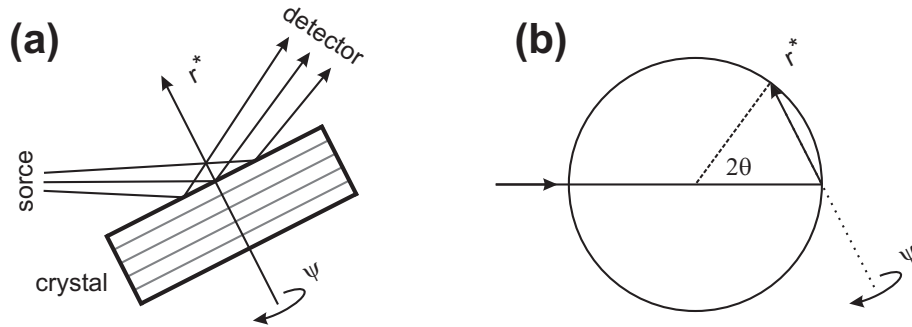


Figure 3.5: Crystal rotation about the ψ -axis in direct space (a) and in reciprocal space using the Ewald construction (b).

lected or discarded. Crystals which gave rise to strong reflections with peak widths (FWHM) substantially larger than the lowest experimentally reachable value of ~ 0.08 deg were not used for synchrotron experiments. The ω -scans were measured in a continuous rotation mode rotating over angles of 1 or 2 deg. For a higher accuracy the peak widths were determined by a curve fitting applying gaussian or pseudovoigt fit functions.

To correct the measured reflection intensities for the effects of absorption a knowledge of the crystal shape is necessary. The crystal shape can be determined by the measurement of ψ -scans on selected reflections. ψ -scans are performed by measuring each single reflection in orientations which are equivalent to orientations resulting from rotations about the scattering vector (Fig. 3.5). The ψ -scans were performed by measuring the intensities of reflections by ω - 2θ -scans and rotating the crystal about the ψ -angle in increments of 10 deg.

The principle of the semi-empirical crystal shape optimization can be understood by regarding first the X-ray absorption occurring by the transmission of photons through an ideal crystal polished to a perfect sphere. The percentage of absorbed photons depends on the absorption length of the crystal and on the lengths of the beam path through the crystal. A rotation of the spherical crystal about the ψ -axis has no influence on the reflection intensities since the lengths of the beam paths remain constant. For a rotation of a non-spherical crystal, however, the reflection intensities depend on the ψ -angle since different ψ -angles involve different lengths of beam paths through the crystal.

The ψ dependence of measured reflection intensities are used in the computer program HABITUS (Herrendorf and Bärnighausen (1997)) to refine a model for

the crystal shape. The refinement is performed by the optimization of a starting model consisting of a high symmetric form possessing many faces e.g. by using an icosahedron. The program optimizes the crystal shape by changing the distances of the faces to the center and by changing the tilting of the faces. The optimization process is controlled by an improvement of a figure of merit calculated from the maximal and minimal values of the absorption corrected intensities of reflections. The absorption correction of the intensities of the reflections was performed by using the integration software *Crysalis (Software Crysalis RED (2005))* or the program SADABS (Sheldrick (1998)).

3.2.2 Experiments on a MAR345 dtb diffractometer

The goniometer of the Mar345 dtb diffractometer possesses just one axis for rotation of the crystal, the ϕ -axis, which is oriented perpendicular to the primary beam (Fig. 3.6). The detector can be tilted in the 2θ -position.

The diameter of the Mar345 image plate is 345 mm and corresponds to 2300×2300 pixels in a digitized image with one pixel corresponding to $150 \times 150 \mu\text{m}^2$ in size. The dynamic range of the detector is 17 bit (from 0 to $2^{17}=131071$). The Laser and the scanner system are integrated in the Mar345 image plate detector allowing an automatic and fast readout and erasion of the image plates.

In the data reduction process reflection positions are determined to calculate the orientation matrix which expresses three non-coplanar crystal lattice directions by the diffractometer coordinate system. This process is performed by integration software programs (*Software Crysalis RED (2005)*; Duisenberg et al. (2003)) which are also applied for the subsequent processing steps including the integration of intensities of reflections mostly segmented over several frames.

3.3 Control of the crystal temperature

Low-temperature diffraction studies require a stable sample cooling combined with the diffractometer.

On the Mar345 dtb diffractometer the crystal temperatures were established using an Oxford cryostream cooling device. In this cryostat the crystal temperature is controlled by a cold nitrogen gas stream steadily blowing over the crystal. The nitrogen gas is produced by vaporization of liquid nitrogen pumped-off from an storage vessel. Crystal temperatures ranging from 80 to 400 K are attainable through

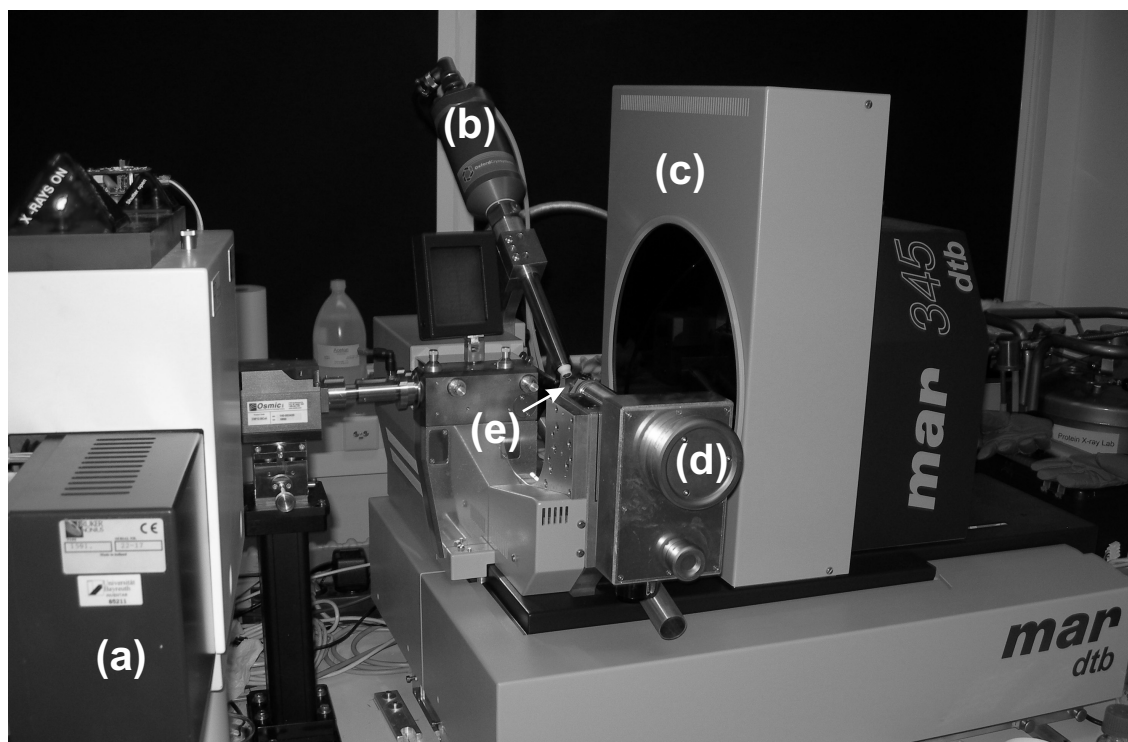


Figure 3.6: Setup of a mar345 dtb imageplate diffractometer (installed at the laboratory of crystallography, university of Bayreuth). (a) rotating anode, (b) cooling system, (c) detector, (d) ϕ -axis, (e) crystal.

the electrical heating of the gas. The lower temperature limit of the cooling device is determined by the boiling point of nitrogen which corresponds to a temperature of 77.35 K at ambient pressure.

Lower crystal temperatures can be achieved through the application of an open flow Helijet or a closed-cycle cryostat using helium as cryogen gas. The working principle of the Helijet is similar to the one of the cryostream. The lowest attainable temperature of the open flow cooling method is ~ 10 K.

A closed-cycle cryostat was employed for cooling of CrOCl single-crystals, towards temperatures below the phase transition temperature of $T_c = 14$ K. The crystal temperatures adjustable by a closed-cycle cryostat are ranging from the boiling temperature of helium corresponding for ambient pressure to a temperature of 4.22 K to room temperature. The cooling effect in a closed-cycle cryostat results from the cycled process of compressing helium gas and releasing it into an evacuated

chamber which is subsequently evacuated anew. The crystal is cooled through the thermal contact to a cold finger consisting of a copper rod of 200 mm in length. Crystal temperatures are adjusted via an electrical heating at the end of the cold finger. To allow a good thermal conductivity from the crystal to the cold finger the crystal is mounted on a bundle of carbon fibres (Section 3.4). Temperature increase and icing of the cooled crystal through the contact to air was prevented by the use of two evacuated beryllium cylinders (Fig. 3.3). The inner cylinder was cooled to reduce the thermal radiation at the crystal. The beryllium shielding gives rise to X-ray absorption whose magnitude is dependent on the beampath of the radiation and to diffraction rings.

Unfortunately, variations of the temperature cause a shrinking or expansion of the cold finger and thus shift the crystal outside the center of the X-ray beam. Readjusting the height of the crystal is optically precluded by the beryllium shielding and has therefore to be performed through the optimization of the intensities of reflections and can be calculated for $T \sim 20$ K.

3.4 Crystal preparation

Data collections carried out on the laboratory diffractometers (Mar345 dtb and Nonius Mach3) were performed on crystals ranging from 150 to 300 μm in their maximum edge lengths. The investigated crystals were diffracting Mo- $K\alpha$ X-ray radiation to 2θ -angles larger 60 deg.

The size of the surveyed crystals was limited by the diameter of ~ 400 μm of the beam because an incomplete irradiation of the crystal results in too low intensities of some reflections.

Lamellae-shaped crystals of CrOCl up to 200 μm in length were attached with the aid of a small amount of a two-component glue to the top of boron glass fibres (Fig. 3.7 (a)). ω -Scans performed on reflections of bigger crystals exhibited often broad peak widths which was interpreted by imperfect crystallization of larger individuals. The crystals were prepared on boron glass fibres because of the low X-ray absorption of boron glass. For the low-temperature experiments using a closed-cycle cryostat the CrOCl crystals had to be prepared on thermal conducting needles. The needles were produced by cementing of carbon fibres using a two-component glue. They were fixed into copper pins by aid of thermal conducting silver lacquer and the outstanding ends were cut with a razor blade to lengths of about 2 mm. The

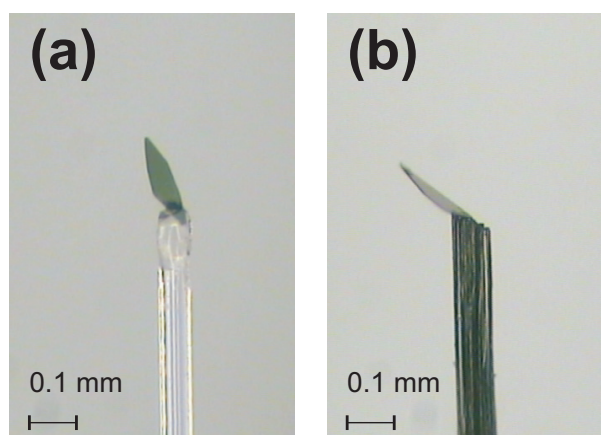


Figure 3.7: Single-crystal of CrOCl glued on the top of a boron glass fibre (a) and on the top of carbon fibres (b).

crystals were attached using a tip of two-component glue to the top of the needles (Fig. 3.7 (b)).

Air-sensitive crystals of the organometallic compound $\text{Eu}(\text{SC}_{36}\text{H}_{49})_2$ were cut in the cryoprotectant oil Paraton-N to lengths of $\sim 300 \mu\text{m}$. The crystals were set to the top of boron glass fibres and their positions on the fibres were fixed by cooling the crystal beneath the hardening temperature of the oil. Single-crystals prepared in Paraton-N were destroyed at temperatures close to the phase transition temperature. Thus, crystals used for a data collection on the low-temperature phase were prepared without oil under a nitrogen gas stream. In contrast to the crystal cutting in oil where crystal splinters were easily removed from the surface by moving the crystals the cutting of crystals under nitrogen atmosphere had to be carried out with more care avoiding a generation of splinters. The cut crystals were attached to the boron fibres using a two-component glue.

Because of their high hygroscopicity crystals of TiI_3 were inspected and prepared in the glove box under argon atmosphere. Thin needles of TiI_3 which were $\sim 300 \mu\text{m}$ long were placed on micro meshes of polyimide sample mounts (Fig. 3.8 (b); Thorne et al. (2003)) whose surfaces were made adhesive by covering them with a thin film of vacuum grease. The adhesion of the crystals to the flat surface of the micro mounts led to a tension free fixing of the crystals, thus, a splitting of the crystals observed in initial attempts by mounting crystals on boron glass fibres could be avoided. Air contact during the transfer of the prepared TiI_3 -crystals to the nitrogen gas stream

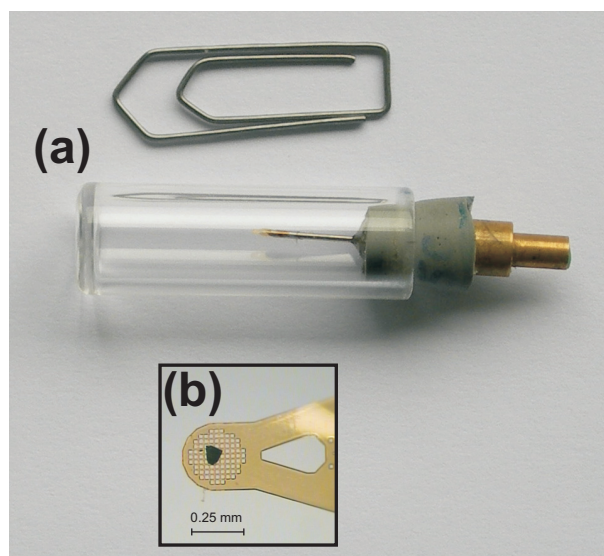


Figure 3.8: Hygroscopic crystal sealed in a capsule containing inert gas (a). Crystal attached to the surface of a micro mount (b).

of the diffractometer was prevented by a sealing in a small capsule filled with inert gas (Fig. 3.8 (a)). After opening of the container the plug holding the crystal could be set to the diffractometer. The prepared crystals could maintain several days within the closed capsule without any signs of deterioration but got hydrolyzed by the exposition to the humidity of air within two to five minutes.

Chapter 4

Crystal chemistry of selected transition-metal compounds

4.1 The transition-metal trihalides

The transition-metal trihalides (MX_3) form layered crystal structures of the BiI_3 and AlCl_3 structure types and quasi-one-dimensional structures of the TiI_3 structure type (Lin and Miller (1993)). The symmetry of the BiI_3 structure type is $R\bar{3}$ while it is $P6_3/mcm$ for the TiI_3 structure type. The average structures of the BiI_3 and the TiI_3 structure types consist of a hexagonal closest packing of halogen atoms in which one third of the octahedral interstices are occupied by metal atoms while the remaining two thirds are empty.

The different structure types arise from different distributions of the metal atoms over the octahedral sites.

In the BiI_3 structure type each MX_6 -octahedron is edge sharing with three adjacent octahedra forming hexagonal nets of metal atoms oriented perpendicular to the lattice direction \mathbf{c} (Fig. 4.1a) and the honeycomb-like layers of the metal atoms are screwed trigonally along the \mathbf{c} direction.

In the TiI_3 structure type MX_6 -octahedra are face sharing and the metal atoms form chains running parallel to the lattice direction \mathbf{c} (Fig. 4.1b).

The AlCl_3 structure type consists also of layers of edge sharing MX_6 -octahedra in analogy to the BiI_3 structure type but the halogen atoms are cubic closest packed.

Several MX_3 -compounds are polymorph and can form two or more structure types depending on the crystallization conditions. The compounds TiCl_3 and TiBr_3 for example crystallize at low temperatures in the BiI_3 -structure type (α -modification)

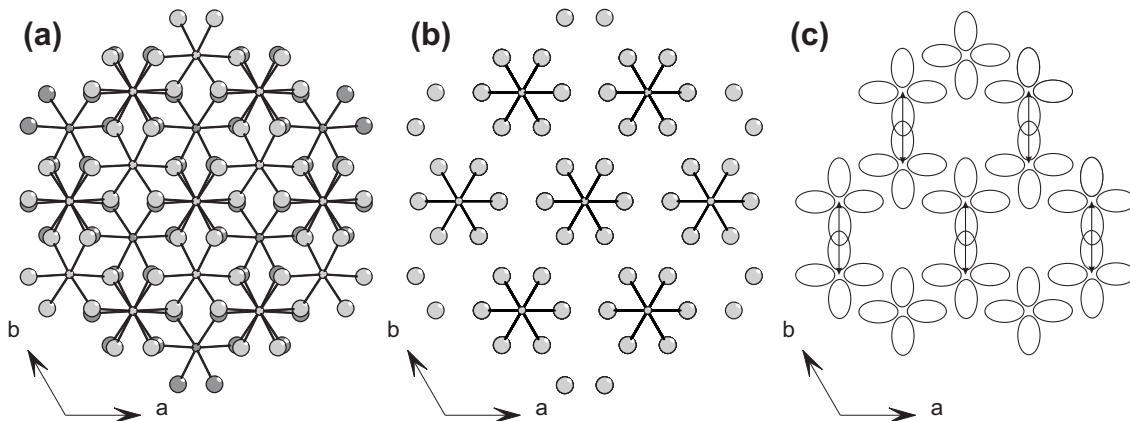


Figure 4.1: Section of crystal structures of the BiI_3 structure type (a) and the TiI_3 structure type (b) projected along the lattice direction \mathbf{c} . Atoms belonging to the same layers of the BiI_3 structure type are colorized in equally grey saturations. Metal atoms are depicted as small spheres and halogen atoms are represented by big spheres. Chemical bonds between metal and halogen atoms are represented by lines. (c) one possible arrangement of the $d_{x^2-y^2}$ orbitals in the α -modifications of TiX_3 . The lobes of the orbitals are depicted as ellipsoids and overlap in one direction of the (\mathbf{a}, \mathbf{b}) plane. The resulting dimerization of the metal distances is symbolized by arrows.

but adopt at high temperatures preferably the TiI_3 -structure type (β -modification) (Newland and Shelton (1970)). TiI_3 , however, crystallizes only in the TiI_3 structure type. Some MX_3 compounds form crystal structures in which the stacking sequences of the metal atom layers are disordered and can neither be assigned to the hexagonal nor to the cubic stacking sequence (Brodersen, Thiele, Ohnsorge, Recke and Moers (1968)).

Because of the d^1 configuration of the Ti^{3+} ions the TiX_3 compounds tend to establish direct magnetic spin interactions between neighboring metal atoms at low temperatures. As consequence the TiX_3 compounds undergo by cooling a phase transition from a paramagnetic room-temperature phase into a low-temperature phase in which antiferromagnetic spin coupling of the d^1 valence electrons is observed (Pollini (1983), Drent et al. (1975)). In the α -modifications the dimerization occurs in the plane of the honeycomb-like layers of metal atoms and in the β -modifications along the metal chains.

The fivefold degenerate d orbitals of the titanium atoms split under the influence

of the octahedral ligand field of the halogen atoms into a group of two states at higher and a group of three states at lower energy. The single d electron of Ti^{3+} occupies one of the three low-energy states. The low-energy states are d_{xy} , d_{xz} and d_{yz} and the high-energy states are $d_{x^2-y^2}$ and d_{z^2} .

In the crystal structure of $\alpha\text{-TiX}_3$ the dimerization direction of the titanium atoms is coplanar with the equatorial plane of the honeycomb-like layers. The equatorial plane constitutes the xy -plane of the d orbitals in which the axes of the d_{xy} and the $d_{x^2-y^2}$ orbitals are located. One of the lobes of the $d_{x^2-y^2}$ or the d_{xy} orbital is pointing into the direction of the dimerization suggesting a substantial contribution of this orbital to the magnetic spin interaction. The geometry of these orbitals is furthermore possibly the reason why each titanium atom can establish a spin-interaction to just one of the three neighboring titanium atoms. The axes of the orbital include an angle of 90 deg which is incompatible with the angles of the atomic arrangement in the honeycomb-like metal layers (Fig. 4.1c).

In the structures of the $\beta\text{-TiX}_3$ modifications the d_{xy} and $d_{x^2-y^2}$ orbitals are also oriented perpendicular to the c -direction and their energies are lowered by an elongation of the coordination polyhedra along the chain axis (Drent et al. (1975)). In the $\beta\text{-TiX}_3$ modifications the distances between neighboring titanium atoms on the metal chains are substantially smaller than the metal-metal distances established in the honeycomb-like layers of metal atoms in the $\alpha\text{-TiX}_3$ modifications (Tab. 4.1). The close contact of the titanium atoms in the β -modification allows a strong orbital overlap of neighboring d_{z^2} orbitals which is regarded responsible for the formation of an antiferromagnetic spin pairing by which the transition to the low-temperature phase is promoted (Drent et al. (1975); Pollini (1983)).

Due to the dimerization of the metal atoms associated with the transformation into the low-temperature phase the origin of the transitions of the α - and the β -modification of the TiX_3 compounds can not be sought in pure antiferromagnetic spin interactions (Section 2.2) and is more probably driven by a spin-Peierls pairing of the metal atoms.

4.1.1 Phase transitions of $\alpha\text{-TiX}_3$ ($\text{X} = \text{Cl}, \text{Br}$)

The room-temperature phase of the α -modification of TiCl_3 (TiBr_3) undergoes at a temperature of $T_c = 217$ K (180 K) a phase transition to a low-temperature phase whose crystal structure possesses triclinic symmetry (Maule et al. (1988)). The reduction of symmetry is caused by the dimerization of the titanium atoms in the

Table 4.1: Average metal-metal distances in selected transition-metal trihalides at room-temperature.

compound	distance (Å)	Reference
α -TiCl ₃	3.55	Troyanov and Snigireva (2000)
β -TiCl ₃	2.91 ^a	Natta et al. (1961)
α -TiBr ₃	3.74	Troyanov et al. (1994)
β -TiBr ₃	3.0475 ^a	Newland and Shelton (1970)
TiI ₃	3.255(2)	Angelkort et al. (2009)

^adetermined from lattice parameter **c**

honeycomb layers of the structure. The dimerization is caused by a displacement of the titanium atoms in one of the three symmetry equivalent lattice directions of the hexagonal unit cell of the high-temperature phases (Troyanov et al. (1994); Troyanov and Snigireva (2000)). The phase transition is accompanied by changes of the lattice parameters in the vicinity of the transition temperatures T_c resulting for decreasing temperatures first in a decrease of the lattice parameter **a** and for gently lower temperatures in an increase of the lattice parameter **c** (Ogawa (1960)) underlining the importance of the dimerization along **a** for the phase transition. At temperatures below T_c the magnetic susceptibilities of TiCl₃ and TiBr₃ decrease abruptly (Klemm and Krose (1947); Ogawa (1960)) indicating that the dimerization of the titanium atoms is related to the occurrence of an antiferromagnetic coupling of the magnetic moments of the atoms (Fig. 4.2).

4.1.2 Phase transition of β -TiX₃ (X = Cl, Br, I)

The symmetry of the β -modifications of TiX₃ reduces at the transition into the low-temperature phase to the subgroup symmetry $Pmmn$. Frequently the orthorhombic symmetry of the low-temperature structure is hidden by a pseudo-hexagonal symmetry originating in twinning. The twinning rule corresponds to the rotation about a threefold axis oriented parallel to the lattice direction **c**¹.

In comparison to the α -modifications of TiX₃, which exhibit pronounced changes of the magnetic susceptibility in the vicinity of the transition temperature, the absolute value of the magnetic susceptibilities of the β -modifications as well as their

¹The effect of twinning in the β -TiX₃ structures is highlighted in the appendix C.

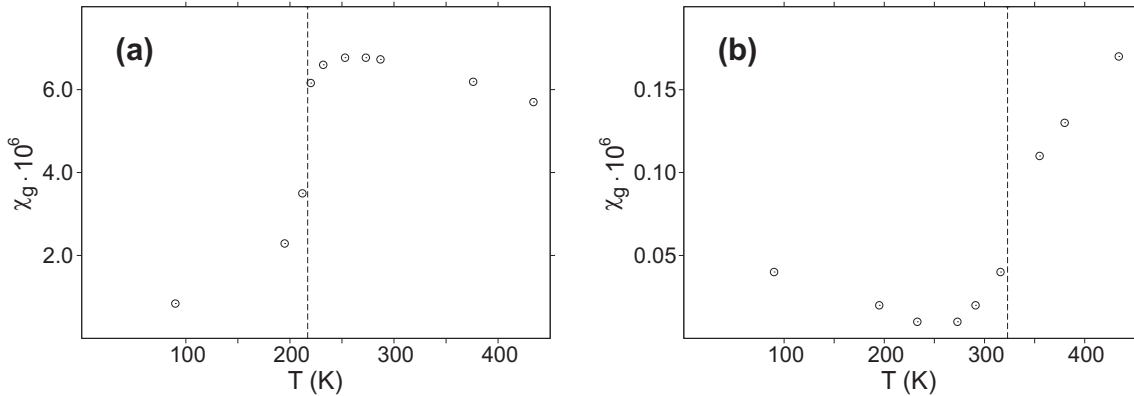


Figure 4.2: Temperature dependence of the magnetic susceptibility of (a) α -TiCl₃, and (b) TiI₃. Reprinted from Klemm and Krose (1947). Broken lines mark the transition temperatures of α -TiCl₃ (Ogawa (1960)) and TiI₃ (Angelkort et al. (2009)).

changes resulting from the phase transitions are rather small (Fig. 4.2)(Klemm and Krose (1947); Lewis et al. (1962)). The anomalously low susceptibilities of the β -MX₃ phases is attributed to a competition between an antiferromagnetic and a ferromagnetic coupling of the magnetic moments of the metal atoms in these structures (Baker and Janus (1964)). Thus, the susceptibility change resulting from the transition into the low-temperature phase can be interpreted with an increase of the antiferromagnetic interaction with respect to the ferromagnetic coupling.

4.2 The transition-metal oxyhalides

4.2.1 Crystal structures and magnetic behavior

The transition-metal oxyhalides (MOX) form layered crystal structures of the FeOCl structure type possessing the symmetry $Pm\bar{m}n$ at room-temperature. In the structure chains of metal atoms, chains of oxygen atoms and chains of chlorine atoms run parallel to the lattice direction **b**. The stacking direction of the MOX layers are parallel to **c** (Fig. 4.3). The metal and oxygen chains form corrugated double layers which are sandwiched by two layers of halogen atoms. The metal atoms are accommodated at centers of distorted octahedra defined by two halogen and four oxygen atoms.

The d orbitals of the transition-metal atoms give rise to interactions of magnetic

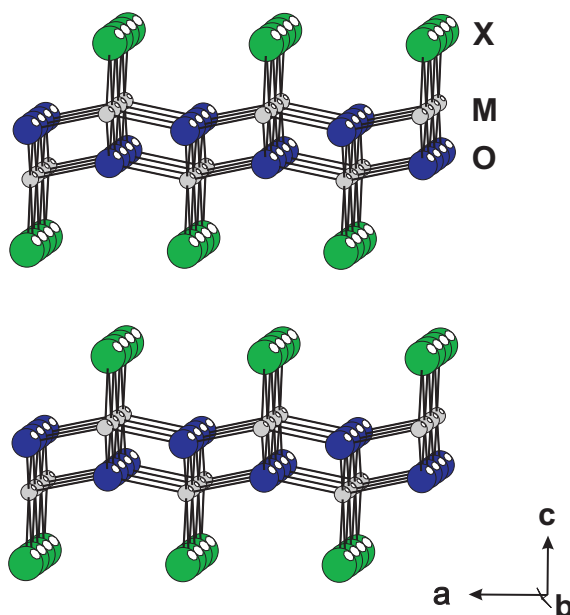


Figure 4.3: MOX crystal structure depicted via parallel projection. The labels M , O and X are referring to metal, oxygen and halogen atoms respectively.

spin moments by which MOX compounds undergo antiferromagnetic phase transitions. Depending on the number of electrons of the metal atoms, spins of electrons on neighboring atoms can interact by direct exchange along the metal chains, by direct exchange involving neighbors on neighboring chains and by a M–O–M superexchange oriented almost parallel to the lattice direction **a**. Due to the effect of these interactions MOX compounds exhibit phase transitions to low-temperature phases which possess different magnetic structures and can also differ in their nuclear structures. For the MOX compounds with titanium two phase transitions and the formation of an incommensurately modulated intermediate phase has been observed (Seidel et al. (2003); Schönleber et al. (2006); van Smaalen et al. (2005)).

The other MOX compounds undergo only one phase transition (Adam and Buisson (1975); Christensen et al. (1975); Wiedenmann et al. (1983)), which is associated with a lowering of the symmetry from orthorhombic to monoclinic on lowering the temperature. Often the transition is accompanied by twinning resulting from the two possible orientations of the monoclinic lattices on the orthorhombic lattice².

²In Appendix D a formula is derived used to calculate the monoclinic angle of CrOCl from a peak splitting caused by crystal twinning.

4.2.2 Phase transitions of TiOCl and TiOBr

TiOCl and TiOBr each undergo two phase transitions at which the crystal structures and the space group symmetry change (van Smaalen et al. (2005)). By decreasing the temperature below the upper transition temperature T_{c2} (TiOCl: $T_{c2} = 90$ K, TiOBr: $T_{c2} = 48$ K) the room-temperature phase transforms into an intermediate phase whose structure is incommensurately modulated. Simultaneously the magnetic behavior of the compounds change from paramagnetic to antiferromagnetic (Seidel et al. (2003)). A further temperature decrease below T_{c1} (TiOCl: $T_{c1} = 67$ K, TiOBr: $T_{c1} = 28$ K) transforms the incommensurately modulated structure into a twofold superstructure of the high-temperature structure corresponding to a doubling of the lattice vector \mathbf{b} .

At the phase transition from the room-temperature phase into the intermediate phase the space group symmetry is reduced to the monoclinic c -unique superspace group $P2/n (\sigma_1, \sigma_2, 0)00$. The monoclinic angle γ adopts a value of 90.023 deg in the incommensurately modulated phase of TiOCl and is temperature independent (Schönleber et al. (2006)). The modulation wave vector is $\mathbf{q} = (\sigma_1, 1/2 + \delta, 0)$ with σ_1 and δ constituting irrational components of the wave vector. The value of σ_1 decreases from 0.08 to zero and the value of δ from 0.013 to 0.005 for decreasing crystal temperatures (Schönleber et al. (2006)). The space group of the low-temperature structures of TiOCl and TiOBr is $P2_1/m$ with the angle α being the monoclinic unique angle (Fausti et al. (2007)).

The distorted octahedral coordination of the Ti^{3+} -atoms by two halogen and four oxygen atoms with $\text{mm}2$ point group symmetry completely lifts the degeneracy of the d orbitals. The $d_{x^2-y^2}$ orbital has the lowest energy and constitutes the only occupied orbital of Ti^{3+} . The orbitals whose energy corresponds to the higher energy levels are unoccupied and are not involved in the interactions of the magnetic spin moments because the excitation energies required to transfer electrons onto them are too high (Macovez et al. (2007)). In the TiOX-structure the $d_{x^2-y^2}$ orbital is oriented along the \mathbf{b} - and \mathbf{c} -directions resulting in a direct orbital-overlap of neighboring titanium atoms along the chains of metal atoms.

Due to the large overlap, the direct exchange along \mathbf{b} is the dominating magnetic interaction in TiOX compounds and results in a spin-Peierls pairing of the magnetic moments at low-temperatures. The spin-Peierls transition, associated with the formation of spin-singlet pairs below T_{c1} , is regarded to be unconventional due to its first-order character. Superexchange interactions are generated by a hybridization

of the $d_{x^2-y^2}$ orbitals with the $2p$ orbitals of oxygen. The magnitude of the superexchange interaction was calculated to be 12 % of the spin-Peierls interaction in TiOCl and 20 % of the spin-Peierls interaction in TiOBr (Macovez et al. (2007)). Antiferromagnetic coupling is also established between the magnetic spin moments of titanium atoms on neighboring chains within one double layer.

The spin-Peierls pairing of the intermediate phase is frustrated by the effect of the Ti-O-Ti superexchange coupling and the long-range ordered antiferromagnetic interaction. As a result of the frustration the atomic displacements of the titanium atoms can deviate from the \mathbf{b} -direction (Schönleber et al. (2006); Krimmel et al. (2006)). The atomic displacements of the oxygen and chlorine atoms are almost parallel to the atomic displacements of the titanium atoms and reduce the variation of the interatomic distances in the intermediate phase. The frustration of the spin-Peierls pairing is also present in the low-temperature phase and the resulting structures represent commensurate analogues of the incommensurate structures (Schönleber et al. (2006)).

A temperature decrease of the incommensurately modulated phase effects an increase of the amount of spin-Peierls dimers resulting in parallel in a decrease of the amount of electron-singlets by which the antiferromagnetic coupling is established. In this context the transition at T_{c1} can be regarded as a collapse of the antiferromagnetic state induced by the advanced detracting of electrons (Schönleber et al. (2008)).

4.2.3 Magnetic structures of FeOCl, CrOCl and VOCl

FeOCl, CrOCl and VOCl undergo by cooling only one phase transition resulting in the formation of antiferromagnetic low-temperature phases (Adam and Buisson (1975); Christensen et al. (1975); Wiedenmann et al. (1983)). The low-temperature phase of FeOCl possesses an incommensurately modulated magnetic structure with a propagation vector of $1/2 \ 1/2 \ 0.275$ at 4.2 K (Adam and Buisson (1975)). The modulation along the \mathbf{c} -direction results from a rotation of the magnetic moments of the Fe-atoms about angles of 99 deg in the (\mathbf{b}, \mathbf{c}) plane for every translation period along \mathbf{b} .

For CrOCl the occurrence of an antiferromagnetic transition with an associated Néel-temperature of 13.5 K was revealed by a temperature-dependent measurement of the magnetic susceptibility. At the corresponding structural transition with the transition temperature $T_c = 13.5$ K the room-temperature phase transforms into a

monoclinic low-temperature phase (Chapter 7). The magnetic structure of the low-temperature phase is a fourfold superstructure of the high-temperature structure established by a quadrupling of the lattice vector \mathbf{b} (Christensen et al. (1975)).

The room-temperature phase of VOCl transforms at $T_N = 80.3$ K into a monoclinic low-temperature phase in which the monoclinic angle γ is 90.211 deg at $T = 3.2$ K (Schönleber et al. (2009)). The space group of the nuclear structure below T_N is $P112/n$. The magnetic structure of the low-temperature phase is a $2 \times 2 \times 2$ superstructure of the high-temperature structure and results from the magnetic superexchange interactions J_a along \mathbf{a} , the direct exchange interaction J_b along \mathbf{b} and a weak antiferromagnetic interaction along \mathbf{c} (Komarek et al. (2009)).

Chapter 5

Phase transition and crystal structure of the monomeric Europium(II) thiolate $\text{Eu}(\text{SC}_{36}\text{H}_{49})_2$

5.1 Introduction

Organometallic complexes of rare-earth metals have been reported with different types of chemical bonding, including interactions with σ -donor ligands (Edelmann et al. (2002)), charged π -donor ligands, like cyclopentanide (Schumann et al. (1995); Arndt and Okuda (2002)), and neutral π -arene donors (Bochkarev (2002); Giesbrecht et al. (2004)). σ - and π -bonded Organolanthanoid compounds have found applications in catalysis (Hou et al. (2003); Hultzsich et al. (2006); Marks and Hong (2004)). Understanding chemical stability and reactivity is often based on the knowledge of the crystal structures. The experimental determination of the stable crystal structure thus is important for the proper understanding of the chemical interactions in these compounds. Recently a series of organolanthanoid compounds were synthesised that contain σ -bonded interactions as well as η^6 - π -arene interactions between the lanthanoid atom and the ligands (Niemeyer (2001); Cofone and Niemeyer (2006); Hauber and Niemeyer (2007)). One of these compounds is $\text{Eu}(\text{SAr}^*)_2$ containing the ligand SAr^* with $\text{Ar}^* = 2,6\text{-Trip}_2\text{-C}_6\text{H}_3$ and $\text{Trip} = 2,4,6\text{-(isopropyl)}_3\text{C}_6\text{H}_2$ (Fig. 5.1). The earlier work reported the synthesis and the crystal structure at 173 K of solvent

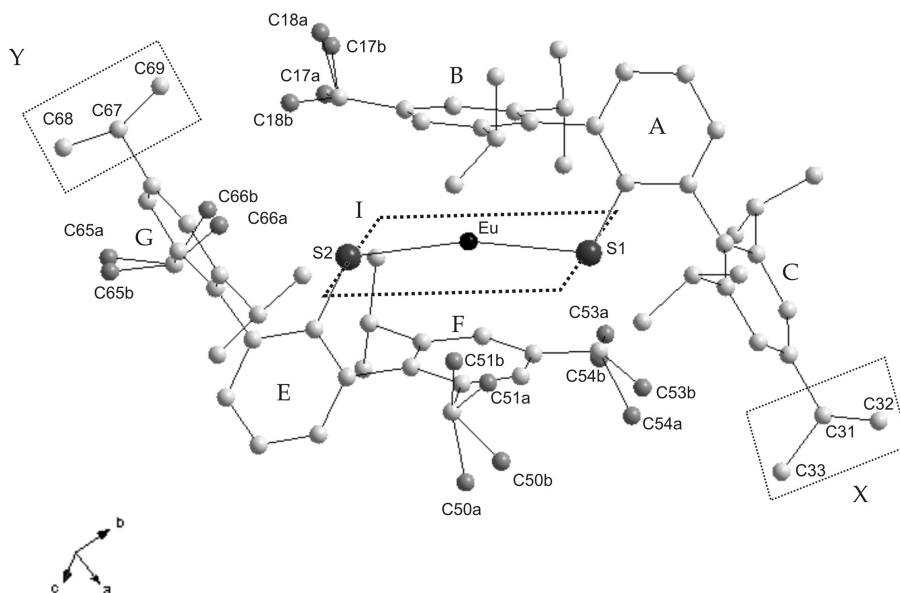


Figure 5.1: Asymmetric unit of the high-temperature structure, displayed in parallel projection. Hydrogen atoms were omitted for clarity. Medium grey atoms are disordered.

containing $\text{Eu}(\text{SAr}^*)_2 \cdot 0.5 \text{ THF}$. Here we report the results of temperature-dependent X-ray diffraction on solvent-free $\text{Eu}(\text{SAr}^*)_2$. A structural phase transition has been discovered at $T_c = 119 \pm 1 \text{ K}$, and crystal structures of the low-temperature and high-temperature phases are presented. Analysis of the crystal structures shows that an optimised crystal packing at low temperatures is the driving force for the phase transition. The Bond-Valence method is used to show that bonding between divalent europium occurs in equal amounts to the two sulphur atoms and the two phenyl rings of the ligands.

5.2 Results and Discussion

Solvent-free $\text{Eu}(\text{SAr}^*)_2$ has been crystallised as described earlier (Niemeyer (2001)). Temperature-dependent X-ray diffraction has indicated a phase transition at $T_c = 119 \pm 1 \text{ K}$, through the appearance of additional reflections in the diffraction pattern at low temperatures (Fig. 5.2). Bragg reflections appear split below T_c , pointing to the coexistence of high-temperature and low-temperature phases for at least several degrees. Together with a reduction of the volume by 1% at T_c (Table 5.1), this

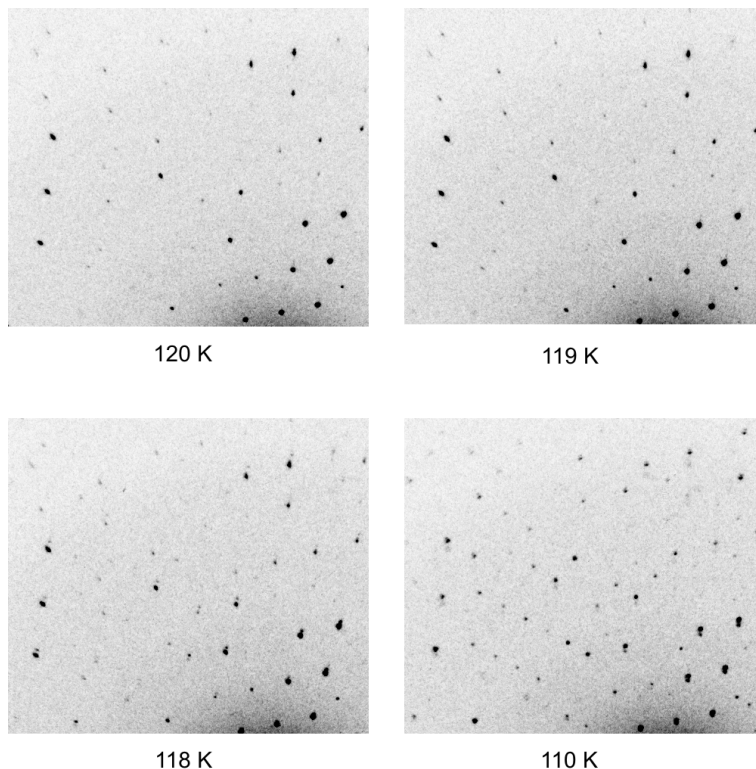


Figure 5.2: Section of the diffraction pattern at different temperatures.

suggests a first-order character of the phase transition.

The low-temperature crystal structure is found to be a twofold superstructure of the high-temperature modification. The relation between the basis vectors of the two lattices is:

$$\begin{aligned}
 \mathbf{a}_{LT} &= \mathbf{a}_{HT} + \mathbf{b}_{HT} \\
 \mathbf{b}_{LT} &= -\mathbf{c}_{HT} \\
 \mathbf{c}_{LT} &= -\mathbf{a}_{HT} + \mathbf{b}_{HT}
 \end{aligned}
 \tag{5.1}$$

The high-temperature structure contains one $\text{Eu}(\text{SAr}^*)_2$ complex in the asymmetric unit. Because both modifications crystallise in centrosymmetric triclinic space groups, the low-temperature crystal structure contains two crystallographically independent complexes. They are denoted as "molecule a" and "molecule b" in this paper. With reference to Eq. 5.1, Fig. 5.3 and the supplementary material (in this thesis provided as appendix A), atoms of molecules a and b are given the

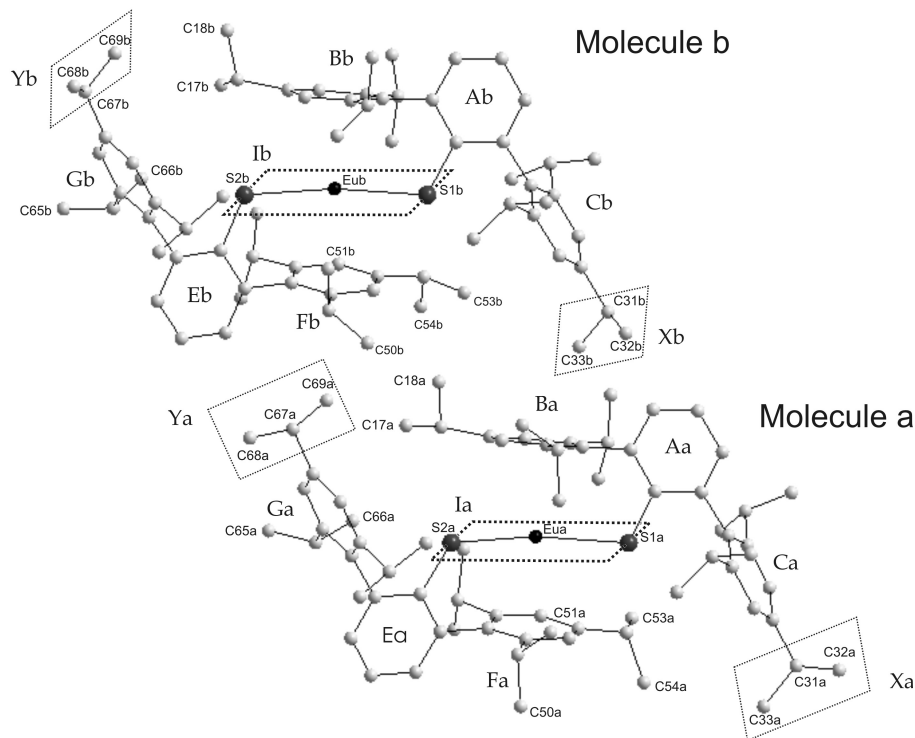


Figure 5.3: Asymmetric unit of the low-temperature structure, displayed in parallel projection. Hydrogen atoms are not shown.

same numbers as the corresponding atoms of the single independent molecule in the high-temperature phase, supplemented with "a" and "b", respectively.

Solvent-free $\text{Eu}(\text{SAr}^*)_2$ and $\text{Eu}(\text{SAr}^*)_2 \cdot 0.5$ THF crystallise in similar unit cells, while the volume of the unit cell of the latter compound is larger by $\sim 90 \text{ \AA}^3$, in order to accommodate one THF molecule. Small differences of geometrical parameters are observed, that will be discussed below. The crystal structures at high temperatures are characterised by disorder of four isopropyl groups over two orientations each (Fig. 5.1).

In the low-temperature structure, molecule a inherits one orientation of each disordered group while molecule b inherits the other orientation (Fig. 5.2). For example, atomic sites C53a, C54a, C53b and C54b of the high-temperature structure are occupied with a probability of ~ 0.5 (Fig. 5.1). In the low-temperature structure sites C53a and C54a are fully occupied in molecule a and sites C53b and C54b

are fully occupied in molecule b (Fig. 5.3). Initially, the phase transition can be described as an order-disorder transition pertaining to the isopropyl groups attached to phenyl rings B and F (Fig. 5.1).

The driving force for the phase transition is, however, the higher packing density of the low-temperature phase by 1% (Table 5.1). This is achieved not only by the ordering of the isopropyl groups but also by further conformational changes of the complexes. Most dramatically this pertains to a reorientation of isopropyl groups X and Y attached to phenyl rings C and G, respectively (Fig. 5.1). In molecule a they remain in staggered conformation with respect to the phenyl rings (angles X/C and Y/G of approximately 90 deg; see Table 5.2), but in molecule b they are rotated towards a less favourable orientation, with angles X/C and Y/G of ~ 67 deg. The higher packing density is expressed by distances between europium atoms in neighbouring complexes along the direction of \mathbf{b}_{LT} being shorter in the low-temperature than in the high-temperature structure (Table 5.2). The conformational differences pertaining to the isopropyl groups in molecules a and b and in the high-temperature structure seem to be responsible for the structural differences in other parts of the complexes. The environment of Eu in molecule a is similar to the environment in the high-temperature structure, but molecule b is different (Table 5.2).

Compared to the other structures, molecule b has slightly longer Eu–S distances and a larger angle S–Eu–S. Angles between the nearly coplanar phenyl rings B and F (defining the η^6 - π -arene bonds) and the plane I of the S–Eu–S group are slightly different for the different complexes but do not show a systematic variation.

The interplanar angles I/B and B/F are larger in $\text{Eu}(\text{SAr}^*)_2 \cdot 0.5 \text{ THF}$ than in all other structures (Table 5.2), the contribution to the valence of europium is, however, higher in the THF-containing compound, suggesting a slightly higher η^6 - π -arene interaction between Eu and both phenyl rings. A quantitative description of chemical bonding is provided by the Bond-Valence method (Brown (2002a)). The bond strength, ν_{ij} , of each pair of atoms is related to the distance, d_{ij} , between them, by the simple formula,

$$\nu_{ij} = \sum_j \exp\left(\frac{R_0 - d_{ij}}{b}\right) \quad (5.2)$$

where $b = 0.37 \text{ \AA}$ is a universal constant. Each pair of chemical elements is characterised by the value of the semi-empirical constant R_0 . The valence, V_i , of atom i is obtained as the sum of ν_{ij} over all neighbours j of i .

Table 5.1: Crystal parameters and refinement results for the high and the low-temperature phase.

Temperature	122K	100K
Empirical formula	$\text{C}_{72}\text{H}_{98}\text{EuS}_2$	$\text{C}_{72}\text{H}_{98}\text{EuS}_2$
Formula weight (g/mol)	1179.7	1179.7
Crystal diameter (mm)	0.3	0.3
Crystal system	triclinic	triclinic
Space group	$\text{P}\bar{1}$	$\text{P}\bar{1}$
a (Å)	13.303(2) ^a	17.955(2)
b (Å)	14.337(2) ^a	18.040(2)
c (Å)	18.397(2) ^a	21.177(2)
α (deg)	104.0(1) ^a	82.7(1)
β (deg)	93.9(1) ^a	85.8(1)
γ (deg)	98.8(1) ^a	76.9(1)
Volume (Å ³)	3344.8(9)	6620.0(8)
Volume/molecule (Å ³)	1672.4(5)	1655.0(3)
Z	2	4
Wavelength (Å)	0.7107	0.7107
Absorption coefficient (mm ⁻¹)	1.04	1.04
θ_{max} (deg)	30	30
Number of reflections (total)	34143	64022
Reflections (unique)	17246	33068
Reflections (observed)	16762	30082
Goodness of fit (all)	2.71	4.46
R_{int}	5.1	4.9
R_F	5.78	6.57
$R_F(h + k = \text{even})$	-	6.05
$R_F(h + k = \text{odd})$	-	7.37
$\Delta\rho_{\text{max}}$ (e/Å ³)	2.0	1.7
$\Delta\rho_{\text{min}}$ (e/Å ³)	-3.6	-2.4

^aTransformation of the high-temperature unit cell towards a twofold superstructure results in lattice parameters: $a = 18.014$ Å, $b = 18.397$ Å, $c = 20.989$ Å, $\alpha = 83.0$ deg, $\beta = 85.7$ deg, and $\gamma = 76.0$ deg; unit-cell volume: 6689.6 Å³.

Table 5.2: Selected bond lengths (Å), bond angles (deg), interplanar angles (deg) and intramolecular distances (Å). Molecule a and molecule b of the low-temperature structure are related through pseudo translational symmetry.

	100 K		122 K	173 K ^a	173 K ^b
	molecule a	molecule b			Eu(SAr*) ₂ ·THF _{0.5}
Bond lengths and bond angles^c					
Eu–S1	2.810	2.830	2.809	2.808	2.816
Eu–S2	2.803	2.818	2.804	2.813	2.818
S1–Eu–S2	139.0	143.8	137.4	138.7	141.9
⟨Eu–C(B)⟩ ^d	3.117	3.094	3.081	3.087	3.070
⟨Eu–C(F)⟩ ^d	3.078	3.094	3.067	3.076	3.059
Interplanar angles^e					
B/F	12.5	13.6	12.9	13.6	16.0
Ba/Bb		2.6	-	-	-
Fa/Fb		3.6	-	-	-
Ia/Ib		1.64	-	-	-
I/B	8.6	7.6	8.2	8.4	11.5
I/F	6.4	8.3	6.4	6.8	6.3
I/B + I/F	15.0	15.9	14.6	15.2	17.8
I/B - I/F	1.9	0.7	1.8	1.6	5.2
A/E	144.2	145.2	140.2	140.9	143.4
I/C	118.7	122.4	119.7	119.9	122.4
I/G	117.6	118.8	119.6	119.7	122.4
X/C	92.2	68.70	93.30	93.6	93.6
Y/G	87.6	66.4	82.7	82.0	80.4
Distances					
C32–C68	18.78	17.91	18.77	18.73	19.14
Eu–Eu (along b _{LT})	18.04	18.04	18.40	18.54	18.31

^aM. Niemeyer, unpublished.

^bFrom M. Niemeyer, Eur. J. Inorg. Chem. 2001, 1969-1981.

^cStandard uncertainties for the bond lengths are smaller than 0.002 Å, whereas the standard uncertainties for the bond angles are smaller than 0.1 deg.

^d⟨Eu–C⟩ is the average of six bond lengths.

^e abbreviations refer to the labeling defined in Fig. 5.1 and Fig. 5.3, and follow assignments introduced in Niemeyer (2001).

Table 5.3: Valences of europium and sulphur in the high -and the low-temperature structures.

	100 K		122 K	173 K	173 K
	molecule a	molecule b			$\text{Eu}(\text{SAr}^*)_2 \cdot \text{THF}_{0.5}$
Valence of europium					
Contribution of B	0.437	0.416	0.472	0.461	0.484
Contribution of F	0.478	0.456	0.490	0.477	0.500
Contribution of S1	0.541	0.513	0.543	0.546	0.533
Contribution of S2	0.552	0.530	0.550	0.539	0.530
total Eu	2.008	1.915	2.055	2.023	2.047
Valence of sulphur^b					
S1	-1.969	-1.893	-1.981	-1.962	-1.986
S2	-1.927	-1.854	-1.983	-1.974	-1.966

^aValences have been calculated with Bond-valence parameters $R^0(\text{C}^{\text{IV}}-\text{S}) = 1.800 \text{ \AA}$, $R^0(\text{Eu}^{\text{II}}-\text{S}) = 2.583 \text{ \AA}$ and $R^0(\text{Eu}^{\text{II}}-\text{C}(\pi\text{-bonded})) = 2.135 \text{ \AA}$.

^bContributions of C-atoms with distances greater 4 \AA and contributions of H-atoms were neglected.

The Bond-Valence method is a standard method in Inorganic Chemistry, and bond-valence parameters R_0 have been tabulated for all pairs of elements (O’Keeffe and Brese (1991b)). However, inorganic and organometallic compounds require different sets of parameters R_0 (Palenik (1997; 2003)). Furthermore, different valence states may require different bond-valence parameters. Here, we have used values of R_0 derived by Trzesowska *et al.* (Trzesowska (2006); Trzesowska *et al.* (2004)) for $\text{Eu}^{\text{II}}-\text{S}$ and $\text{Eu}^{\text{II}}-\text{C}$,¹ and by Brown (Brown (2006)) for $\text{C}^{\text{IV}}-\text{S}$. Application to the low- and the high-temperature structures shows that a valence of two is well reproduced for Eu and for S in all structures (Table 5.3). More precisely, computed valences of Eu and both S atoms in molecule b are smaller by approximately 0.1 valence units than valences in molecule a and in the high-temperature structure.

¹The bond-valence parameters R_0 as reported in Trzesowska (2006) for $\text{Eu}-\text{O}$ and $\text{Eu}-\text{N}$ are 0.065 \AA longer for Eu^{II} than for Eu^{III} . For $\text{Eu}-\text{S}$ only the value $R_0 = 2.517 \text{ \AA}$ for Eu^{III} has been reported. By analogy we have used $R_0(\text{Eu}^{\text{II}}-\text{S}) = 2.517 \text{ \AA} + 0.066 \text{ \AA} = 2.583 \text{ \AA}$.

This again supports the interpretation of a less favourable conformation of molecule b as compared to the other structures. Consideration of individual contributions to the valence of Eu shows that bonding of equal magnitude is present towards both S atoms as well as both phenyl rings. Sulphur, on the other hand, derives a substantial part of its valence from incidental S-C interactions other than the apparent single S-C σ -bond (Table 5.2, Fig. 5.1).

The assignment of a coordination number for the europium atom in both phases is not straightforward. Taking into account the additional π -contacts, a formal coordination number of eight is calculated. However, the observed Eu-S distances are surprisingly short. In fact, they are approx. 0.08-0.13 Å shorter than the corresponding values reported for other Eu^{II} thiolates that contain six- or eight-coordinate europium atoms (Hargittai (2000); Kaupp (2001)).

From these data a lower effective coordination number of approximately 4 may be estimated for the europium atom in Eu(SAr*)₂, assuming that every η^6 -bonded arene ring occupies only one coordination site. This view is supported by the above-mentioned analysis of the bonding valences which shows roughly equal contributions by the two sulphur atoms and the two pending arene rings, respectively.

The occurrence of bent equilibrium geometries for lanthanide MX₂ species in the gas phase is now well established (Hargittai (2000); Kaupp (2001)). The bending can be explained by contributions of metal *d* orbitals to the σ -bonding and by the polarization of the metal cation by the ligands (Kaupp (2001)). According to Kaupp *et al.* (Kaupp (2001)) the MX₂ compounds can be divided into molecules with genuinely bent structures, for example the gas phase structure of EuF₂, and molecules with quasi-linear equilibrium geometries, for example SmCp₂ or CaF₂. The latter show almost no energy change (less than 1-2 kJ mol⁻¹) when the equilibrium angle is increased to 180 deg, whereas the former exhibit considerable linearization energies of up to 33 kJ mol⁻¹.

With a linearization energy of only 1.1 kJ mol⁻¹, calculated at MP2/6-31+G** level of theory, the model compound Yb(SH)₂ can be classified as a quasi-linear molecule (Niemeyer (2001)). According to further quantum-chemical calculations and low-temperature NMR experiments, metal- π -arene interactions to flanking arene rings in some Eu^{II} or Yb^{II} compounds are in the range 40-55 kJ mol⁻¹ (Niemeyer (2001); Hauber and Niemeyer (2005)). Therefore, the bent S-Eu-S angle in the different phases of Eu(SAr*)₂ clearly originates from the additional Eu... π -arene interactions and not from other intrinsic electronic factors.

5.3 Conclusions

A low-temperature structural phase transition has been discovered in crystals of solvent-free $\text{Eu}(\text{SAr}^*)_2$ at $T_c = 119 \pm 1$ K. The volume per molecule reduces by 1% at the phase transition. Accordingly, an optimised packing is identified as driving force for the phase transition. A denser packing of complexes $\text{Eu}(\text{SAr}^*)_2$ is achieved at the expense of a less favourable conformation of one of the two crystallographically-independent complexes in the low-temperature phase. This interpretation is supported by the Bond-Valence method, that indicates a slightly under-bonded character of Eu in the strained complex.

5.4 Experimental Section

Synthesis and crystallisation of $\text{Eu}(\text{SC}_{36}\text{H}_{49})_2$ as a 0.5 THF hemisolvant was described in (Niemeyer (2001)). Crystals of the solvent-free compound were obtained by crystallisation from *n*-heptane at -15 °C. The crystals were handled in inert atmospheres (argon and nitrogen). For the first diffraction experiment a crystal was selected and mounted under the cryoprotectant oil Paratone-N. X-ray diffraction was measured on a MARRESEARCH DTB MAR345 image plate diffractometer, equipped with a rotating anode X-ray generator (50 kV, 100 mA) and a graphite monochromator selecting Mo- K_α radiation. The crystal was cooled by a OXFORD nitrogen gas flow cooling. A datacollection was performed at $T=122$ K by a series of 360 phi scans with 0.5 deg rotation per image. Lattice parameters and integrated intensities of Bragg reflections were extracted with the software package XDS (Kabach (1993)) (Table 5.1). Data were merged according to Laue symmetry $\bar{1}$ in the computer program JANA2000, which was also used for refinement (Petricek et al. (2000)).

Starting with the non-hydrogen atom positions from Niemeyer (2001), structure refinements converged smoothly to a fit to the data of $R = 0.067$. Hydrogen atoms were inserted at distances of 0.95 Å from carbon at calculated positions, finally resulting in $R = 0.058$. The 172 K structure of Niemeyer (2001) was confirmed, including disorder over two orientations for each of the methyl groups defined by carbon atoms C17, C18, C50, C51, C53, C54, C65, C66 (Fig. 5.1). Three crystals were cooled to temperatures below 119 K. At these temperatures the diffraction images contained many more maxima than those measured at 122 K, while reflections had a split appearance. It was concluded that the crystals had suffered damage due

to a phase transition around 119 K. Indexing of these images failed. Therefore another crystal was mounted for diffraction, now glued to a glass hair and handled in nitrogen gas flow. Diffraction of this crystal was measured at different temperatures between 125 K and 115 K in steps of 0.5 K, in order to determine the transition temperature more accurately.

A data collection was performed at a temperature of 100 K. Reflections had a split appearance, but the damage to the crystal was much less than for the crystal mounted in Paratone-N. Indexing of the data showed that the low-temperature phase has a twofold supercell of the high-temperature phase. Lattice parameters and integrated intensities were determined by the software CRYSTALIS RED (171.27p23) (*Software CrystAlis RED* (2005)), because split reflections are much better handled by CRYSTALIS RED than by XDS. Intensity data were merged by JANA2000 according to Laue symmetry $\bar{1}$. The crystal structure was solved by Direct Methods employing SIR2002 (Burla et al. (2001)), and subsequently refined by JANA2000. The relatively high R-values can be explained by the less than optimal data quality due to the damage of the crystal. Atoms were named according to the independent atoms of the high-temperature structure. All atoms of molecule a of the low-temperature structure are indicated by "a", while those of the molecule b are indicated by the ending "b". Absorption correction was not made, because the crystal shape could not be determined and the absorption coefficient was small ($\mu = 1.04 \text{ mm}^{-1}$).

Chapter 6

Low- and high-temperature crystal structures of TiI_3

6.1 Introduction

The crystal structures of transition metal halides can be characterized by a closest packed arrangement of halogen atoms with the metal atoms occupying one-third of the octahedral interstitial sites. In fluorides the metal atoms are homogeneously distributed in space, while in the other halides they are concentrated in layers or chains that are separated from each other by regions containing the empty octahedral sites (Lin and Miller (1993)).

The TiI_3 structure type comprises chains of equidistant metal atoms that are arranged parallel to the unique axis of a hexagonal closest packing (hcp) of iodine atoms (Figs. 6.1 and 6.2) Dahl et al. (1964). This ordered arrangement of occupied and vacant octahedral sites possesses translational symmetry according to a three-fold supercell of the hcp structure, with lattice parameters $a_h = \sqrt{3}a_{hcp}$ and $c_h = c_{hcp}$, and with the space group $P6_3/mcm$.

RuBr_3 crystallizes in a twofold superstructure of the TiI_3 structure type, which is characterized by the presence of dimers within the chains of metal atoms (Brodersen, Breitbach and Thiele (1968)). The stability of the RuBr_3 structure type as opposed to the TiI_3 structure type has been attributed to the presence of metal-metal bonds in the former structure (Lachgar et al. (1990); Dorhout and Corbett (1991)). Alternatively, the origin of the dimerization has been ascribed to the Peierls mechanism, involving quasi-one-dimensional (1D) electron bands on the chains of metal atoms (Lin and Miller (1993)).

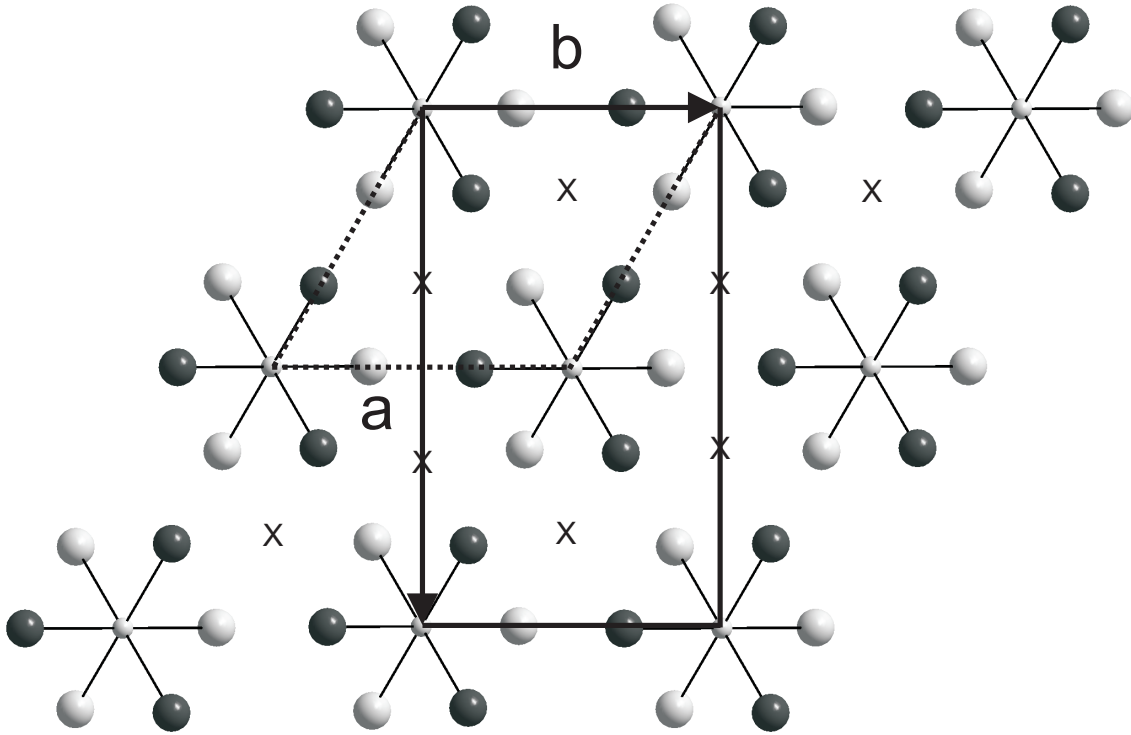


Figure 6.1: Projection of the crystal structure of TiI_3 along \mathbf{c} . The orthorhombic unit cell of the low-temperature structure (solid lines) is related to the hexagonal unit cell of the high-temperature structure (dotted lines) by the relations: $\mathbf{a}_o = 2\mathbf{a}_h + \mathbf{b}_h$, $\mathbf{b}_o = \mathbf{b}_h$ and $\mathbf{c}_o = \mathbf{c}_h$. Small spheres represent titanium atoms and big spheres iodine atoms. The z -coordinate of the dark iodine atoms is shifted by 0.5 from the z -coordinate of the light iodine atoms. Unoccupied octahedral sites are marked by crosses.

RuBr_3 is orthorhombic with space group $Pmnm$ and lattice parameters $a_o = \sqrt{3}a_h$, $b_o = b_h$ and $c_o = c_h$ that define the orthohexagonal unit cell of the TiI_3 lattice (Fig. 6.1) (Brodersen, Breitbach and Thiele (1968)). The orthorhombic distortion of the hexagonal lattice is expressed in the diffraction by the presence of weak superlattice reflections at $(h + \frac{1}{2}, k, l)_h$ (the subscript h indicates an indexing with respect to the hexagonal lattice). Most crystals, however, are twinned with the orthorhombic structure occurring in three orientations on the hexagonal lattice (Babel (1972)). While main reflections $(h, k, l)_h$ are common to the three domains, each twin domain gives rise to its own set of superlattice reflections, at $(h + \frac{1}{2}, k, l)_h$, $(h, k + \frac{1}{2}, l)_h$ and $(h - \frac{1}{2}, k + \frac{1}{2}, l)_h$, respectively.

The superlattice reflections are weak and they have been overlooked in initial

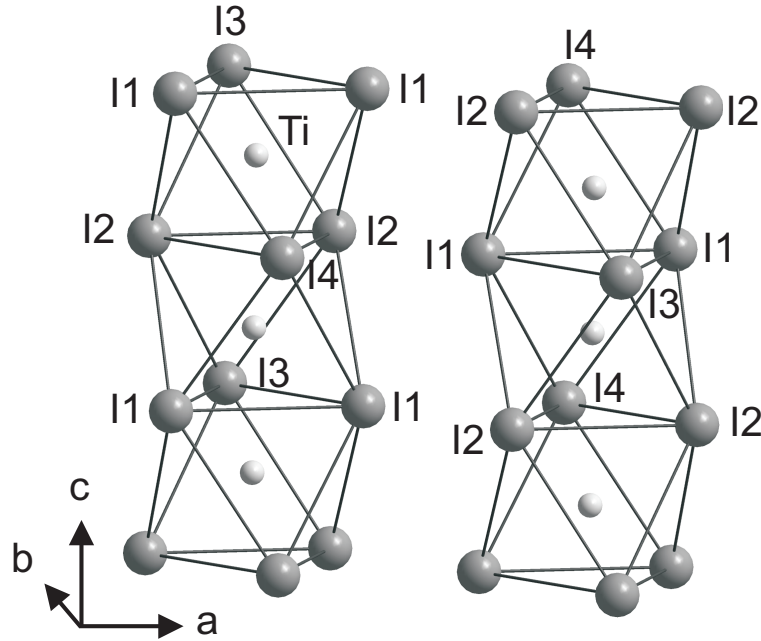


Figure 6.2: Chains of face sharing TiI_3 -octahedra are oriented parallel to lattice direction c . Atoms are labeled according to Table 6.6.

studies on materials belonging to this class of compounds. It could thus be presupposed that all compounds for which the hexagonal structure has been found would actually crystallize in the RuBr_3 structure type. However, the question about the "true" crystal structures of transition metal halides was resolved by the notion of a phase transition between the RuBr_3 and TiI_3 structure types (Lachgar et al. (1990)). Accordingly, high-temperature (TiI_3 type) and low-temperature (RuBr_3 type) structures have now been reported for RuBr_3 , RuCl_3 and MoBr_3 (Hillebrecht et al. (2004); Merlino et al. (2004)). Depending on the compound, transition temperatures have been found to be higher or lower than room temperature (Table 6.1).

The compound TiI_3 exhibits superlattice reflections in its diffraction pattern at room temperature, reflecting the RuBr_3 structure type (von Schnering (1966)). The only published structure of TiI_3 is a refinement of the hexagonal substructure against the main reflections (von Schnering (1966)). Here we report the discovery of a phase transition between the TiI_3 and RuBr_3 structure types at $T_c = 323 \pm 2$ K and we present accurate crystal structures of both the high-temperature and low-temperature forms. These results are analyzed in view of the mechanism of the phase transitions in transition metal halides.

Table 6.1: Compounds with the orthorhombic RuBr₃ structure type at low temperatures and the hexagonal TiI₃ structure type at high temperatures. Indicated are the temperatures at which the structures have been determined as well as the transition temperature (T_c).

	RuBr ₃ structure type			T_c (K)	TiI ₃ structure type			Reference
	T (K)	a_o (Å)	b_o (Å)		c_o (Å)	T (K)	a_h (Å)	
β -TiCl ₃	-	-	-	-	RT ^a	6.270	5.820	Natta et al. (1961)
β -TiBr ₃	-	-	-	-	RT ^a	6.595	6.095	Newland and Shelton (1970)
TiI ₃	273	12.361(1)	7.137(1)	6.508(1)	323	326	7.142(1)	6.510(1) [*]
RuCl ₃	170	10.576(2)	6.106(1)	5.634(1)	206	293	6.121(2)	5.655(2)
RuBr ₃	293	11.256(2)	6.499(1)	5.873(2)	377.5	423	6.522(2)	5.885(2)
RuI ₃	-	-	-	-	RT ^a	6.982	6.231	von Schnering et al. (1966)
MoBr ₃	RT	11.442(2)	6.605(1)	6.077(1)	466.1	-	-	Babel (1972); Merlino et al. (2004)
MoI ₃	-	-	-	-	RT ^a	7.115	6.420	Hillebrecht et al. (2004)
ZrCl ₃	-	-	-	-	RT ^a	6.383(1)	6.139(2)	Larsen et al. (1982)
ZrBr ₃	-	-	-	-	RT ^a	6.728(1)	6.299(2)	Larsen et al. (1982); Kleppinger et al. (1975)
ZrI ₃	293	12.594(6)	7.292(2)	6.679(2)	-	-	-	Lachgar et al. (1990)
HfI ₃	-	-	-	-	RT ^a	7.225	6.59	Dahl et al. (1964)
OsI ₃	-	-	-	-	RT ^a	6.93	6.26	Schäfer et al. (1971)
NbI ₃	-	-	-	-	RT ^a	6.61	6.82	Hillebrecht et al. (2004)

[*] This work.

RT denotes room temperature.

^aSuperstructure reflections were not reported, but it cannot be excluded that they were overlooked.

6.2 Experimental section

TiI₃ was obtained as the result of an unsuccessful attempt to synthesize TiOI. Stoichiometric amounts of TiO₂ (Strem, 99.99%), Ti (Alfa, 99.99%) and I₂ (Alfa, 99.99%) were sealed in an evacuated quartz glass tube. This tube was placed in a temperature gradient of 923 K at the educt side and 823 K at the product side; reaction time was five days. The product consisted of pinkish-red plates, dark violet grains and black needles of several millimeters in length. The crystals were identified as TiI₂, Ti₂O₃ and TiI₃, respectively. Because TiI₃ reacts with air, the material was handled under argon and nitrogen inert atmospheres.

Two single-crystals of TiI₃ were selected for X-ray diffraction experiments on a MAR345 image plate diffractometer. Crystals were mounted with the aid of vacuum grease (Krytox, DuPont) on polyamide mounts (MiTeGen, Thorne et al. (2003)). The crystal temperature was regulated with a cryostream nitrogen-gas-flow cryostat, which also provided the inert atmosphere for the sample during the diffraction experiment. Diffraction data were measured by ϕ -scans of 0.5 deg wide. Data sets on the low-temperature phase were thus collected at temperatures of 100 K and 273 K. Two runs appeared necessary for each data collection: one with an exposure time of 480 s per frame and a second one with 60 s per frame. The latter run provided the intensities of reflections that were overexposed in the first run.

The software CrysAlis was used for data processing, including absorption correction (*Software CrysAlis RED* (2005)). Strong reflections in the data collected at both temperatures could be indexed on the basis of the hexagonal unit cell proposed by von Schnering (von Schnering (1966)) with $a_h = b_h = 7.0857(5)$ Å and $c_h = 6.4817(4)$ Å at $T = 100$ K. Much weaker reflections correspond to an apparent hexagonal $2a_h \times 2b_h \times c_h$ superlattice.

In a second experiment short runs of 10 frames each were measured temperature dependent up to 325 K (Fig. 6.3). Superlattice reflections were found to be present on the images up to 321 K. Some weak scattering might be present at these positions at $T = 323$ K, while the superlattice reflections were definitely absent at 325 K (Fig. 6.3). A complete data set was then measured at a temperature of 326 K. Data processing with CrysAlis indicated that all Bragg reflections could be indexed by the $a_h \times b_h \times c_h$ unit cell. These results are in accordance with the occurrence of a first-order phase transition in TiI₃ at a temperature of $T_c = 323 \pm 2$ K. Details on the experiments and data are given in Table 6.2.

Table 6.2: Experimental data of the TiI_3 structure for different temperatures.

Temperature (K)	100	273	326
Formula weight (g/mol)	428.59	428.59	428.59
Crystal shape (mm^3)	$0.05 \times 0.05 \times 0.3$	$0.03 \times 0.07 \times 0.35$	
Crystal system	orthorhombic	orthorhombic	hexagonal
Space group	$Pmnm$	$Pmnm$	$P6_3/mcm$
a (\AA)	12.2728(7)	12.3609(7)	7.1416(5)
b (\AA)	7.0857(5)	7.1365(5)	7.1416(5)
c (\AA)	6.4817(4)	6.5083(4)	6.5102(4)
Volume (\AA^3)	563.7	574.1	287.6
Z	4	4	2
Calculated density (g/cm^3)	5.05	4.96	4.95
Detector distance (mm)	80	80	80
Wavelength (\AA)	0.71069	0.71069	0.71069
Absorption coefficient (mm^{-1})	17.78	17.45	17.43
θ_{max} (deg)	32.2	32.2	32.2
ϕ -range (deg)	180	180	150
Number of measured reflections	18025	13915	2636
main	4896	3428	2636
superlattice	13129	10487	–
Number of unique reflections (all)	6800	6893	201
main	1742	1738	201
superlattice	5058	5155	–
Number of unique reflections (obs.)	5478	4890	199
main	1621	1585	199
superlattice	3857	3305	–
R_{int}	0.0273	0.0258	0.0249
wR_F^2 (observed)	0.0988	0.1150	0.0312
main	0.0729	0.1116	0.0312
superlattice	0.1223	0.1195	–
R_F (observed)	0.0585	0.0690	0.0137
main	0.0361	0.0530	0.0137
superlattice	0.1171	0.1122	–
GoF (observed)	3.33	3.90	1.52
relative twin volumes	0.19/0.23/0.58	0.45/0.23/0.32	–
$\Delta\rho_{\text{max}}$ (e/\AA^3)	2.22	2.20	0.45
$\Delta\rho_{\text{min}}$ (e/\AA^3)	-2.47	-1.47	-0.49

The reflection intensities of the low-temperature measurements were averaged according to Laue symmetry $\bar{1}$.

R -values were calculated through the expressions $R_F = (\sum ||F_{\text{obs}}| - |F_{\text{cal}}|| / \sum |F_{\text{obs}}|)$ and $wR_F^2 = (\sum w (|F_{\text{obs}}| - |F_{\text{cal}}|)^2 / \sum w |F_{\text{obs}}|^2)^{1/2}$ with $w = 1/((\sigma_{F_{\text{obs}}})^2 + (p|F_{\text{obs}}|)^2)$, in which p is the instability factor.

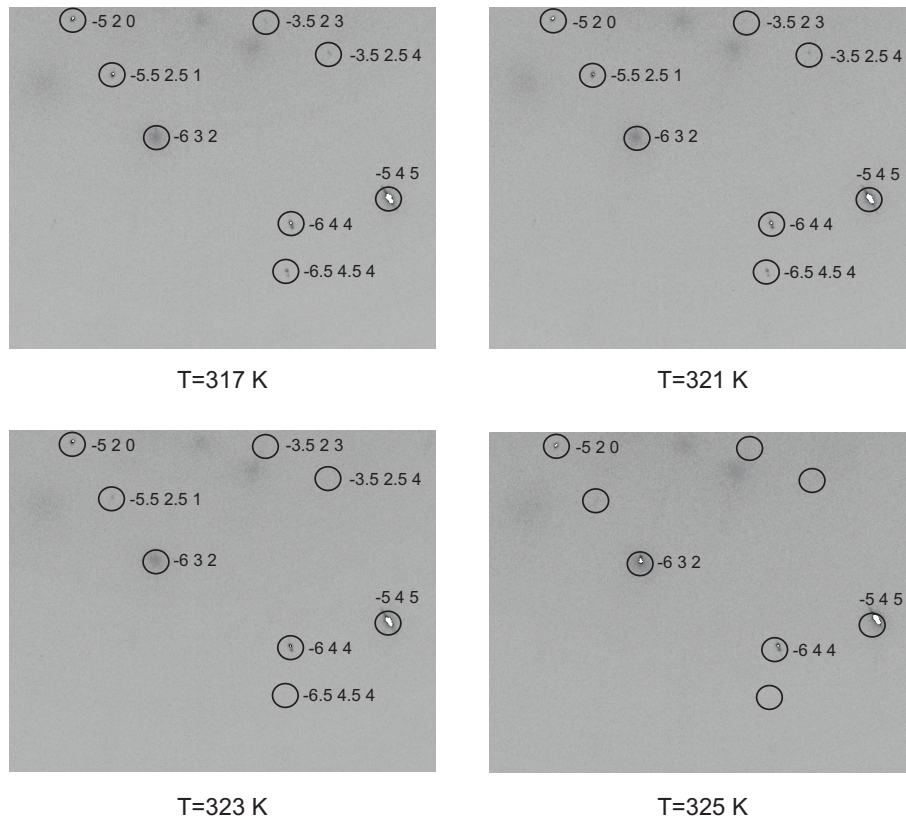


Figure 6.3: Sections of MAR345-image plate frames exposed over a ϕ -range of 1.5 deg. The pictures show reflection spots of the same region obtained for different crystal temperatures. The indices refer to the hexagonal unit cell $\{\mathbf{a}_h, \mathbf{c}_h\}$.

6.3 Structure refinements

The high-temperature crystal structure of TiI_3 was refined against the data measured at $T = 326$ K. The data were averaged in Laue symmetry $6/mmm$. An excellent fit to these data was obtained in the space group $P6_3/mcm$, with the model of von Schnering (von Schnering (1966)) as start parameters. All refinements were performed with Jana2000 (Petricek et al. (2000)).

The low-temperature phase appeared to be orthorhombic with a primitive, orthohexagonal unit cell (Table 6.2). All superlattice reflections could be explained on the assumption of a threefold twinned crystal. With respect to the orthorhombic unit cell of the first domain, the superlattice reflections of the second and third domains have half-integer indices (Section 6.1), preventing their use in the refinement

Table 6.3: Relative atomic coordinates and equivalent isotropic atomic displacement parameters (\AA^2) for the high-temperature structure at $T = 326$ K.

	\mathbf{x}	\mathbf{y}	\mathbf{z}	U_{eq}
Ti	0	0	0	0.0243(3)
I	0.31705(4)	0	0.25	0.0246(2)

with Jana2000. Integer indices for all reflections are obtained with the hexagonal $2a_h \times 2b_h \times c_h$ superlattice (Section 6.2). Orthorhombic symmetry is then recovered by the non-standard centering translation $(0, 1/2, 0)$. The latter setting was thus used for the refinement of the orthorhombic superstructure against the complete data set, taking into account the twinning. It appeared necessary to reduce the Laue symmetry of the data to $\bar{1}$, in order to allow for unequal volumes of the domains—as it proved to be the case. The shifts of the atoms towards the superstructure positions were found by the refinement using starting values of the high-temperature structure. A reasonable fit to the diffraction data was found in space group $Pmnm$ (Table 6.2), but R -values were substantially higher than for the refinement of the hexagonal structure against the high-temperature data. Atomic coordinates of the high-temperature structure are given in Table 6.3; Table 6.4 provides the atomic coordinates of the low-temperature structures with respect to the orthorhombic lattices defined in Table 6.2.

Motivated by the discrepancy—especially for the superlattice reflections—between calculated and observed structure factors, structure solution was tried in several orthorhombic and monoclinic space groups (Table 6.5). Other centrosymmetric orthorhombic space groups lead to a worse fit to the data, while an improvement of the fit could not be obtained in subgroups of $Pmnm$. We therefore conclude that the low-temperature form of TiI_3 has $Pmnm$ symmetry.

It is noticed the space groups $P6_3/mcm$ and $Pmnm$ have previously been reported for RuBr_3 and RuCl_3 and MoBr_3 (Brodersen, Breitbach and Thiele (1968); Hillebrecht et al. (2004); Merlino et al. (2004)), and that a similar problem of high R -values was reported for these compounds as well as for the $Pmnm$ structure of ZrI_3 (Lachgar et al. (1990); Hillebrecht et al. (2004); Merlino et al. (2004)). A possible origin for the relatively high R -values might be sought in the contribution of twin boundaries—including elastic distortions of the bulk near these boundaries—to the diffracted intensities.

Table 6.4: Relative atomic coordinates and equivalent isotropic atomic displacement parameters (\AA^2) for the low-temperature structures at $T = 100$ K and at $T = 273$ K. Coordinates are given with respect to the orthorhombic lattice (Table 6.2), with the origin of $Pmnm$ at $m2/nm$.

	x	y	z	U_{eq}
100 K				
Ti	0	-0.24646(9)	-0.22847(10)	0.0081(3)
I1	0.16325(3)	-0.40850(7)	0	0.0088(2)
I2	0.65710(4)	0.09157(8)	0	0.0088(2)
I3	0	0.07923(7)	0	0.0099(2)
I4	0.5	0.56006(8)	0	0.0093(2)
273 K				
Ti	0	-0.24678(10)	-0.22867(12)	0.0197(5)
I1	0.16255(4)	-0.40649(10)	0	0.0239(3)
I2	0.65674(5)	0.09330(10)	0	0.0241(3)
I3	0	0.07632(8)	0	0.0246(4)
I4	0.5	0.55894(10)	0	0.0230(3)

Table 6.5: R -values of refinements of the low-temperature structure at 100 K in different space groups. The value of R_F is given for all reflections, for the main reflections and for the superlattice reflections.

Space group	Reflection group		
	All	Main	Superlattice
$P6_3/mcm$	-	0.0391	-
$Pmnm$	0.0585	0.0361	0.1172
$P2_122_1$	0.0562	0.0341	0.1133
$Pmn2_1$	0.0549	0.0350	0.1066
$P2_1nm$	0.0552	0.0347	0.1085
$P12/n1$	0.0582	0.0357	0.1171
$P1n1$	0.0536	0.0347	0.1031
$P121$	0.0535	0.0337	0.1050
$P\bar{1}$	0.0550	0.0336	0.1104
$Pmnn$	0.1736	0.1174	0.3355
$Pmcn$	0.1760	0.0653	0.5086
$Pmcm$	0.2099	0.0848	0.5484
$Pbnn$	0.1676	0.0558	0.5034
$Pbnm$	0.1698	0.0625	0.4614
$Pbcn$	0.1978	0.0898	0.5369
$Pbcm$	0.1593	0.0542	0.4565

$$R_F \text{ is defined as } R_F = \frac{\sum ||F_{obs}| - |F_{cal}||}{\sum |F_{obs}|}.$$

6.4 Discussion

6.4.1 TiI_3 and RuBr_3 structure types

A phase transition in TiI_3 has been found to occur at $T_c = 323 \pm 2$ K. Structure refinements establish that TiI_3 crystallizes in the TiI_3 structure type at high temperatures. Below T_c , *i.e.* at room temperature, TiI_3 crystallizes in the RuBr_3 structure type. The orthorhombic distortion follows the same pattern as it has been previously described for ZrI_3 , RuBr_3 , RuCl_3 and MoBr_3 (Brodersen, Breitbach and Thiele (1968); Lachgar et al. (1990); Hillebrecht et al. (2004); Merlino et al. (2004)). Major effect is the formation of dimers along the chains of metal atoms (Figs. 6.2, 6.4). Halogen atoms are displaced such as to keep the metal–halogen distances as equal as possible (Table 6.6 and Lachgar et al. (1990)).

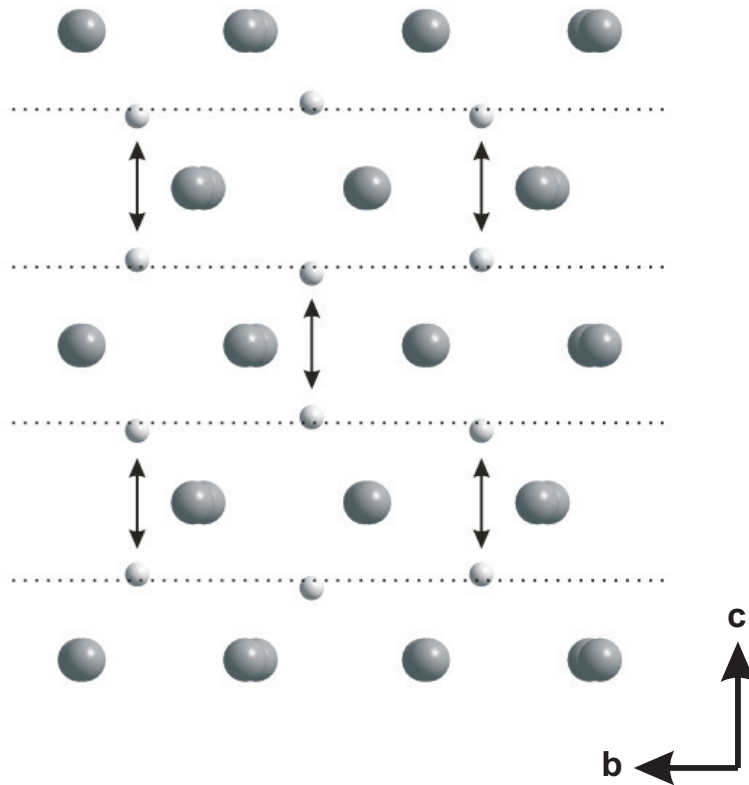


Figure 6.4: Pairing of Ti-atoms in the low-temperature structure of TiI_3 . The low-temperature structure (100 K) is projected along \mathbf{a}_0 . Dotted lines indicate positions with $z = 0$ and $z = 1/2$. Dimerization of Ti atoms is indicated by arrows.

Table 6.6: Selected interatomic distances (\AA) and bond angles (deg) at different temperatures. Standard uncertainties are smaller than 0.002 \AA in the distances and smaller than 0.05 deg in the angles. The atom labeling is the same as in Fig. 6.2.

	100 K	273 K	326 K
Intrachain distances			
Ti-Ti	3.520	3.532	3.255
	2.962	2.977	3.255
Ti-I1 (2 \times)	2.743	2.748	2.789
Ti-I2 (2 \times)	2.832	2.841	2.789
Ti-I3	2.742	2.744	2.789
Ti-I4	2.835	2.843	2.789
I1-I1	4.007	4.019	3.922
I1-I2 (2 \times)	3.944	3.949	3.965
I1-I3 (2 \times)	3.995	3.989	3.922
I1-I4 (2 \times)	3.959	3.976	3.965
I2-I2	3.856	3.875	3.922
I2-I3 (2 \times)	3.960	3.976	3.965
I2-I4 (2 \times)	3.839	3.847	3.922
Interchain distances			
I1-I1	4.089	4.129	4.174
I1-I2	4.173	4.209	4.228
I1-I2	4.173	4.211	4.228
I1-I3 (2 \times)	4.146	4.202	4.228
I1-I4 (2 \times)	4.139	4.179	4.228
I2-I2	4.170	4.205	4.174
I2-I3 (2 \times)	4.209	4.245	4.228
I2-I4 (2 \times)	4.231	4.277	4.228
I3-I4 (2 \times)	4.127	4.167	4.174
Bond angles			
I1-Ti-I1	93.83	93.97	89.37
I1-Ti-I2 (2 \times)	90.03	89.88	90.63
I1-Ti-I3 (2 \times)	93.48	93.14	89.37
I1-Ti-I4 (2 \times)	90.41	90.65	90.63
I2-Ti-I2	85.82	85.99	89.37
I2-Ti-I3 (2 \times)	90.54	90.75	90.63
I2-Ti-I4 (2 \times)	85.29	85.18	89.37
Ti-I1-Ti (2 \times)	65.34	65.58	71.42
Ti-I2-Ti (2 \times)	76.85	76.86	71.42
Ti-I3-Ti	65.38	65.68	71.42
Ti-I4-Ti	76.76	76.81	71.42

The driving force for the formation of the twofold superstructure of the TiI_3 structure type has been identified as metal–metal bonding along the chains of metal atoms (Lachgar et al. (1990)). At the same time the role of direct metal–metal bonding was questioned, because the transition metal triiodides have been found to crystallize more likely in the RuBr_3 structure type than the chlorides do, although chlorides possess shorter metal–metal distances and concomitantly stronger metal–metal bonds than the corresponding iodides. Instead, the importance was stressed of metal–metal interactions via the metal–halogen bonds (Lin and Miller (1993); Lachgar et al. (1990)).

Insight into this issue can be obtained from atomic valences as they can be computed from the structure models by the bond-valence method (Brown (2002b); Brese and O’Keeffe (1991)). We have calculated bond valences for the three structures of TiI_3 reported here as well as for the high-temperature and low-temperature structures of RuBr_3 and RuCl_3 (Hillebrecht et al. (2004)). If only cation–anion interactions are taken into account the bond-valence model should lead to valence three for the metal atoms and valence one for the halogen atom. This is found to be the case for the high-temperature forms of TiI_3 and RuBr_3 (Table 6.7). For the atom pair Ru–Cl a bond-valence parameter R_0 is only available for four-valent Ru, with value $R_0(\text{Ru}^{\text{IV}}-\text{Cl}^{\text{I}}) = 2.21 \text{ \AA}$ (Brese and O’Keeffe (1991)). With this value a valence of 4.2 was obtained for Ru, which cannot be correct as is also indicated by the valence of 1.39 for Cl. We have therefore employed a value of $R_0(\text{Ru}^{\text{III}}-\text{Cl}^{\text{I}}) = 2.10 \text{ \AA}$, which was chosen to lead to a valence of three for Ru in the high-temperature crystal structure of RuCl_3 (Table 6.7). A difference of 0.11 \AA between the bond-valence parameters of the three-valent and four-valent states of an element is untypical for the bond-valence method (Brown (2002b)), and one could suppose that the published value (Brese and O’Keeffe (1991)) for $R_0(\text{Ru}^{\text{IV}}-\text{Cl}^{\text{I}})$ is actually in error.

Computed atomic valences in the RuBr_3 type structure are also close to three for the metal atoms in the low-temperature crystal structures of TiI_3 , RuBr_3 and RuCl_3 . Half of the halogen atoms appear slightly underbonded and half of them slightly overbonded, with an average valence of one (Table 6.7).

Cation–cation and anion–anion interactions can also be described by the bond-valence method, and bond-valence parameters for these interactions have been derived by O’Keeffe *et al.* (O’Keeffe and Brese (1991a; 1992)). They constitute an additional contribution to the bonding of each atom. The meaning of the anion–anion bond-valences is not clear to us, because they suggest that the valence of the halogen atoms would be larger than 1. For the metal atoms, however, the additional

Table 6.7: Atomic valences of MX_3 compounds ($\text{M} = \text{Ti, Ru}$; $\text{X} = \text{Cl, Br, I}$) as computed by the bond-valence method Brown (2002b); Brese and O’Keeffe (1991).

	TiI₃			RuBr₃^a		RuCl₃^a	
	100 K	273 K	326 K	LT	HT	LT	HT
Valence of M	3.464	3.399	3.346	3.720	3.623	3.826	3.794
Contribution of M	0.370	0.356	0.274	0.548	0.486	0.768	0.684
Contribution of X	3.094	3.043	3.072	3.170	3.132	3.058	3.090
Valence of X1 (2×)	-1.434	-1.411	-1.274	-1.400	-1.316	-1.286	-1.255
Contribution of M	-1.156	-1.140	-1.024	-1.124	-1.044	-1.070	-1.031
Contribution of X	-0.278	-0.271	-0.250	-0.274	-0.272	-0.214	-0.224
Valence of X2 (2×)	-1.207	-1.170	-1.274	-1.280	-1.316	-1.192	-1.255
Contribution of M	-0.908	-0.886	-1.024	-0.990	-1.044	-0.960	-1.031
Contribution of X	-0.299	-0.284	-0.250	-0.290	-0.272	-0.232	-0.224
Valence of X3	-1.437	-1.416	-1.274	-1.402	-1.316	-1.314	-1.255
Contribution of M	-1.159	-1.152	-1.024	-1.128	-1.044	-1.104	-1.031
Contribution of X	-0.278	-0.264	-0.250	-0.272	-0.272	-0.210	-0.224
Valence of X4	-1.206	-1.172	-1.274	-1.276	-1.316	-1.186	-1.255
Contribution of M	-0.902	-0.882	-1.024	-0.982	-1.044	-0.952	-1.031
Contribution of X	-0.304	-0.290	-0.250	-0.292	-0.272	-0.234	-0.224
Mean valence of X	-1.320	-1.292	-1.274	-1.340	-1.316	-1.596	-1.255

^a values were taken from Hillebrecht et al. (2004)

Bond-valences have been calculated with $b = 0.37 \text{ \AA}$ and bond-valence parameters from Brese and O’Keeffe (1991): $R_0(\text{Ti}^{III}\text{-I}) = 2.54 \text{ \AA}$, $R_0(\text{Ru}^{III}\text{-Br}) = 2.26 \text{ \AA}$, $R_0(\text{Ti}^{III}\text{-Ti}^{III}) = 2.52 \text{ \AA}$, $R_0(\text{Ru}^{III}\text{-Ru}^{III}) = 2.42 \text{ \AA}$, $R_0(\text{I-I}) = 2.66 \text{ \AA}$, $R_0(\text{Cl-Cl}) = 1.99 \text{ \AA}$ and $R_0(\text{Br-Br}) = 2.28 \text{ \AA}$. And $R_0(\text{Ru}^{III}\text{-Cl}) = 2.10 \text{ \AA}$ (see text).

contributions to the valence can be interpreted as metal–metal bonding that brings the total valence of the metal atoms closer to the more stable valence of four of these elements (Table 6.7). It is thus found that the metal–metal bonding along the chains is larger in $RuCl_3$ than in $RuBr_3$ and again larger than in TiI_3 , in accordance with the previous suggestion of stronger metal–metal interactions for lighter halogen atoms (Lachgar et al. (1990)). However, the distortion of the TiI_3 structure type towards the $RuBr_3$ structure type has a larger effect on the metal-metal bonding in the iodide than in the bromide and chloride, as it is suggested by the difference between metal atom valences in the high-temperature and low-temperature crystal structures (Table 6.7). The atomic distances in the $RuBr_3$ structure type indicate a stronger or at least equal dimerization in the iodides than in the bromides and chlorides (Table 6.8). This feature can be explained by the more flexible structures formed by the larger iodine atoms than by the smaller bromine and chlorine atoms.

Table 6.8: Metal–metal distances in transition metal trihalides with the $RuBr_3$ type crystal structure. Indicated are the average ($\langle M-M \rangle$), short ($M-M$) and long ($M-M'$) distances (\AA) along the metal chains, as well as the difference (Δd) between the short and long distances.

	$\langle M-M \rangle$	$M-M$	$M-M'$	Δd
TiI_3 (273 K) [*]	3.255	2.978	3.532	0.554
$RuCl_3$ (170 K) Hillebrecht et al. (2004)	2.817	2.633	3.001	0.368
$RuBr_3$ (293 K) Hillebrecht et al. (2004)	2.937	2.765	3.108	0.343
ZrI_3 (RT) Lachgar et al. (1990)	3.340	3.172	3.507	0.335
$MoBr_3$ (RT) Merlino et al. (2004)	3.039	2.874	3.203	0.329

[*] this work.

6.4.2 The phase transition

The structural phase transitions in $RuBr_3$ and $MoBr_3$ have been characterized by temperature-dependent X-ray diffraction (Hillebrecht et al. (2004); Merlino et al. (2004)). Both publications arrive at the conclusion that the phase transitions are of second order, as it is allowed by Landau theory (Franzen (1990)). While Hillebrecht *et al.* (Hillebrecht et al. (2004)) state that "the metal distances change continuously in a temperature range of about 100 K around the transition temperature," Merlino *et al.* (Merlino et al. (2004)) provide a quantitative analysis of the temperature-dependent intensities of selected Bragg reflections. They have determined critical

exponents (β) for the order parameter (η) in the distorted phase,

$$\eta = \left(1 - \frac{T}{T_c}\right)^\beta \quad (6.1)$$

of $\beta \approx 1/8$. This value is only 40% of the value of $\sim 1/3$ that is expected for the critical exponent of the order parameter of a second-order phase transition (Chaikin and Lubensky (2000)), and the second-order nature should be questioned.

Employing $\beta = 1/8$ and $T_c = 323$ K in Eq. 6.1, the value of the order parameter in TiI_3 at $T = 273$ K is 74% of the value at 100 K. The difference in short and long metal distances, which is a measure for the magnitude of the order parameter, is nearly equal at these two temperatures and clearly at variance with a continuous change with temperature (Table 6.6). The other way around, the comparison of distortions at these two temperatures leads to an estimate of 0.008 for the value of the critical exponent in TiI_3 . This indicates that the transition in TiI_3 is more likely to be a first-order than a second-order phase transition.

Consideration of the temperature dependence of the diffracted intensity in MoBr_3 (Fig. 9 in Ref. (Merlino et al. (2004))) shows that a better fit to most of the data would be possible with a value of β considerably smaller than $1/8$. The value $\beta \approx 1/8$ seems to have been determined by one or two data points close to the transition temperature. These data could, however, also be explained as diffuse scattering due to critical fluctuations near the transition, and they should not have been included in the analysis of the critical exponent. We therefore propose that the transition in MoBr_3 is a first-order rather than a second-order phase transition. The data on RuBr_3 (Merlino et al. (2004)) encompass a much smaller range of temperatures than those on MoBr_3 and they seem to be less conclusive.

It is noticed that a first-order phase transition does not preclude the existence of an order parameter. The first-order character requires a discontinuity of the order parameter at T_c , while the order parameter still may continuously increase on further reduction of the temperature. Such a scenario, with different temperature dependencies below T_c , seems to explain the behaviors as observed for TiI_3 , MoBr_3 and RuBr_3 .

6.5 Conclusions

TiI_3 crystallizes in the TiI_3 structure type at high temperatures. At $T_c = 323 \pm 2$ K a structural distortion develops, resulting in the RuBr_3 structure type to be stable

at room temperature. Similar phase transitions have been reported for MoBr_3 , RuBr_3 and RuCl_3 , whereby transition temperatures may be below or above room-temperature (Hillebrecht et al. (2004); Merlino et al. (2004)). These results suggest that other transition metal halides—for which either the TiI_3 or the RuBr_3 structure type has been reported (Table 6.1)—will possess such a transition too.

The high-temperature crystal structure of TiI_3 contains chains of equidistant titanium atoms. Driving force for the phase transition is metal–metal bonding through the formation of dimers along these chains, whereby the order parameter is provided by the difference between the short and long metal-metal distances. A comparison of the crystal structures of TiI_3 close to and far below T_c (Table 6.6), together with the analysis of scant information on this transition in other compounds (Table 6.1), has shown that the phase transition is most probable a first-order phase transition.

Chapter 7

Magnetoelastic coupling in CrOCl

7.1 Introduction

TiOCl has recently attracted attention because of the presence of quasi-one-dimensional (1D) $S = 1/2$ magnetic chains of Ti atoms, which are responsible for the development of a spin-Peierls state below $T_{c1} = 67$ K (Seidel et al. (2003); Shaz et al. (2005)). The low-dimensional character of the magnetic interactions in TiOCl is the result of the presence of the single d electron of Ti^{3+} in the $3d_{x^2-y^2}$ orbital, which then gives rise to a large direct exchange along the chains of metal atoms, but allows only weak magnetic exchange between the chains (Saha-Dasgupta et al. (2004)). Several compounds MOCl (where M is a $3d$ transition metal) are known to be isostructural to TiOCl at room temperature (Schäfer and Wartenpfehl (1961); Ehrlich and Seifert (1959); Haase and Brauer (1975); Lind (1970)). They differ from each other in the number of d electrons on the M^{3+} atom. Different phase diagrams may be expected and have indeed been observed (Christensen et al. (1975); Adam and Buisson (1975); Wiedenmann et al. (1983)). Compounds MOCl are thus of interest, because variation of the element M allows the magnetic interactions to be varied on otherwise equal lattices.

Isostructural compounds MOX ($M = \text{Ti, V, Cr, Fe}$; $X = \text{Cl, Br}$) crystallize in the FeOCl structure type with space group $Pm\bar{m}n$ and lattice parameters $a = 3.8638(2)$, $b = 3.1793(1)$ and $c = 7.7157(3)$ Å for CrOCl at room temperature (Schäfer and Wartenpfehl (1961)). The crystal structures consist of MO double layers sandwiched between layers of halogen atoms which stack along the lattice direction \mathbf{c} (Fig. 7.1). Another view of the structure is that of ribbons MOX perpendicular to \mathbf{a} . Within each ribbon a chain of metal atoms runs along \mathbf{b} .

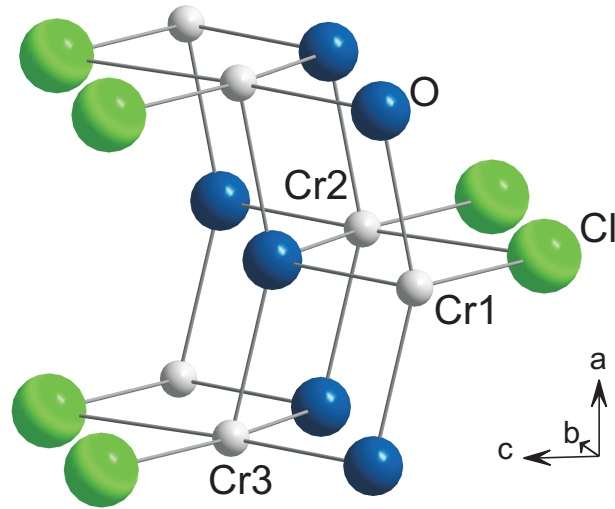


Figure 7.1: Crystal structure of CrOCl .

The short $M-M$ distances ($d = 3.179 \text{ \AA}$) along these chains allow direct exchange interactions between electrons on neighboring atoms (Saha-Dasgupta et al. (2004)). Direct exchange between Ti atoms has been discussed as the reason for the unusual phase diagrams of TiOCl and TiOBr . However, the shortest $M-M$ bond ($d = 3.006 \text{ \AA}$) is between ribbons, *i.e.* between Cr1 and Cr3 in Fig. 7.1. Depending on the symmetry of the filled d orbitals, direct exchange between ribbons as well as superexchange between ribbons and superexchange along \mathbf{a} must be considered.

In TiOCl and TiOBr a spin-Peierls transition has been observed inducing a lowering of the orthorhombic to monoclinic symmetry. The low-temperature spin-Peierls phases in TiOCl and TiOBr have \mathbf{a} -axis unique monoclinic symmetry (Shaz et al. (2005)). In addition both compounds exhibit an intermediate phase between T_{c1} and T_{c2} —with $T_{c2} = 90 \text{ K}$ for TiOCl —which is incommensurately modulated with \mathbf{c} -axis unique monoclinic symmetry (van Smaalen et al. (2005); Krimmel et al. (2006); Schönleber et al. (2006)). Recently it was found that VOCl displays an \mathbf{c} -axis unique monoclinic lattice distortion below $T_N = 80.3 \text{ K}$, which supports antiferromagnetic (AFM) order with a twofold magnetic superstructure (Komarek et al. (2009); Schönleber et al. (2009)). The formation of this phase can be explained by the filling of two $3d$ orbitals by the two d electrons of V^{3+} .

CrOCl was reported to develop AFM order at low temperatures with a fourfold magnetic superstructure (Christensen et al. (1975)). Here we report the temper-

ature dependence of the anisotropic magnetic susceptibility, which indicates that ordered magnetic moments are parallel to \mathbf{c} . X-ray diffraction experiments reveal that the magnetic transition to the AFM state is accompanied by an \mathbf{a} -axis unique monoclinic lattice distortion. The transition to the magnetically ordered state is a first-order transition, and it is accompanied by a structural distortion towards a twofold superstructure. By combining temperature and field dependent magnetisation and specific heat measurements we arrive at a proposal of the (H, T) phase diagram of CrOCl. The differences in phase diagrams of different compounds $MOCl$ are discussed in view of the different numbers of d electrons of the metal atoms.

7.2 Experimental

Single crystals of CrOCl were grown in evacuated quartz-glass ampoules by gas transport according to published procedures (Schäfer and Wartenpfehl (1961); Nocker and Gruehn (1993)). Stoichiometric amounts of Cr_2O_3 (Alpha, 99.997% purity) and CrCl_3 (Alpha, 99.9%) were mixed with HgCl_2 as transport agent and placed in a sealed and evacuated quartz-glass ampoule. The ampoule was heated for five days in a temperature gradient of 1223 K (educt side) to 1123 K (product side). CrOCl formed at the product side of the ampoule as greenish plate-like crystals of up to several millimeter in length. The sample also contained smaller amounts of a dark green powder (Cr_2O_3) on the educt side and CrCl_3 on the product side.

Magnetic susceptibilities at constant field and varying temperature and magnetizations at constant temperature and varying field of a single crystal of 0.45 mg were measured in a Quantum Design MPMS squid magnetometer with the magnetic field oriented either parallel or perpendicular to \mathbf{c} . Heat capacities of the same crystal were determined with the magnetic field oriented parallel to \mathbf{c} in a Quantum Design PPMS system employing the relaxation method.

A crystal of dimensions $0.15 \times 0.05 \times 0.005 \text{ mm}^3$ was selected for x-ray diffraction experiments using synchrotron radiation of wavelength 0.71000 \AA . The crystal was glued to a carbon fiber that was attached to the cold finger of a closed-cycle helium cryostat mounted on the Huber four-circle diffractometer at beamline D3 of HASYLAB at DESY, Hamburg, Germany, equipped with a scintillation detector. Diffraction was measured at selected temperatures between 8 K and room temperature.

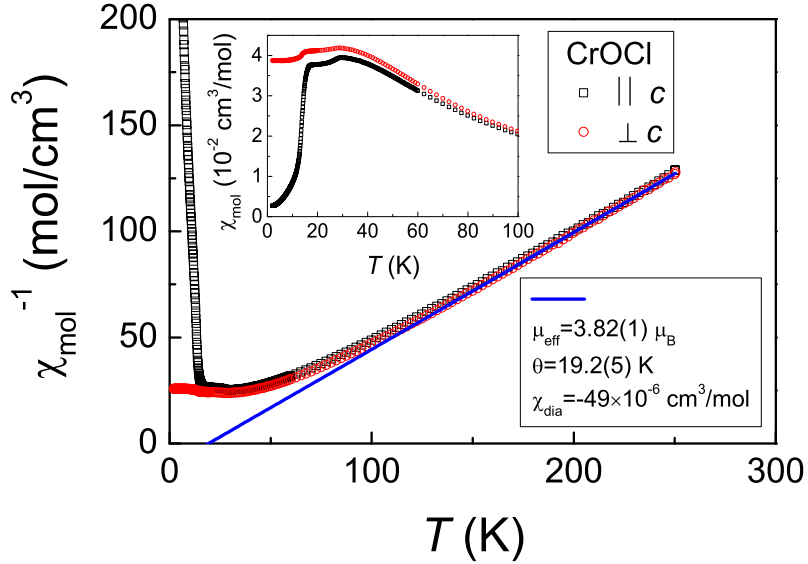


Figure 7.2: (Color online): Magnetic susceptibility of CrOCl measured in a magnetic field of 0.1 T parallel and perpendicular to \mathbf{c} . The (blue) solid line represents a fit of the Curie-Weiss law [eq. (7.1)] to the data at temperatures $T > 175$ K (see text).

7.3 Results

7.3.1 Magnetic Susceptibility and magnetization

Above ~ 175 K the magnetic susceptibilities follow a Curie Weiss law according to (Fig. 7.2)

$$\chi_{mol} = \frac{C}{T - \Theta} + \chi_{dia} \quad (7.1)$$

with a Curie constant $C = 1.825(9) \text{ cm}^3\text{K/mol}$, equivalent to an effective magnetic moment $\mu_{eff} = 3.82(1)\mu_B$, in good agreement with previous measurements (Schäfer and Wartenpfehl (1961)). When fitting eq. (1) to the data, we fixed the diamagnetic contribution to $\chi_{dia} = -49 \times 10^{-6} \text{ cm}^3/\text{mol}$, corresponding to the sum of the diamagnetic increments of the constituting elements in their respective oxidation states according to Selwood: Selwood (1956) Cr^{3+} : $11 \times 10^{-6} \text{ cm}^3/\text{mol}$; O^{2-} : $12 \times 10^{-6} \text{ cm}^3/\text{mol}$; Cl^- : $26 \times 10^{-6} \text{ cm}^3/\text{mol}$. The effective moment is in good agreement with the value expected for a $3d^3$ electronic configuration with spin-only $S = 3/2$

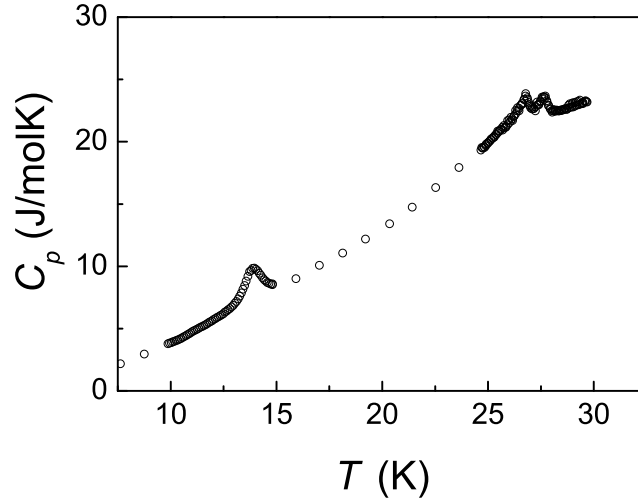


Figure 7.3: Temperature dependence of the specific heat C_p of CrOCl. Anomalies are clearly revealed at 13.9(1) K and at 26.7 and 27.8 K.

state of the Cr^{3+} ion and a g -factor of $g \approx 1.97$ somewhat reduced from the free-electron g -factor due to spin-orbit coupling effects (Abragam and Bleaney (1970)). The Curie-Weiss temperature is positive and amounts to $\Theta = 19.2(5)$ K, indicating predominant ferromagnetic exchange interaction.

Below about 80 K the susceptibilities measured with fields parallel and perpendicular to the \mathbf{c} axis increasingly deviate from each other. A broad maximum appears at ~ 30 K for both directions of the field. Below ~ 14 K χ_{\parallel} drops almost to zero while χ_{\perp} levels off at a value of $3.88 \times 10^{-2} \text{ cm}^3/\text{mol}$ indicating long-range AFM ordering in agreement with previous findings (Christensen et al. (1975)). The splitting of parallel and perpendicular susceptibilities is consistent with the notion of an easy-axis antiferromagnet with the easy axis along or close to the crystallographic \mathbf{c} -axis.

Onset of AFM long-range ordering below ~ 14 K is marked by an anomaly at 13.9(1) K in the specific heat (C_p) measured on the same crystal as used for the determination of the magnetic susceptibilities. An additional, split anomaly of about the same magnitude is observed at 26.7 and 27.8 K (Fig. 7.3).

Magnetization experiments with the magnetic field applied along the easy axis revealed a spin-flop transition at a flop field $H_{SF} = 3.2(1)$ Tesla (Fig. 7.4).

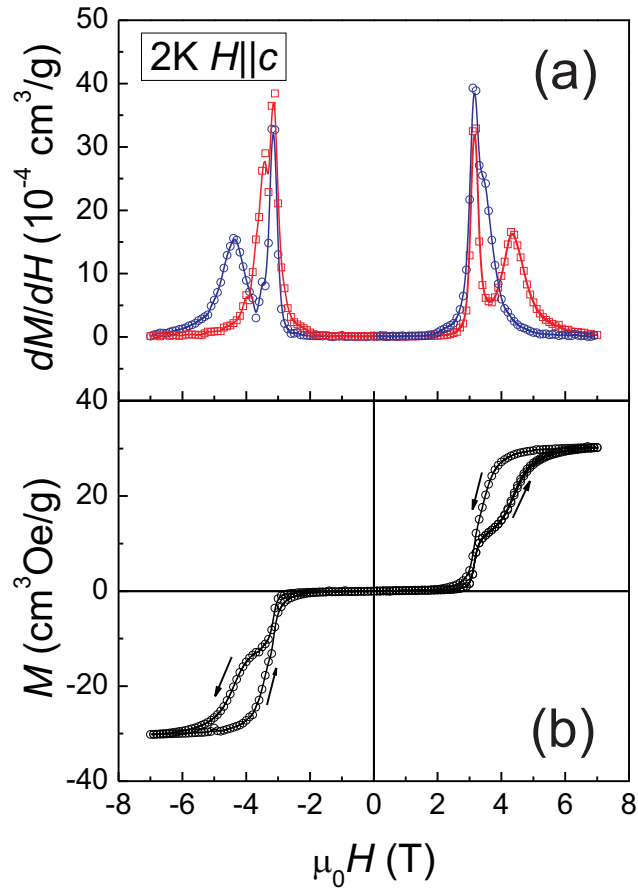


Figure 7.4: (Color online): Magnetization M and its derivative with respect to the magnetic field, dM/dH , measured on CrOCl at $T = 2$ K with the magnetic field applied along the \mathbf{c} axis. The hysteresis in the magnetization branches with data collected by increasing and decreasing field (as indicated by the arrows) is clearly visible and symmetric if the field is reversed. (a) solid (red) lines and symbols \square mark values obtained on increasing the external field, while (blue) solid lines and symbols \circ mark values obtained with decreasing external field.

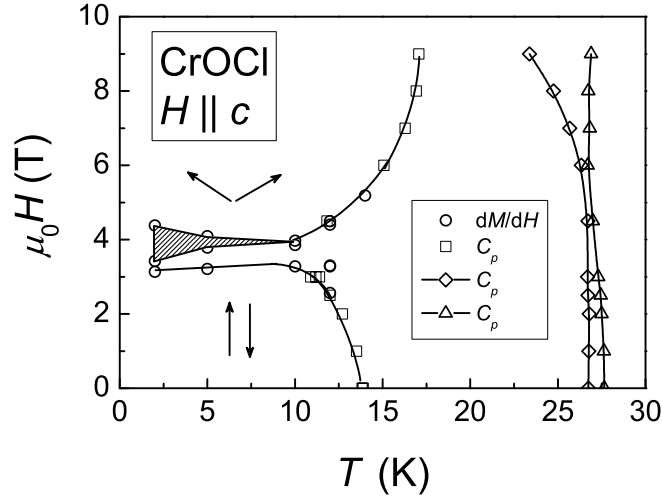


Figure 7.5: Phase diagram of CrOCl with the magnetic field applied along the crystallographic c axis. The arrows indicate the spin flop phase. The shaded area indicates the hysteresis of the spin-flop transition.

A hysteresis is observed between the magnetization measured with increasing and decreasing fields. The derivative dM/dH clearly reveals the splitting of the transition measured with increasing and decreasing fields to be of the order of 1.3 Tesla [Fig. 7.4(a)]. Combining the information obtained from magnetization and specific heat experiments enables us to construct the (H, T) phase diagram for the magnetic phases of CrOCl as shown in Fig. 7.5.

7.3.2 X-ray diffraction

Preliminary x-ray diffraction experiments confirmed the FeOCl structure type of CrOCl. The first series of synchrotron experiments was carried out at selected temperatures in a cooling cycle from 270 K to 9 K. At each temperature so-called ω - 2θ maps were measured for the reflections $(0\bar{2}5)$, (204) and $(2\bar{2}0)$. To this end, detector slits of $6 \times 0.02 \text{ mm}^2$ were set, which correspond to an acceptance angle in the direction of 2θ of 0.0031° . ω -Scans (rotation of the crystal) were carried out for a series of 2θ values, with step sizes of 0.002° in both ω and 2θ . The resulting plot shows the diffracted intensity as a function of the orientation of the crystal and as a

function of the scattering angle. Within the orthorhombic lattice all reflections are expected as single peaks, as is indeed observed down to $T = 15$ K (Fig. 7.6). Some scans show a slight broadening of the peaks in the direction of ω , which indicates a less than optimal crystal quality, most likely resulting from anisotropic stress induced by different thermal contractions of the sample and the glue used to attach the sample.

At $T = 9$ K the reflection $(0\bar{2}5)$ is split in both ω and θ , while the reflection $(2\bar{2}0)$ remains sharp and (204) is split in ω only. These splittings imply a twinned monoclinic crystal with a monoclinic angle α different from 90° . Furthermore, they imply that the monoclinic distortion has occurred through a rotation of the \mathbf{b} -axis while the direction of the \mathbf{c} -axis is the same in both domains.

The experiment was continued by measuring ω - 2θ maps of the $(0\bar{2}5)$ reflection by increasing the temperature in steps of 1 K. The splitting remained visible up to $T = 13.5$ K and disappeared above $T = 15$ K. At 14 K scattering centered at three different 2θ values was observed, which indicates the simultaneous presence of both the monoclinic low-temperature and the orthorhombic high-temperature phases. These observations prove that the transition at T_N is a first-order phase transition. At 13.5 K both maxima appear broadened in the direction of ω , thus suggesting that the transition might already have started. The transition temperature thus is estimated from the x-ray diffraction experiment as $T_N^{xray} = 13.5 \pm 0.5$ K, in good agreement with the magnetization and heat capacity results.

Diffacted intensity as a function of scattering angle was obtained by summing the measured intensities of the ω - 2θ maps in the direction of ω . By this we obtained pseudo-powder-diffraction diagrams, which differ from real powder diffraction by the property that they do not contain diffraction by reflections other than $(0\bar{2}5)$ that might have similar scattering angles. Up to $T = 13.5$ K these plots contain two maxima that can be well fitted with two Lorentzian functions (Fig. 7.7). The difference in the center positions of the two Lorentzians provide an accurate estimate for the splitting in 2θ from which the monoclinic angle α can be calculated (Schönleber et al. (2008)). The monoclinic distortion is weakly temperature dependent and corroborates the first-order character of the phase transition (Fig. 7.8).

At 9 K q -scans were measured along \mathbf{b} for six reflection pairs $(hkl) \rightarrow (hk+1l)$. These indicated the presence of superlattice reflections at half-integer k indices with the two highest intensities at $(0-0.53)$ and $(2-1.51)$. ω -Scans at these positions versus temperature showed the presence of superlattice reflections up to 13 K which disappeared above 15 K (Fig. 7.9).

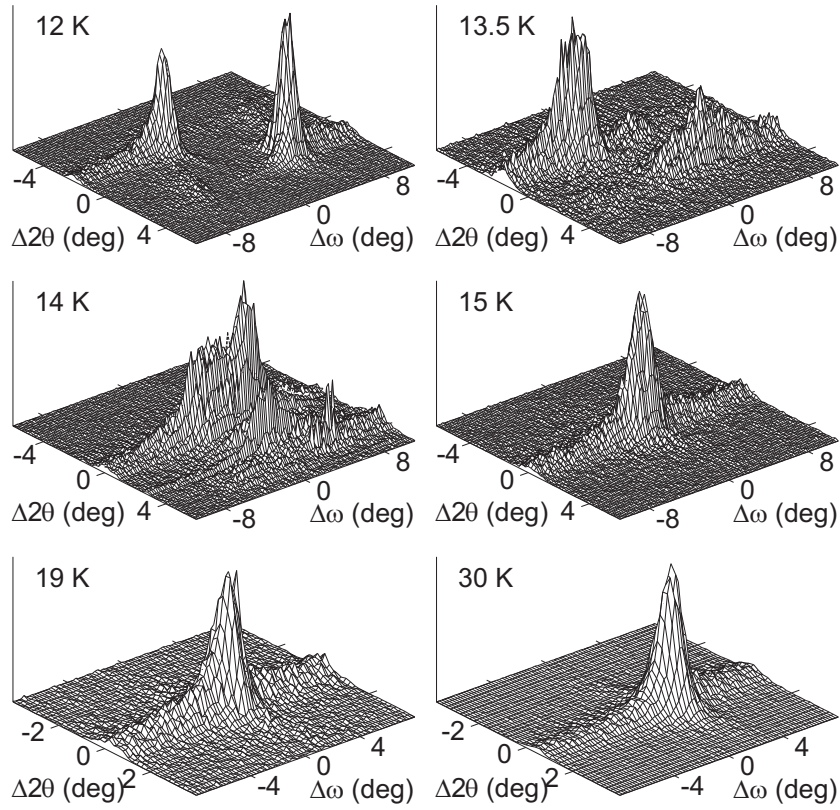
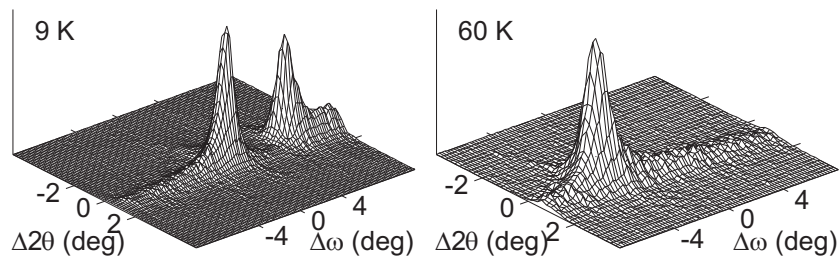
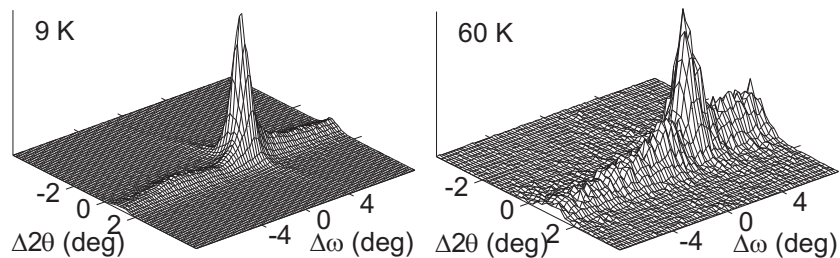
Reflection 0 -2 5**Reflection 2 0 4****Reflection 2 -2 0**

Figure 7.6: Diffracted intensity as a function of the scattering angle 2θ and the crystal orientation ω for several reflections at selected temperatures. $\Delta 2\theta$ and $\Delta \omega$ indicate the deviation from the center of the scan in units of 0.01° .

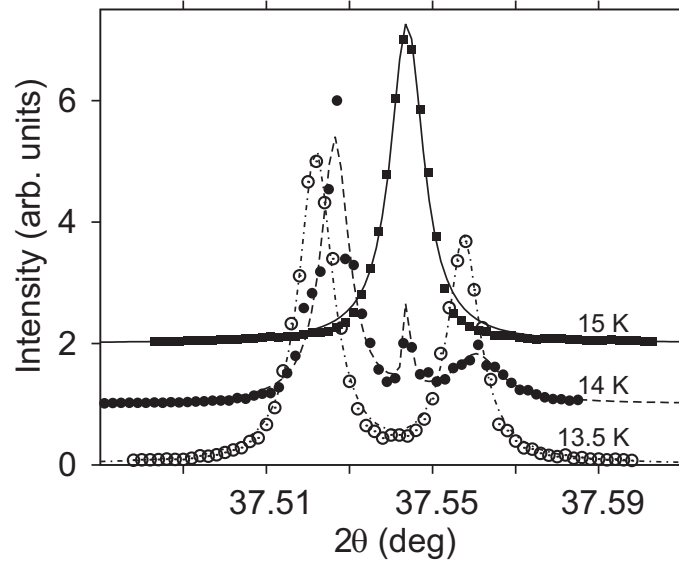


Figure 7.7: Diffracted intensity as a function of the scattering angle 2θ for the reflection $(0\bar{2}5)$ at selected temperatures. Lines represent fits to the data points with one, two or three Lorentz-type functions at each temperature.

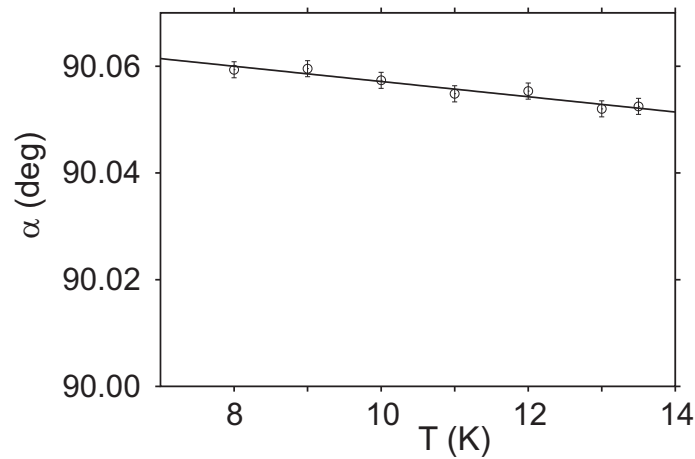


Figure 7.8: Temperature dependence of the monoclinic angle α obtained from the splitting in 2θ of the reflection $(0\bar{2}5)$. The line represents a fit to the data points of $\alpha = \alpha_0 + \alpha_T T$ with $\alpha_0 = 90.071(22)^\circ$ and $\alpha_T = -0.00143(18)^\circ/\text{K}$.

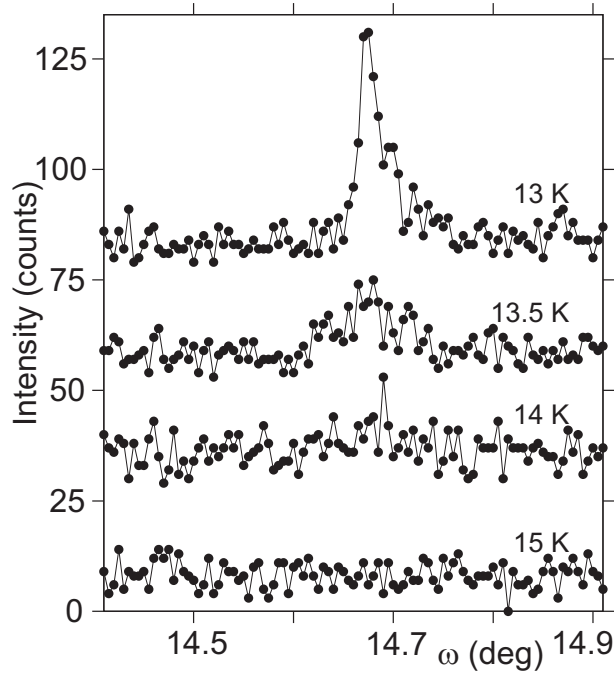


Figure 7.9: ω -Scans centered at the superstructure reflection ($2 -1.5 1$) at selected temperatures. Given is the number of counts measured for 16 s in each step of 0.005° wide. Scans at consecutive temperatures have been given an incremental off-set of 25 counts.

7.4 Discussion

Preceding work has indicated a phase transition to occur in CrOCl at low temperatures towards a state with AFM order on a fourfold magnetic supercell (Christensen et al. (1975)). Here we find that the AFM phase transition is accompanied by a lattice distortion towards monoclinic symmetry and by a structural distortion towards a twofold, $2b$, nuclear superstructure. The transition occurs at $T_N = 13.5$ K, which is significantly lower than the magnetic transition at ~ 80 K in VOCl. The magnitude of the lattice distortion ($\alpha = 90.06^\circ$) is three times smaller than that found in VOCl ($\gamma = 90.2^\circ$) (Komarek et al. (2009); Schönleber et al. (2009)). Both features indicate a sizeable magnetoelastic coupling in CrOCl which is, however, considerably weaker than in VOCl, despite the higher magnetic moment of Cr^{3+} compared to that of V^{3+} . An explanation for the different behaviors of CrOCl ($S = \frac{3}{2}$), VOCl ($S = 1$) and TiOCl ($S = \frac{1}{2}$) can be found in the different symmetries of the filled

$3d$ orbitals in these compounds.

The compounds MOCl ($M = \text{Ti, V, Cr}$) have a common topology and a common symmetry at the metal site. As a working hypothesis we therefore assume an equal hierarchy of $3d$ orbital energies. For TiOCl , calculated electronic band structures have been reported at various levels of theory (Saha-Dasgupta et al. (2004); Fausti et al. (2007); Zhang et al. (2008)). It has been found that the single valence electron of Ti^{3+} occupies the $3d_{x^2-y^2}$ orbital—for x along \mathbf{b} , y along \mathbf{c} and z along \mathbf{a} —that is responsible for AFM coupling by direct exchange between neighboring Ti atoms along \mathbf{b} . The orbitals next higher in energy are $3d_{xz}$ and $3d_{yz}$ (Saha-Dasgupta et al. (2004); Fausti et al. (2007); Zhang et al. (2008)). These orbitals are empty in TiOCl . Here we assume that the two valence electrons of V^{3+} in VOCl occupy the $3d_{x^2-y^2}$ and $3d_{xz}$ orbitals (Schönleber et al. (2009)) and that the three valence electrons of Cr^{3+} in CrOCl occupy the the $3d_{x^2-y^2}$, $3d_{xz}$ and $3d_{yz}$ orbitals. This arrangement explains AFM coupling along \mathbf{b} and strong exchange interactions between neighboring chains of metal atoms through the electrons in the $3d_{xz}$ and $3d_{yz}$ orbitals.

VOCl has been found to develop an \mathbf{c} -axis unique monoclinic lattice distortion (Komarek et al. (2009); Schönleber et al. (2009)). A closer inspection of the crystal structure suggests that this will be the most efficient lattice distortion in order to lift the degeneracy of exchange interactions on the MO bilayers involving the $3d_{xz}$ orbitals of V. This results in stripes of short M - M contacts in the diagonal direction $\frac{1}{2}\mathbf{a} + \frac{1}{2}\mathbf{b}$ and stripes of long M - M contacts in the direction $\frac{1}{2}\mathbf{a} - \frac{1}{2}\mathbf{b}$ (Fig. 7.10). AFM order along $\frac{1}{2}\mathbf{a} + \frac{1}{2}\mathbf{b}$ stripes then combines well with AFM order along \mathbf{b} as imposed by direct exchange via the $3d_{x^2-y^2}$ orbitals. The result is AFM order along \mathbf{a} . The same distortion also lifts the degeneracy of exchange interactions involving $3d_{yz}$ orbitals. However, AFM exchange between these orbitals is probably enhanced along the direction $\frac{1}{2}\mathbf{a} - \frac{1}{2}\mathbf{b}$ of elongated bonds, because σ -type overlap between $3d_{yz}$ orbitals on neighboring atoms is increased in this direction. It thus appears that an \mathbf{c} -axis unique monoclinic distortion leads to frustration between exchange interactions via the $3d_{xz}$ and $3d_{yz}$ orbitals of the metal atom. As both orbitals are occupied in CrOCl , the \mathbf{c} -axis unique monoclinic distortion is unfavorable for this compound.

Experimentally, we have found an \mathbf{a} -axis unique monoclinic lattice distortion for CrOCl , in agreement with the above interpretation. Structurally the easiest way to realize a distortion of this kind requires a relative shift of neighboring layers MOCl . However, this would hardly affect the frustrated exchange interactions within each layer. Instead, we have found that the monoclinic lattice distortion represents a

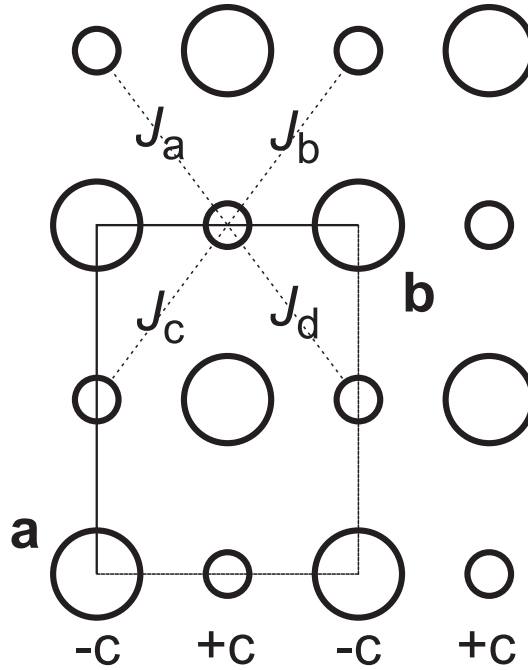


Figure 7.10: Schematic representation of the MO double layers projected onto the a, b -plane. Large circles denote oxygen atoms, small circles represent M atoms. The unit cell of room-temperature structure is indicated. $+c$ and $-c$ denote atoms located at different coordinates along c . A monoclinic distortion with $\gamma \neq 90^\circ$ leads to exchange parameters $J_a = J_d \neq J_b = J_c$; a monoclinic distortion with $\alpha \neq 90^\circ$ leads to $J_a = J_c \neq J_b = J_d$.

shearing of individual layers, which then is responsible for the lifting of the degeneracy of exchange interactions on the MO double layers. Rotation of \mathbf{b} in the (\mathbf{b}, \mathbf{c}) plane results in shorter $M-M$ contacts that form a zigzag pattern on the average parallel to \mathbf{a} . Direct exchange (AFM coupling) is increased along the shorter $M-M$ contacts for both the $3d_{xz}$ and the $3d_{yz}$ orbitals. The result is a ferromagnetic arrangement along \mathbf{a} , which might explain the predominant FM exchange as derived from Curie-Weiss temperature. This order can be combined by AFM coupling between neighboring M atoms along \mathbf{b} . The role of the structural distortion (doubling of the \mathbf{b} -axis) could be to increase the exchange interactions between the zigzag stripes, however a more detailed description requires a complete structure model of the low-temperature phase.

The specific heat data indicate additional transitions at a temperature of ~ 27.2 K (Fig. 7.3). A signature of this magnetic transition has not been found in our

x-ray diffraction data, while a weak anomaly is present in $\chi_M(T)$ (Fig. 7.2). This suggests a purely magnetic character of this transition, for example the formation of incommensurate magnetic order.

While an **c**-axis monoclinic distortion appears to provide a maximum effect on lifting the degeneracy of the coupling between $3d_{xz}$ orbitals of metal atoms on neighboring ribbons, it does not do so for the $3d_{yz}$ orbitals. Instead, an **a**-axis monoclinic distortion through a change of direction of the **b**-axis—*i.e.* representing a distortion of the layers rather than a relative shift between layers—accompanied by a structural distortion representing a doubling of the **b**-axis leads to the required lifting of degeneracy of exchange interactions through the $3d_{yz}$ orbitals. The different lattice distortions of VOCl and CrOCl are thus explained by the different symmetries of the filled $3d$ orbitals.

7.5 Conclusions

The phase transition of CrOCl towards a state of AFM order has been identified as a first-order phase transition at $T_N = 13.5$ K, which is accompanied by a lattice and a structural distortion towards a twofold, $2\mathbf{b}$ superstructure with **a**-axis unique monoclinic symmetry. The ordered magnetic moment is parallel to **c**. A second transition is discovered that is presumably of purely magnetic origin and might indicate the formation of an incommensurate magnetic superstructure.

The different behaviors of TiOCl, VOCl and CrOCl result from different symmetries of the occupied $3d$ orbitals, which lead to different exchange interactions on the *MO* double layers of these isostructural series of compounds.

Chapter 8

Inhomogeneous thermal expansion of layered CrOCl

8.1 Introduction

Thermal expansion provides valuable information about solids, including anharmonicity, anisotropy and the nature of phase transitions (Barron (1998)). The fundamental mechanisms determining thermal expansion are well understood, but an *ab initio* calculation of thermal expansion is not possible except for materials with very simple structures. Primarily, thermal expansion is determined by the anharmonic character of the interatomic potential. However, rearrangements of the atoms within the unit cell may be important too. This internal expansion or inhomogeneous expansion can be the cause of negative expansion and the invar effect (Barrera et al. (2005)).

Thermal expansion of crystalline compounds can accurately be measured by interferometry, dilatometry and X-ray diffraction (Ho and Taylor (1998)). Only X-ray diffraction offers the possibility to determine the internal expansion, then requiring complete structure determinations at several temperatures. Especially the temperature-dependent structural rearrangements provide clues for the understanding of physical properties and for the mechanisms of phase transitions. Examples of such approaches can be found in Refs. Dabrowski et al. (1999); Maniwa et al. (2001); Redhammer et al. (2007). The accuracy of the relative atomic coordinates is much lower than the accuracy with which the lattice parameters can be determined.

Layered materials usually exhibit linear thermal expansions of magnitudes much larger into the direction perpendicular to the layers than into directions parallel to

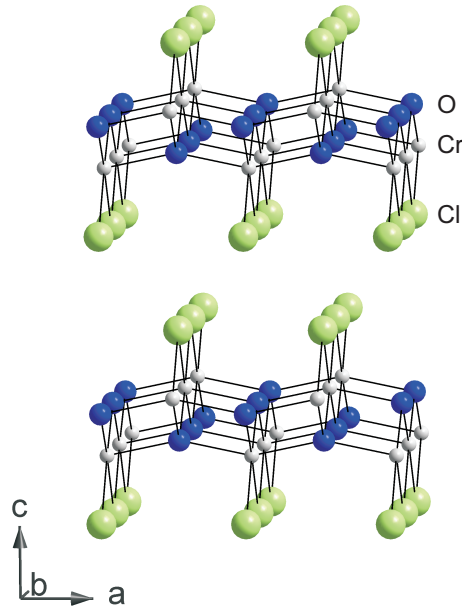


Figure 8.1: Section of the crystal structure of CrOCl .

the layers (Givens and Fredericks (1977); Murray and Evans (1979)). This property is attributed to the strong chemical bonds between atoms within one layer, while neighboring layers interact via much weaker Van-der-Waals-type interactions. With the exception of graphite, this property has not been quantified.

CrOCl is a layered compound that crystallizes in the FeOCl structure type with space group $Pm\bar{m}n$ and lattice parameters $a = 3.8635(2)$, $b = 3.1787(1)$ and $c = 7.7046(3)$ Å at $T = 250$ K (Schäfer and Wartenpfehl (1961)). CrOCl and other, isostructural compounds MOCl ($M = \text{Ti, V, Cr, Fe}$) have been studied for their magnetic behavior at low temperatures (Christensen et al. (1975); Adam and Buisson (1975); Wiedenmann et al. (1983); Seidel et al. (2003)). CrOCl develops a fourfold magnetic superstructure below $T_N = 13.5$ K, but it does not exhibit other phase transitions (Christensen et al. (1975); Angelkort et al. (2009)). MOCl are layered materials comprising of bi-atomic layers MO sandwiched between chlorine atoms. The layers are defined through a network of strong chemical bonds M-O and M-Cl , and they are stacked perpendicular to the \mathbf{c} axis, separated by Van der Waals gaps (Fig. 8.1). Each layer is bounded by chlorine atoms on both sides. Because of the symmetry of the crystal structure, the chlorine atoms are in single planes at $z \approx \pm 0.327$, and they thus uniquely define the boundary between the layers and

the Van-der-Waals-gap region. Furthermore, by virtue of the orthorhombic symmetry principal axes of thermal expansion are along the lattice directions **a**, **b** and **c**. Compounds $MOCl$ are thus ideally suited to disentangle the thermal expansion into variations of the thickness of the layers and the width of the Van-der-Waals gap, by studying the thermal variation of both **c** and the coordinate z of the chlorine atoms.

Here we report the average thermal expansion of $CrOCl$ as obtained from its crystal structures at four temperatures in the range 100–340 K. The thermal expansion of the layers is found to be nearly isotropic, despite the fact that the layers are free to expand into the Van der Waals gaps, while in the directions parallel to the layers an infinite network of strong chemical bonds exists. The high anisotropy of the thermal expansion is due to the expansion of the Van-der-Waals gap on increasing temperature.

8.2 Experimental

Single crystals of $CrOCl$ were grown in evacuated quartz-glass ampoules by gas transport according to published procedures (Schäfer and Wartenpfehl (1961); Angelkort et al. (2009)). One crystal of approximate dimensions of $0.2 \times 0.2 \times 0.01 \text{ mm}^3$ was selected for single-crystal X-ray diffraction experiments. It was mounted on a boron glass fiber by aid of a two-component glue. X-ray diffraction was measured on a MAR345 image plate diffractometer equipped with a rotating anode X-ray generator (50 kV, 100 mA) and a graphite monochromator selecting $Mo-K_\alpha$ radiation. The crystal temperature was regulated with an Oxford Cryostream nitrogen-gas-flow cryostat. Diffraction was measured at temperatures of 100, 250, 310 and 340 K, employing the rotating-crystal method with 0.5° of rotation per frame. Detector positions were chosen with zero and 15° off-sets.

Lattice parameters and integrated intensities of Bragg reflections were determined from the measured diffraction images by the software EVAL14 (Duisenberg et al. (2003)). Absorption correction was performed with SADABS (Sheldrick (1998)). The integrated data were used for refinements of the crystal structures, employing the computer program JANA2006 (Petricek et al. (2006)). Starting values of the parameters were taken from Christensen *et al.* (Christensen et al. (1975)). The structure model involved the atomic coordinates and anisotropic temperature parameters of all three crystallographically independent atoms (one atom each of Cr, O and Cl) (Table 8.1).

Table 8.1: Experimental details and structural data of CrOCl at four temperatures. Cr is at special position (0, 0.5, z); O and Cl are at (0, 0, z).

Temperature (K)	100	250	310	340
Formula weight (g/mol)			103.45	
a (Å)	3.8614 (2)	3.8635 (2)	3.8635 (2)	3.8642 (2)
b (Å)	3.1768 (1)	3.1787 (1)	3.1793 (1)	3.1796 (1)
c (Å)	7.6840 (3)	7.7065 (3)	7.7151 (3)	7.7207 (3)
Volume (Å ³)	94.2588	94.6443	94.7663	94.8612
Z			2	
Data collection				
Absorption coefficient (mm ⁻¹)	6.982	6.954	6.944	6.938
θ_{\max} (°)	32.2	37.2	32.2	37.2
No. reflections (observed)	1931	5409	3037	2531
No. unique reflections	277	371	296	352
R_{int}	0.0336	0.0303	0.0328	0.0315
Structure refinement				
wR_F^2 (obs.)	0.0369	0.0380	0.0358	0.0415
R_F (observed)	0.0237	0.0225	0.0198	0.0263
GoF (observed)	2.64	2.89	2.59	2.63
$\Delta\rho_{max}$ (e/Å ³)	0.57	0.71	0.44	0.55
$\Delta\rho_{min}$ (e/Å ³)	-0.63	-0.84	-0.55	-0.76
z [Cr]	0.108269(55)	0.107956(44)	0.107852(50)	0.107799(44)
U_{iso} [Cr]	0.00341(16)	0.00458(14)	0.00513(16)	0.00660(17)
z [O]	0.94464(23)	0.94479(22)	0.94453(25)	0.94502(23)
U_{iso} [O]	0.00364(54)	0.00494(41)	0.00544(48)	0.00736(45)
z [Cl]	0.327531(84)	0.326780(74)	0.326543(87)	0.326300(78)
U_{iso} [Cl]	0.00594(20)	0.01012(18)	0.01221(21)	0.01417(22)

8.3 Discussion

The relative changes of the lattice parameters on heating above $T = 100$ K provide values for the average linear expansion coefficients, which are defined by

$$\beta_l = \frac{l(T) - l(100)}{l(100)(T - 100 \text{ K})} \quad (8.1)$$

where $l(T)$ is the length at temperature T in the direction of the expansion. For the three lattice directions, the average linear expansions over the temperature range 100–250 K thus are found as (Table 8.1)

$$\beta_a = 0.311 \cdot 10^{-5}; \beta_b = 0.384 \cdot 10^{-5}; \beta_c = 1.956 \cdot 10^{-5} \text{ K}^{-1}$$

Because of the orthorhombic symmetry this are the principal components and they completely define the thermal expansion tensor. In accordance with the expectations these values indicate a highly anisotropic expansion with the largest value in the direction perpendicular to the layers.

The thickness of a single layer CrOCl is defined by $d_L = 2z[\text{Cl}]c$, while the width of the Van der Waals gap then is $d_{\text{vdW}} = (1 - 2z[\text{Cl}])c = c - d_L$. Taking into account the temperature dependencies of both c and the coordinate $z[\text{Cl}]$, different average linear expansions of the layers and the Van der Waals gaps are obtained as (Eq. 8.1; Table 8.1)

$$\beta_L = 0.222 \cdot 10^{-5}; \beta_{\text{vdW}} = 2.646 \cdot 10^{-5} \text{ K}^{-1}$$

It is thus found that nearly all expansion in the direction perpendicular to the layers is due to an expansion of the Van der Waals gap (Fig. 8.2). The linear expansion coefficient of the layers in this direction is even smaller than in the lateral directions, despite the fact that the layers are almost "free" to expand into the Van der Waals gap. It appears that the expansion of single layers is determined by the strong chemical bonds within the layers rather than the "free" space around them.

Several of the transition metal dichalcogenides exhibit phase transitions in a wide range of temperatures, that are responsible for anomalies in the thermal expansion. Corrected for these anomalies, they might show a similar nearly isotropic expansion of single layers as presently found for CrOCl (Givens and Fredericks (1977); Murray and Evans (1979)). Graphite is a special layered compound, since its layers of one plane of carbon atoms have thickness zero in the present definition. Accordingly, the linear expansion of the layers in the stacking direction is zero and the expansion of the Van der Waals gap is equal to the linear expansion along \mathbf{c} , with average value

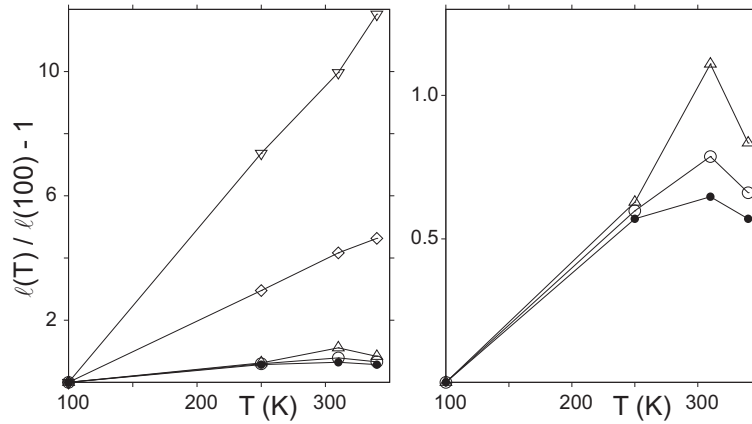


Figure 8.2: Temperature dependence of the relative variations of the lattice parameters, the thickness of the layers and the width of the Van der Waals gap (Eq. 8.1 and Table 8.1).

over 100–250 K of $\beta_c = \beta_{\text{VdW}} = 2.2 \cdot 10^{-5} \text{ K}^{-1}$ Bailey and Yates (1970). The linear expansion parallel to the layers is negative with average value $\beta_a = -1.2 \cdot 10^{-5} \text{ K}^{-1}$ (Bailey and Yates (1970)).

Within the present approach we cannot provide a model for the expansion of graphite. However, it is noticed that the transition metal dichalcogenides and MOCl are unique in the sense that they comprise of layers interacting via Van der Waals forces, while many other so-called 'layered compounds'—including graphite—involve covalent or ionic contributions to the bonding between layers.

Chapter 9

Summary

In this thesis results of the investigations of the mechanisms of solid-solid phase transitions are reported on basis of the exemplary characterization of the phase transition of the metalorganic compound $\text{Eu}(\text{SC}_{36}\text{H}_{49})_2$ and of the inorganic transition-metal compounds TiI_3 and CrOCl .

The phase transitions were surveyed temperature dependently by the performance of single-crystal X-ray diffraction experiments and measurements of the magnetic susceptibility. The X-ray diffraction experiments were carried out as data collections of integrated intensities of reflections and as measurements of profiles on selected reflections in so-called ω - 2θ maps. The data sets of the integrated intensities were used to determine the crystal structures at different temperatures. By the comparison of the high- and the low-temperature crystal structures the mechanisms of the phase transitions of the compounds $\text{Eu}(\text{SC}_{36}\text{H}_{49})_2$ and TiI_3 were determined. Furthermore the transition temperatures of all three compounds were determined by temperature-dependent measurements of intensities of superstructure reflections. From the ω - 2θ maps the monoclinic lattice distortion of the low-temperature phase of CrOCl was calculated.

For the metalorganic compound $\text{Eu}(\text{SC}_{36}\text{H}_{49})_2$ a phase transition with a transition temperature of $T_c = 119$ K was found and the high- as well as the low-temperature structures were determined. The transition into the low-temperature phase was attributed to the ordering of isopropyl-groups which are disordered in the high-temperature structure. The asymmetric unit of the high-temperature phase is composed of one molecule $\text{Eu}(\text{SC}_{36}\text{H}_{49})_2$ in which the isopropyl-groups are disordered with almost equal occupancy probabilities over two positions. In the low-temperature structure two symmetry independent molecules with different confor-

mations are forming the asymmetric unit. The complementary atomic positions of the disordered atoms in the high-temperature phase are distributed in the low-temperature phase in such a way that each molecule possesses one of the two possible atomic positions. Thus, the low-temperature structure contains only ordered and completely occupied atomic positions. The transition into the low-temperature structure is accompanied by a loss of symmetry by which the number of symmetrically independent molecules is increased to two. The more compact conformation of one of the two molecules causes a decrease of the average volume per molecule by the transition into the low-temperature phase. The formation of a denser packing of atoms is the driving force of the phase transition.

For TiI_3 a phase transition with a transition temperature of $T_c = 323$ K was discovered and the crystal structures of the high- and low-temperature phases close to the transition temperature as well as the low-temperature structure at a temperature of 100 K were determined. In the high- and low-temperature structures of TiI_3 face-sharing of TiI_6 octahedra along the lattice direction \mathbf{c} results in the formation of chains of titanium atoms running along \mathbf{c} . In the high-temperature structures the titanium atoms are equally spaced along the chain axes. The symmetry of the high-temperature structure was found to be $P6_3/mcm$, and the symmetry of the low-temperature structure was determined as $Pmnm$. The transition into the low-temperature phase was associated with the formation of crystal domains which were twinned by a threefold rotation axis oriented parallel to \mathbf{c} . For temperatures below T_c an atomic displacement of the titanium atoms along the chains was observed indicating a grouping of titanium atoms to dimers. The dimerization of the titanium atoms promotes the phase transition. Also for other isostructural transition-metal compounds phase transitions caused by a dimerization of metal atoms are known (H. Hillebrecht, T. Ludwig and G. Thiele (2004), *Z. Anorg. Allg. Chem.* **630**: 2199-2204) and probably all the transition-metal trihalide compounds form low-temperature phases in which the metal atoms are dimerized.

The dimerization of titanium atoms in the low-temperature structure of TiI_3 can be used to calculate the order parameter of the phase transition as a function of the temperature. An abrupt change of the order parameter at temperatures close below the phase transition temperature exhibits the first order character of the phase transition.

From the low-temperature structures of the transition-metal trihalides the one of TiI_3 possesses the largest difference of the atomic distances between neighboring metal atoms on the metal chains. Although the metal-metal interactions are stronger

for the chlorides and bromides a higher flexibility in the structures cause iodides to possess higher values of dimerisation.

CrOCl crystalizes in a layer-type crystal structure possessing the symmetry $Pmmn$. The layers of CrOCl are stacked along the lattice direction \mathbf{c} and neighboring layers of CrOCl are separated by van-der-Waals gaps. Measurements of the magnetic susceptibility revealed that CrOCl undergoes a phase transition from a paramagnetic room-temperature phase into an antiferromagnetic low-temperature phase at $T_N = 13.5$ K.

The profiles on selected reflections of the reciprocal lattice planes $0kl$, $h0l$ and $hk0$ were measured in ω - 2θ maps for the temperature range 8 – 270 K. A splitting of reflections along certain directions indicated the occurrence of twin-domains resulting from a lowering of the symmetry at the transition to monoclinic. The splitting of reflections was observed for temperatures below the transition temperature $T_c = 13.5$ K but could not be found at higher temperatures. The coincidence of the transition temperatures of the structural and the magnetic phase transition gives evidence for the direct structural implication of the magnetic phase transition.

Through the direction dependent splitting of the reflections of the three reciprocal lattice planes the monoclinic angle was identified as angle α and the twinning-plane of the crystal was found to occur perpendicular to \mathbf{c} .

The magnitude of the splitting of the reflections was determined for different temperatures below T_c and was used to calculate the value of α . It was found, that the angle α changes at the transition into the low-temperature phase discontinuously to a value of ~ 90.05 deg. The sudden increase exhibits that the phase transition is a first order phase transition.

Measured non-zero intensities of superstructure reflections with k indices of 0.5 and 1.5 evidence that the low-temperature structure constitutes a $2\mathbf{b}$ superstructure of the high-temperature structure. At the transition into the low-temperature phase the orientation of the \vec{b} -axis was found to change by a rotation within the (\mathbf{b}, \mathbf{c}) plane causing a shearing of the individual layers of CrOCl.

The crystal structure of CrOCl was determined for four different crystal temperatures in the temperature range between 100 and 340 K. An increase of the crystal temperature effects an anisotropic expansion of the lattice directions \mathbf{a} , \mathbf{b} and \mathbf{c} . Along the lattice direction \mathbf{c} the highest thermal expansion was found. It is caused by the temperature-dependent expansion of the van-der-Waals gaps. The linear thermal expansion along \mathbf{c} was determined to be approximately five times larger as the linear thermal expansion along \mathbf{a} or \mathbf{b} .

All the investigated phase transitions were found to be first order phase transitions. The discontinuous structural change of TiI_3 at the transition into the low-temperature phase opposes the gradual change of the magnetic susceptibility in the vicinity of the transition temperature (W. Klemm and E. Krose (1947), *Z. Anorg. Allg. Chem.* **253**: 209-217). The mechanism of the structural phase transition corresponds to the pairing of metal atoms as it is found for the spin-Peierls phase transitions of the transition-metal oxyhalides.

It was shown that the room-temperature phase of CrOCl transforms analogous to other transition-metal oxyhalides in an antiferromagnetic phase transition into a monoclinic low-temperature phase.

The different electron configurations of the metal atoms in TiOCl , VOCl and CrOCl result in a different transition behavior of these compounds and in the formation of different magnetic low-temperature structures. TiOCl undergoes two phase transitions and forms an intermediate phase whose structure is incommensurately modulated. VOCl and CrOCl exhibit only one phase transition. In contrast to VOCl which transforms at $T_c = 80.3$ K into a monoclinic phase with γ as the monoclinic angle, the interactions of the metal atoms in the low-temperature phase of CrOCl cause the angle α to be the monoclinic angle.

Chapter 10

Zusammenfassung

Thema der vorliegenden Dissertation ist die Untersuchung von Mechanismen von fest-fest Phasenübergängen, welche anhand des Phasenübergangs der Organometallverbindung $\text{Eu}(\text{SC}_{36}\text{H}_{49})_2$ und der anorganischen Übergangsmetallverbindungen TiI_3 und CrOCl dargelegt werden.

Die Phasenübergänge wurden in Abhängigkeit von der Temperatur mittels Einkristallröntgenbeugung sowie Messungen der magnetischen Suszeptibilität untersucht. Bei den Röntgenbeugungsexperimenten handelte es sich um Messungen von integrierten Reflexintensitäten und Messungen von Reflexprofilen in so genannten ω - 2θ -Maps. Die Datensätze der integrierten Reflexintensitäten wurden dazu verwendet, Kristallstrukturen bei unterschiedlichen Kristalltemperaturen zu bestimmen. Durch das Vergleichen der Hoch- und Tieftemperaturstrukturen wurden die Mechanismen der Phasenübergänge der Verbindungen $\text{Eu}(\text{SC}_{36}\text{H}_{49})_2$ und TiI_3 bestimmt. Darüberhinaus wurden durch temperaturabhängige Intensitätsmessungen an Überstrukturreflexen die Übergangstemperaturen der fest-fest-Übergänge aller drei untersuchten Verbindungen ermittelt. Aus den ω - 2θ -Maps wurde die monokline Verzerrung des Gitters in der Tieftemperaturphase von CrOCl bestimmt.

Für die Organometallverbindung $\text{Eu}(\text{SC}_{36}\text{H}_{49})_2$ wurde ein Phasenübergang mit einer Umwandlungstemperatur von $T_c = 119$ K gefunden. Die Hoch- sowie die Tieftemperaturstruktur wurden bestimmt. Die Phasenumwandlung in die Tieftemperaturphase wurde auf das Ordnen von in der Hochtemperaturstruktur fehlgeordnet vorliegenden Isopropyl-Gruppen zurückgeführt. Die asymmetrische Einheit der Hochtemperaturphase besteht aus einem Molekül $\text{Eu}(\text{SC}_{36}\text{H}_{49})_2$, in welchem die Isopropyl-Gruppen über zwei Positionen mit etwa gleicher Besetzungswahrscheinlichkeit fehlgeordnet auftreten. In der Tieftemperaturstruktur bilden zwei symme-

trieunabhängige Moleküle mit unterschiedlichen Molekülkonformationen die asymmetrische Einheit. Die komplementären Atompositionen der fehlgeordneten Atome in der Hochtemperaturphase werden beim Übergang in die Tieftemperaturstruktur auf die beiden Moleküle so verteilt, dass auf jedes Molekül je eine der beiden möglichen Atompositionen entfällt. In der Tieftemperaturstruktur liegen somit geordnete, voll besetzte Atompositionen vor. Die Umwandlung in die Tieftemperaturstruktur wird von einem Verlust an Symmetry begleitet wodurch die Anzahl der symmetrieunabhängigen Moleküle auf zwei erhöht wird. Die kompaktere Konformation eines der symmetrieunabhängigen Moleküle bewirkt eine Verringerung des mittleren Molekülvolumens beim Übergang in die Tieftemperaturphase. Die beim Übergang auftretende Bildung einer dichteren Packung der Atome ist die treibende Kraft der Phasenumwandlung.

Für TiI_3 wurde eine Phasenumwandlung mit einer Phasenübergangstemperatur von $T_c = 323$ K entdeckt und die Kristallstrukturen der Hoch- und der Tieftemperaturphase nahe der Umwandlungstemperatur und die Tieftemperaturstruktur bei einer Temperatur von 100 K bestimmt. In der Hoch- und Tieftemperaturstruktur von TiI_3 liegen TiI_6 -Oktaeder vor, welche entlang der Gitterrichtung c flächenverknüpft sind und zur Bildung von längs c verlaufenden Titanatom-Ketten führen. In der Hochtemperaturstruktur sind die Titanatome equidistant entlang der Kettenachsen verteilt. Die Symmetrie der Hochtemperaturstruktur erwies sich als $P6_3/mcm$, und die Symmetrie der Tieftemperaturstruktur wurde als $Pmnm$ bestimmt. Die Umwandlung in die Tieftemperaturphase vollzog sich unter gleichzeitiger Ausbildung von Kristalldomänen, welche über eine parallel zu c orientierte dreizählige Rotationsachse verzwillingt waren. Für Temperaturen unterhalb von T_c wurde eine Verschiebung der Titanatome längs der Kettenachsen beobachtet, aufgrund welcher sich Metallatom-Dimere bildeten. Die Paarbildung der Titanatome verursacht das Auftreten der Phasenumwandlung. Für isostrukturelle Übergangsmetallverbindungen anderer Zusammensetzung sind ebenfalls Phasenübergänge infolge der Bildung von Metall-Dimeren bekannt (H. Hillebrecht, T. Ludwig und G. Thiele (2004), *Z. Anorg. Allg. Chem.* **630**: 2199-2204) und es ist wahrscheinlich, dass alle Trihalogenid-Verbindungen eine Tieftemperaturphase besitzen, in welcher die Metallatome Dimere bilden.

Die mit abnehmender Temperatur fortschreitende Dimerisierung der Ti-Ti-Abstände in der Tieftemperaturstruktur von TiI_3 wurde benutzt, um den Ordnungsparameter des Phasenübergangs zu berechnen. Seine plötzliche Änderung nahe der Umwandlungstemperatur weist auf das Vorliegen eines Phasenübergangs erster Ord-

nung hin.

Von den Tieftemperaturstrukturen der Trihalogenide weist jene von TiI_3 die größten Längenunterschiede der Atomabstände benachbarter Metallatome in den Metallatomketten auf. Obwohl die Wechselwirkungen der Metallatome in Chloriden und Bromiden größer sind besitzen die Jodide aufgrund einer größeren Flexibilität ihrer Struktur größere Beträge der Dimerisierung.

CrOCl kristallisiert in einer Schichtstruktur, welche die Symmetrie $Pm\bar{m}n$ besitzt und in welcher CrOCl -Lagen längs der Gitterrichtung \mathbf{c} gestapelt sind. Zwischen den aufeinander folgenden CrOCl -Lagen bestehen van-der-Waals-Lücken. Mittels Messungen der magnetischen Suszeptibilität konnte gezeigt werden, dass CrOCl bei $T_N = 13.5$ K eine Umwandlung der paramagnetischen Raumtemperaturphase in eine antiferromagnetische Tieftemperaturphase vollzieht.

Die Reflexprofile von ausgesuchten Reflexen der reziproken Gitterebenen $0kl$, $h0l$ und $hk0$ wurden als ω - 2θ -Maps in einem Temperaturbereich von 8 - 270 K gemessen. Reflexaufspaltungen entlang bestimmter Richtungen zeigen das Auftreten von Zwillingsdomänen an, welche als Folge einer Symmetrierniedrigung beim Übergang in die monokline Tieftemperaturphase gebildet wurden. Die durch die Reflexaufspaltungen angezeigte monokline Verzerrungen des Kristallgitters setzte unterhalb der Übergangstemperatur $T_c = 13.5$ K ein. Das Zusammenfallen der strukturellen und magnetischen Umwandlungstemperaturen belegt das Auftreten einer unmittelbaren strukturellen Änderung als Folge des magnetischen Phasenübergangs.

Durch die richtungsabhängige Aufspaltung der Reflexe der drei reziproken Gitterebenen konnte der monokline Winkel als Winkel α identifiziert werden. Für die Zwillingsebene wurde eine Orientierung senkrecht zur \mathbf{c} -Richtung gefunden.

Aus dem Betrag der Reflexaufspaltungen wurde der Winkel α für verschiedene Temperaturen unterhalb T_c bestimmt. Sein Wert ändert sich beim Übergang in die Tieftemperaturphase diskontinuierlich auf einen Wert von $\approx 90.05^\circ$ und kennzeichnet mit seinem sprunghaften Anstieg das Vorliegen eines Phasenübergangs erster Ordnung.

Gemessene Überstrukturreflexe mit den k-Indizes 0.5 und 1.5 weisen darauf hin, dass die Tieftemperaturstruktur eine $2\mathbf{b}$ -Überstruktur der Hochtemperaturstruktur darstellt. Beim Phasenübergang in die Tieftemperaturstruktur wurde ein Verdrehen der \vec{b} -Achse in der (\mathbf{b}, \mathbf{c}) -Ebene beobachtet, welches eine Scherung der einzelnen CrOCl -Lagen verursacht.

Die Kristallstruktur von CrOCl wurde für vier verschiedene Kristalltemperaturen in einem Temperaturbereich von 100 bis 340 K bestimmt. Mit einer Erhöhung

der Kristalltemperatur erfolgte eine anisotrope Ausdehnung entlang den Gitterrichtungen **a**, **b** und **c**. Entlang der Gitterrichtung **c** wurde die größte thermische Ausdehnung gefunden. Sie wird durch das temperaturabhängige Weiten der van-der-Waals-Lücken verursacht. Für den linearen thermischen Ausdehnungskoeffizient entlang **c** wurde ein etwa fünfmal größer Wert als entlang **a** und **b** ermittelt.

Die untersuchten Phasenumwandlungen erwiesen sich als Phasenübergänge erster Ordnung. Die sprunghafte Strukturänderung von TiI_3 steht im Gegensatz zu der allmählichen Änderung der magnetischen Suszeptibilität in der Nähe der Umwandlungstemperatur (W. Klemm und E. Krose (1947), *Z. Anorg. Allg. Chem.* **253**: 209-217). Der für TiI_3 gefundene Mechanismus des strukturellen Übergangs entspricht der Paarbildung von Metallatomen wie sie bei den Spin-Peierls Phasenübergängen der Übergangsmetalloxyhalogenid-Verbindungen auftreten.

Es wurde gezeigt, dass CrOCl wie andere Übergangsmetalloxyhalogenid-Verbindungen einen antiferromagnetischen Phasenübergang zu einer monoklinen Tieftemperaturphase durchläuft. Aufgrund unterschiedlicher Elektronenkonfigurationen der Metallatome werden unterschiedliches Übergangsverhalten und unterschiedliche magnetische Tieftemperaturstrukturen für TiOCl , VOCl und CrOCl beobachtet. TiOCl zeigt zwei Phasenübergänge und bildet eine inkommensurabel modulierte intermediäre Phase. VOCl und CrOCl durchlaufen hingegen nur eine Phasenumwandlung. Im Gegensatz zu VOCl , welches unterhalb der Umwandlungstemperatur von $T_c = 80.3$ K eine monokline Phase mit γ als monoklinen Winkel bildet, bewirken die Wechselwirkungen der Metallatome in CrOCl , dass α der monokline Winkel der Tieftemperaturphase ist.

Appendix A

Supplementary material:



Table A.1: Relative atomic coordinates and equivalent isotropic atomic displacement parameters (\AA^2) for the high-temperature structure at $T = 122$ K.

atom	x	y	z	U_{eq}
Eu	0.703793(10)	0.868444(10)	0.701787(8)	0.01753(6)
S1	0.81819(6)	0.05788(6)	0.75295(6)	0.0305(3)
S2	0.56574(6)	0.74264(7)	0.75826(6)	0.0314(3)
C1	0.7679(2)	0.1486(2)	0.72070(17)	0.0207(9)
C2	0.6720(2)	0.1296(2)	0.67833(17)	0.0210(9)
C3	0.6324(3)	0.2051(2)	0.6572(2)	0.0304(11)
C4	0.6874(3)	0.3002(2)	0.6783(2)	0.0354(12)
C5	0.7830(3)	0.3181(2)	0.7183(2)	0.0294(11)
C6	0.8256(2)	0.2441(2)	0.73816(18)	0.0222(9)
C7	0.6102(2)	0.0291(2)	0.65601(17)	0.0189(9)
C8	0.5393(2)	0.0010(2)	0.70362(17)	0.0204(9)
C9	0.4793(2)	0.9083(2)	0.68104(17)	0.0216(9)
C10	0.4850(2)	0.8420(2)	0.61282(17)	0.0220(9)
C11	0.5582(2)	0.8705(2)	0.56765(17)	0.0219(9)
C12	0.6206(2)	0.9628(2)	0.58766(17)	0.0209(9)
C13	0.5261(3)	0.0714(2)	0.77723(18)	0.0280(10)
C14	0.4370(5)	0.1230(5)	0.7660(3)	0.076(2)
C15	0.5151(5)	0.0242(4)	0.8415(2)	0.069(2)
C16	0.4102(3)	0.7471(2)	0.58876(19)	0.0315(11)
C17	0.3719(13)	0.7201(11)	0.5074(8)	0.110(8)
C18	0.3369(9)	0.7196(9)	0.6387(7)	0.063(5)
C17a	0.4318(5)	0.6763(4)	0.5222(3)	0.0243(18)
C18a	0.2998(4)	0.7743(5)	0.5726(5)	0.039(2)
C19	0.6988(2)	0.9881(2)	0.53610(18)	0.0248(10)
C20	0.6512(3)	0.9699(3)	0.4551(2)	0.0405(14)
C21	0.7855(3)	0.9316(5)	0.5377(3)	0.065(2)
C22	0.9337(2)	0.2632(2)	0.7746(2)	0.0247(10)
C23	0.0134(3)	0.2541(2)	0.7274(2)	0.0310(11)
C24	0.1129(3)	0.2668(3)	0.7609(2)	0.0342(12)
C25	0.1364(2)	0.2887(3)	0.8378(2)	0.0326(12)
C26	0.0568(2)	0.2998(3)	0.8833(2)	0.0327(12)
C27	0.9552(2)	0.2865(2)	0.8526(2)	0.0278(11)

C28	0.9908(3)	0.2283(3)	0.6427(2)	0.0383(13)
C29	0.0228(7)	0.3110(5)	0.6115(4)	0.117(4)
C30	0.0351(9)	0.1423(5)	0.6049(3)	0.126(5)
C31	0.2471(3)	0.3013(3)	0.8715(2)	0.0369(13)
C32	0.2885(3)	0.4046(3)	0.9142(3)	0.0477(16)
C33	0.2613(3)	0.2305(4)	0.9191(3)	0.0508(18)
C34	0.8706(2)	0.2991(3)	0.90425(20)	0.0321(11)
C35	0.8874(3)	0.4027(3)	0.9550(3)	0.0422(14)
C36	0.8615(4)	0.2245(4)	0.9501(3)	0.0557(19)
C37	0.6187(2)	0.6575(2)	0.79606(18)	0.0217(9)
C38	0.7240(2)	0.6567(2)	0.80169(18)	0.0229(10)
C39	0.7636(2)	0.5893(3)	0.8342(2)	0.0313(12)
C40	0.6999(3)	0.5230(3)	0.8612(2)	0.0342(13)
C41	0.5954(2)	0.5221(3)	0.85436(20)	0.0284(11)
C42	0.5536(2)	0.5882(2)	0.82207(18)	0.0218(9)
C43	0.7950(2)	0.7258(2)	0.77197(18)	0.0219(9)
C44	0.8453(2)	0.8156(2)	0.82008(18)	0.0233(10)
C45	0.9139(2)	0.8766(2)	0.79102(19)	0.0263(10)
C46	0.9378(2)	0.8527(2)	0.7168(2)	0.0260(10)
C47	0.8848(2)	0.7644(2)	0.6700(2)	0.0255(10)
C48	0.8143(2)	0.7011(2)	0.69584(18)	0.0224(9)
C49	0.8283(3)	0.8449(3)	0.90265(19)	0.0312(11)
C50	0.9270(8)	0.9022(10)	0.9530(5)	0.052(4)
C51	0.7445(9)	0.9086(9)	0.9150(6)	0.054(5)
C50a	0.9249(6)	0.8303(7)	0.9480(4)	0.047(3)
C51a	0.8047(8)	0.9440(6)	0.9300(5)	0.046(3)
C52	0.0192(2)	0.9194(3)	0.6903(2)	0.0352(13)
C53	0.071(2)	0.8568(16)	0.6241(16)	0.123(13)
C54	0.0873(10)	0.9882(14)	0.7477(10)	0.072(7)
C53a	0.0455(7)	0.8819(7)	0.6157(7)	0.040(3)
C54a	0.1211(6)	0.9445(7)	0.7458(6)	0.051(3)
C55	0.7618(3)	0.6051(2)	0.64167(19)	0.0296(11)
C56	0.8383(4)	0.5359(3)	0.6230(3)	0.0516(17)
C57	0.7107(4)	0.6208(3)	0.5709(3)	0.0571(18)
C58	0.4402(2)	0.5823(2)	0.81210(18)	0.0221(9)
C59	0.3821(2)	0.5168(2)	0.74846(19)	0.0259(10)

C60	0.2781(2)	0.5172(3)	0.7370(2)	0.0301(11)
C61	0.2295(2)	0.5801(3)	0.7865(2)	0.0312(12)
C62	0.2871(2)	0.6422(3)	0.8506(2)	0.0310(11)
C63	0.3925(2)	0.6452(2)	0.8643(2)	0.0277(11)
C64	0.4332(3)	0.4498(3)	0.6906(2)	0.0326(12)
C65	0.384(2)	0.3480(17)	0.6783(15)	0.098(12)
C66	0.431(2)	0.4834(18)	0.6135(12)	0.134(16)
C65a	0.3724(13)	0.3441(11)	0.6591(8)	0.038(3)
C66a	0.4585(9)	0.4952(9)	0.6282(6)	0.038(3)
C67	0.1153(3)	0.5797(3)	0.7707(2)	0.0387(14)
C68	0.0546(3)	0.5317(4)	0.8211(3)	0.0472(17)
C69	0.0923(4)	0.6781(4)	0.7712(5)	0.090(3)
C70	0.4522(3)	0.7148(3)	0.9343(2)	0.0375(12)
C71	0.4284(3)	0.6809(3)	0.0045(2)	0.0447(15)
C72	0.4336(4)	0.8186(3)	0.9416(3)	0.0581(18)
H3	0.5676	0.1916	0.6283	0.0365
H4	0.6600	0.3523	0.6656	0.0424
H5	0.8204	0.3828	0.7326	0.0352
H9	0.4322	0.8896	0.7137	0.0259
H11	0.5658	0.8258	0.5218	0.0263
H13	0.5875	0.1180	0.7917	0.0336
H14a	0.4377	0.1757	0.8089	0.0911
H14b	0.4429	0.1473	0.7225	0.0911
H14c	0.3746	0.0783	0.7596	0.0911
H15a	0.5285	0.0731	0.8879	0.0832
H15b	0.4474	0.9892	0.8372	0.0832
H15c	0.5624	0.9806	0.8402	0.0832
H16	0.4517	0.7015	0.5971	0.0377
H17a	0.4263	0.7051	0.4782	0.1321
H17b	0.3189	0.6647	0.4968	0.1321
H17c	0.3460	0.7732	0.4950	0.1321
H18a	0.2874	0.7613	0.6436	0.0759
H18b	0.3039	0.6539	0.6181	0.0759
H18c	0.3718	0.7257	0.6868	0.0759
H17d	0.4352	0.7053	0.4809	0.0292
H17e	0.4954	0.6570	0.5326	0.0292

H17f	0.3789	0.6207	0.5099	0.0292
H18d	0.2968	0.7949	0.5272	0.0467
H18e	0.2485	0.7186	0.5677	0.0467
H18f	0.2887	0.8256	0.6132	0.0467
H19	0.7254	0.0558	0.5549	0.0298
H20a	0.6998	0.9959	0.4265	0.0486
H20b	0.6310	0.9017	0.4338	0.0486
H20c	0.5930	0.0009	0.4546	0.0486
H21a	0.8341	0.9499	0.5060	0.0779
H21b	0.8174	0.9457	0.5878	0.0779
H21c	0.7594	0.8637	0.5203	0.0779
H24	0.1671	0.2602	0.7300	0.0411
H26	0.0721	0.3169	0.9365	0.0392
H28	0.9186	0.2120	0.6311	0.0460
H29a	0.9945	0.2962	0.5604	0.1400
H29b	0.9993	0.3669	0.6395	0.1400
H29c	0.0953	0.3239	0.6142	0.1400
H30a	0.0851	0.1303	0.6393	0.1506
H30b	0.9823	0.0867	0.5889	0.1506
H30c	0.0661	0.1549	0.5625	0.1506
H31	0.2869	0.2871	0.8305	0.0442
H32a	0.2802	0.4469	0.8825	0.0572
H32b	0.2524	0.4218	0.9569	0.0572
H32c	0.3591	0.4106	0.9303	0.0572
H33a	0.2568	0.1667	0.8871	0.0609
H33b	0.3265	0.2500	0.9478	0.0609
H33c	0.2094	0.2303	0.9521	0.0609
H34	0.8074	0.2878	0.8735	0.0385
H35a	0.8322	0.4099	0.9849	0.0507
H35b	0.9496	0.4147	0.9869	0.0507
H35c	0.8907	0.4480	0.9247	0.0507
H36a	0.8027	0.2286	0.9765	0.0669
H36b	0.8552	0.1610	0.9175	0.0669
H36c	0.9208	0.2370	0.9852	0.0669
H39	0.8350	0.5886	0.8381	0.0375
H40	0.7276	0.4785	0.8841	0.0410

H41	0.5517	0.4756	0.8721	0.0340
H45	0.9460	0.9376	0.8234	0.0315
H47	0.8973	0.7468	0.6186	0.0306
H49	0.8076	0.7852	0.9156	0.0375
H50a	0.9844	0.8757	0.9345	0.0627
H50b	0.9350	0.9689	0.9522	0.0627
H50c	0.9223	0.8970	0.0032	0.0627
H51a	0.6869	0.8795	0.8789	0.0654
H51b	0.7246	0.9139	0.9643	0.0654
H51c	0.7703	0.9718	0.9095	0.0654
H50d	0.9468	0.7724	0.9221	0.0562
H50e	0.9780	0.8846	0.9531	0.0562
H50f	0.9089	0.8250	0.9965	0.0562
H51d	0.8017	0.9579	0.9830	0.0553
H51e	0.8567	0.9903	0.9191	0.0553
H51f	0.7406	0.9475	0.9057	0.0553
H52	0.9880	0.9686	0.6759	0.0423
H53a	0.0693	0.7929	0.6307	0.1480
H53b	0.0344	0.8531	0.5770	0.1480
H53c	0.1398	0.8870	0.6252	0.1480
H54a	0.0594	0.0462	0.7628	0.0863
H54b	0.0971	0.9617	0.7897	0.0863
H54c	0.1512	0.0029	0.7292	0.0863
H53d	0.9851	0.8621	0.5812	0.0480
H53e	0.0902	0.9313	0.6017	0.0480
H53f	0.0786	0.8274	0.6148	0.0480
H54d	0.1459	0.8861	0.7468	0.0613
H54e	0.1710	0.9869	0.7290	0.0613
H54f	0.1077	0.9757	0.7950	0.0613
H55	0.7089	0.5763	0.6656	0.0355
H56a	0.8640	0.5217	0.6678	0.0619
H56b	0.8051	0.4771	0.5882	0.0619
H56c	0.8932	0.5658	0.6013	0.0619
H57a	0.6744	0.5602	0.5405	0.0686
H57b	0.6644	0.6649	0.5840	0.0686
H57c	0.7611	0.6472	0.5438	0.0686

H62	0.2536	0.6835	0.8858	0.0372
H60	0.2389	0.4731	0.6939	0.0361
H64	0.5007	0.4505	0.7114	0.0391
H65a	0.3826	0.3318	0.7254	0.1175
H65b	0.3167	0.3391	0.6548	0.1175
H65c	0.4224	0.3069	0.6469	0.1175
H65d	0.3149	0.3449	0.6259	0.0458
H65e	0.4155	0.3038	0.6326	0.0458
H65f	0.3499	0.3191	0.6997	0.0458
H67	0.0924	0.5418	0.7208	0.0464
H68a	0.0731	0.4698	0.8192	0.0567
H68b	0.0684	0.5713	0.8714	0.0567
H68c	-0.0162	0.5234	0.8049	0.0567
H69a	0.1100	0.6942	0.7260	0.1082
H69b	0.0214	0.6781	0.7748	0.1082
H69c	0.1309	0.7250	0.8133	0.1082
H70	0.5228	0.7145	0.9293	0.0451
H71a	0.4674	0.7255	0.0475	0.0537
H71b	0.3576	0.6782	0.0098	0.0537
H71c	0.4455	0.6179	0.9999	0.0537
H72a	0.4812	0.8624	0.9802	0.0697
H72b	0.4419	0.8352	0.8951	0.0697
H72c	0.3660	0.8230	0.9539	0.0697
H66a	0.4726	0.5460	0.6218	0.1602
H66b	0.4572	0.4377	0.5761	0.1602
H66c	0.3629	0.4865	0.5968	0.1602
H66d	0.5039	0.5555	0.6479	0.0456
H66e	0.4904	0.4528	0.5926	0.0456
H66f	0.3976	0.5064	0.6043	0.0456

Table A.2: Anisotropic displacement parameter (\AA^2) of non-hydrogen atoms in the high-temperature structure at $T = 122$ K.

atom	\mathbf{U}_{11}	\mathbf{U}_{22}	\mathbf{U}_{33}	\mathbf{U}_{12}	\mathbf{U}_{13}	\mathbf{U}_{23}
Eu	0.01237(9)	0.01828(10)	0.02124(10)	0.00149(5)	-0.00121(5)	0.00528(5)
S1	0.0192(4)	0.0210(4)	0.0477(5)	0.0001(3)	-0.0141(3)	0.0092(3)
S2	0.0151(3)	0.0365(5)	0.0529(6)	0.0070(3)	0.0064(3)	0.0285(4)
C1	0.0147(13)	0.0197(14)	0.0257(15)	0.0028(10)	-0.0013(11)	0.0031(11)
C2	0.0152(13)	0.0195(14)	0.0259(15)	0.0019(10)	-0.0006(11)	0.0029(11)
C3	0.0233(16)	0.0246(16)	0.0388(19)	0.0051(12)	-0.0109(14)	0.0032(13)
C4	0.0321(18)	0.0213(17)	0.051(2)	0.0070(13)	-0.0103(16)	0.0079(14)
C5	0.0277(16)	0.0155(15)	0.041(2)	0.0010(11)	-0.0037(14)	0.0044(12)
C6	0.0155(13)	0.0193(14)	0.0296(16)	0.0013(10)	-0.0003(11)	0.0037(11)
C7	0.0125(12)	0.0197(14)	0.0219(14)	0.0021(10)	-0.0039(10)	0.0023(10)
C8	0.0161(13)	0.0244(15)	0.0202(14)	0.0060(10)	0.0001(11)	0.0040(11)
C9	0.0155(13)	0.0279(16)	0.0217(14)	0.0029(11)	0.0013(11)	0.0077(11)
C10	0.0148(13)	0.0249(15)	0.0231(15)	-0.0016(10)	-0.0052(11)	0.0051(11)
C11	0.0188(14)	0.0243(15)	0.0180(14)	0.0012(10)	-0.0012(11)	-0.0008(11)
C12	0.0134(13)	0.0281(15)	0.0190(14)	0.0011(10)	-0.0011(10)	0.0039(11)
C13	0.0267(16)	0.0310(17)	0.0235(16)	0.0083(12)	0.0032(12)	-0.0006(12)
C14	0.075(4)	0.106(5)	0.047(3)	0.063(4)	0.006(3)	-0.011(3)
C15	0.132(6)	0.051(3)	0.024(2)	0.025(3)	0.012(3)	0.0025(18)
C16	0.0294(17)	0.0263(17)	0.0336(18)	-0.0095(12)	-0.0053(14)	0.0091(13)
C17	0.143(15)	0.086(12)	0.062(8)	-0.095(12)	-0.037(9)	0.028(8)
C18	0.049(6)	0.063(8)	0.069(8)	-0.023(5)	-0.012(5)	0.027(6)
C17a	0.028(3)	0.023(3)	0.017(3)	0.001(2)	-0.004(2)	-0.001(2)
C18a	0.012(3)	0.027(3)	0.067(5)	-0.002(2)	-0.007(3)	-0.001(3)
C19	0.0190(14)	0.0294(16)	0.0249(15)	0.0007(11)	0.0041(12)	0.0065(12)
C20	0.0278(18)	0.065(3)	0.035(2)	-0.0001(16)	0.0014(15)	0.0295(18)
C21	0.034(2)	0.129(5)	0.063(3)	0.043(3)	0.026(2)	0.061(3)
C22	0.0160(14)	0.0195(15)	0.0365(18)	0.0004(10)	-0.0005(12)	0.0056(12)
C23	0.0209(15)	0.0263(17)	0.041(2)	0.0009(12)	0.0040(14)	0.0009(13)
C24	0.0191(15)	0.0340(19)	0.047(2)	0.0016(12)	0.0053(14)	0.0062(15)
C25	0.0153(14)	0.0324(18)	0.050(2)	0.0010(12)	0.0013(14)	0.0133(15)
C26	0.0200(16)	0.037(2)	0.039(2)	-0.0039(13)	-0.0054(14)	0.0137(15)
C27	0.0179(14)	0.0270(17)	0.0360(18)	-0.0017(11)	-0.0018(13)	0.0080(13)

C28	0.0275(18)	0.039(2)	0.040(2)	0.0009(14)	0.0062(15)	-0.0022(16)
C29	0.219(10)	0.053(4)	0.055(4)	-0.032(4)	-0.051(5)	0.023(3)
C30	0.291(12)	0.080(5)	0.036(3)	0.107(6)	0.050(5)	0.017(3)
C31	0.0175(15)	0.052(2)	0.043(2)	0.0042(14)	0.0033(14)	0.0178(17)
C32	0.029(2)	0.049(2)	0.060(3)	-0.0065(16)	-0.0164(18)	0.017(2)
C33	0.0251(19)	0.063(3)	0.073(3)	0.0084(18)	-0.0029(19)	0.037(2)
C34	0.0163(15)	0.043(2)	0.0301(17)	-0.0046(13)	-0.0007(13)	0.0024(14)
C35	0.0255(18)	0.036(2)	0.058(3)	0.0024(14)	-0.0034(17)	0.0012(17)
C36	0.065(3)	0.048(3)	0.063(3)	0.012(2)	0.035(3)	0.021(2)
C37	0.0137(13)	0.0266(15)	0.0256(15)	0.0029(10)	-0.0003(11)	0.0093(11)
C38	0.0144(13)	0.0287(16)	0.0277(16)	0.0032(11)	0.0012(11)	0.0118(12)
C39	0.0165(14)	0.043(2)	0.041(2)	0.0088(13)	0.0013(13)	0.0213(15)
C40	0.0256(17)	0.040(2)	0.046(2)	0.0084(14)	0.0016(15)	0.0268(16)
C41	0.0237(15)	0.0306(18)	0.0358(18)	0.0027(12)	0.0031(13)	0.0195(13)
C42	0.0157(13)	0.0257(15)	0.0250(15)	0.0016(10)	0.0007(11)	0.0101(11)
C43	0.0115(12)	0.0265(16)	0.0287(16)	0.0034(10)	-0.0004(11)	0.0100(12)
C44	0.0166(13)	0.0273(16)	0.0272(16)	0.0048(11)	-0.0027(11)	0.0102(12)
C45	0.0152(14)	0.0272(16)	0.0355(18)	0.0010(11)	-0.0047(12)	0.0101(13)
C46	0.0136(13)	0.0298(17)	0.0386(18)	0.0041(11)	0.0005(12)	0.0166(13)
C47	0.0175(14)	0.0306(17)	0.0320(17)	0.0061(11)	0.0055(12)	0.0129(13)
C48	0.0171(13)	0.0221(15)	0.0295(16)	0.0055(10)	0.0028(11)	0.0081(11)
C49	0.0294(17)	0.039(2)	0.0243(16)	0.0005(13)	-0.0027(13)	0.0107(13)
C50	0.047(6)	0.069(7)	0.030(5)	0.000(5)	-0.013(4)	0.003(5)
C51	0.056(7)	0.081(9)	0.030(5)	0.025(6)	0.015(5)	0.012(5)
C50a	0.040(4)	0.067(6)	0.035(4)	0.000(4)	-0.008(3)	0.025(4)
C51a	0.055(5)	0.052(5)	0.031(4)	0.016(4)	0.008(4)	0.007(3)
C52	0.0207(16)	0.036(2)	0.057(2)	0.0043(13)	0.0080(15)	0.0255(17)
C53	0.14(2)	0.073(15)	0.16(3)	-0.005(14)	0.14(2)	0.007(14)
C54	0.026(7)	0.092(13)	0.074(10)	-0.028(7)	0.025(7)	-0.008(10)
C53a	0.026(3)	0.036(5)	0.061(5)	0.002(3)	0.023(3)	0.017(4)
C54a	0.017(4)	0.066(6)	0.065(6)	-0.014(3)	0.005(4)	0.020(5)
C55	0.0288(17)	0.0259(17)	0.0321(18)	-0.0020(12)	0.0047(13)	0.0074(13)
C56	0.048(3)	0.027(2)	0.073(3)	0.0084(17)	0.005(2)	-0.0009(19)
C57	0.073(3)	0.040(2)	0.048(3)	0.000(2)	-0.027(2)	0.0056(19)
C58	0.0164(13)	0.0237(15)	0.0280(16)	0.0000(10)	0.0019(11)	0.0121(11)
C59	0.0208(15)	0.0306(17)	0.0273(16)	0.0001(12)	0.0006(12)	0.0124(12)

C60	0.0217(15)	0.0352(18)	0.0319(18)	-0.0035(12)	-0.0044(13)	0.0127(14)
C61	0.0183(15)	0.0365(19)	0.042(2)	0.0021(12)	0.0002(13)	0.0194(15)
C62	0.0201(15)	0.0331(18)	0.041(2)	0.0053(12)	0.0076(14)	0.0111(14)
C63	0.0192(15)	0.0285(17)	0.0332(18)	-0.0020(11)	0.0042(12)	0.0071(13)
C64	0.0304(18)	0.0346(19)	0.0292(18)	-0.0011(13)	0.0042(14)	0.0051(14)
C65	0.090(18)	0.056(12)	0.16(3)	0.035(11)	0.083(19)	0.017(14)
C66	0.30(4)	0.099(17)	0.029(9)	0.10(2)	0.026(15)	0.024(10)
C65a	0.046(6)	0.021(4)	0.040(4)	-0.007(4)	0.012(4)	-0.001(3)
C66a	0.049(5)	0.036(4)	0.025(5)	-0.004(3)	0.016(4)	0.004(3)
C67	0.0195(16)	0.048(2)	0.050(2)	0.0049(14)	-0.0052(15)	0.0186(18)
C68	0.0153(16)	0.062(3)	0.070(3)	0.0044(16)	0.0099(17)	0.028(2)
C69	0.034(3)	0.071(4)	0.184(8)	0.008(2)	-0.015(4)	0.075(4)
C70	0.0223(17)	0.045(2)	0.0342(19)	-0.0081(14)	0.0071(14)	-0.0030(15)
C71	0.036(2)	0.056(3)	0.038(2)	-0.0022(17)	-0.0050(17)	0.0106(18)
C72	0.085(4)	0.037(2)	0.040(2)	-0.016(2)	0.018(2)	-0.0025(18)

Appendix B

Supplementary material: TiI_3

Table B.1: Anisotropic atomic displacement parameters at different temperatures (\AA^2)

	U_{11}	U_{22}	U_{33}	U_{12}
100 K				
Ti	0.0072(5)	0.0083(3)	0.0083(3)	0.0036(2)
I1	0.0066(2)	0.0117(2)	0.0082(2)	0.00475(17)
I2	0.0074(2)	0.0125(2)	0.0081(2)	0.00605(17)
I3	0.0124(3)	0.00797(18)	0.0108(3)	0.00619(16)
I4	0.0096(3)	0.00810(18)	0.0107(3)	0.00479(15)
273 K				
Ti	0.0237(8)	0.0180(4)	0.0192(4)	0.0119(4)
I1	0.0231(4)	0.0332(3)	0.0189(3)	0.0166(3)
I2	0.0247(4)	0.0339(3)	0.0186(3)	0.0184(3)
I3	0.0342(6)	0.0201(2)	0.0242(3)	0.0171(3)
I4	0.0298(6)	0.0194(2)	0.0232(3)	0.0149(3)
326 K				
Ti	0.0186(4)	0.0186(4)	0.0358(5)	0.00930(19)
I	0.0227(2)	0.0360(3)	0.0196(3)	0.01801(13)

Appendix C

Crystal twinning of TiI_3

At temperatures below the transition temperature diffraction experiments on single-crystals of TiI_3 evidenced the occurrence of superstructure reflections whose intensities were many times weaker than the average main reflection intensities. To allow for an indexing of also the superstructure reflections the reciprocal cell of a 2×2 -supercell of the hexagonal pseudocell can be used. Alternatively the reflections can be indexed by three C-centred orthorhombic unit cells employing the orthohexagonal relation. The indexing can be carried out by rotating the cells from each another about the lattice direction \mathbf{c} using angles of 120 deg. The indexing relies on the assumption that the low-temperature phase is formed by three orientations of twin domains of orthorhombic symmetry. Indeed, for RuBr_3 and ZrI_3 also untwinned single-crystals were found from whose examination unmasked orthorhombic crystal structures were determined (Brodersen, Breitbach and Thiele (1968); Lachgar et al. (1990)). The diffraction pattern of the low-temperature phase of TiI_3 exhibits reflection intensities which are adequately be described by a superposition of the reflection intensities from three single domains. The superposition of the three sublattices of the domains causes a coincidence of the three domain contributions at the positions of the main reflections and an occurrence of single domain contributions at the centers of the orthorhombic reciprocal unit cells (Fig. C.1).

Because of the different orientations of the three domain sublattices in general a different indexing for the three domain contributions occurs (i.e one reflection hkl is indexed as h_1, k_1l , h_2, k_2l or h_3, k_3l dependent on which domain one refers the indexing to). In the following the indexation will refer to an indexing carried out using the unit cell of domain one and suffixes are used to discriminate different reflections. Main reflections are indexed according to the reflection condition $h+k=2n$. The

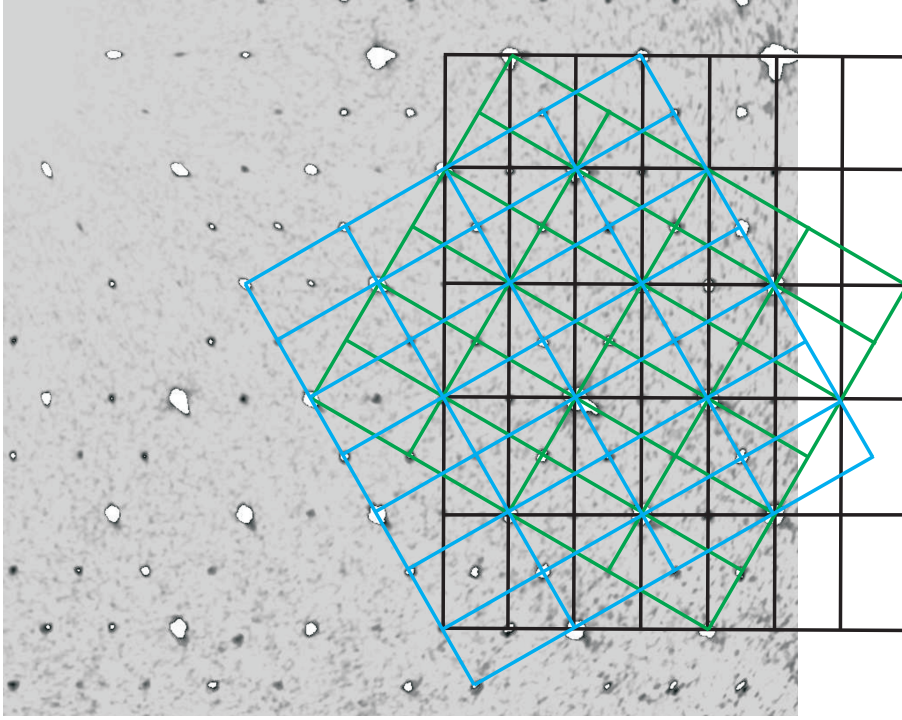


Figure C.1: Reconstructed reciprocal lattice plane $hk0$ of the low-temperature phase of TiI_3 . The graphic was overlain by grids to allow an easy assignment of reflections contributions belonging to the same sublattice.

superstructure reflections resulting from the contribution of domain one are indexed by $h+k=2n+1$. The superstructure reflections belonging to the other two domains occur at the center of the reciprocal unit cell of domain one and thus possess non integer values for their indices h and k . The superstructure reflections belonging to the second domain should possess the indices $h_2 = 2n_2 + \frac{1}{2}$ and $k_2 = 2m_2 + \frac{1}{2}$ forming the reflection condition $h_2 + k_2 = 2(n_2 + m_2) + 1$. The superstructure reflections of the third domain can then be indexed by $h_3 = 2n_3 + \frac{1}{2}$ and $k_3 = 2m_3 - \frac{1}{2}$ and the reflection condition is $h_3 + k_3 = 2(n_3 + m_3)$. As indicated by the reflection conditions the sum of the indices h and k has to be even for the superstructure reflections of the second domain while it has to be odd for the superstructure reflection of the third domain.

Appendix D

Monoclinic angle in the unit cell of CrOCl

The value of the monoclinic angle α was calculated from the 2θ splitting of the reflection (0 -2 5). The expression relating the angle α with the scattering angle 2θ was derived from the squared Bragg equation:

$$\left(\frac{1}{d}\right)^2 = 4 \cdot \frac{\sin^2(\theta)}{\lambda^2}, \quad (\text{D.1})$$

in which λ stands for the wavelength and $(\frac{1}{d})$ represents the length of the scattering vector. Employing the reciprocal lattice vectors \vec{b}^* and \vec{c}^* the scattering vectors of the reflections (0 k l) can be calculated as

$$\left(\frac{1}{d}\right)^2 = k^2|\vec{b}^*|^2 + l^2|\vec{c}^*|^2 + 2kl|\vec{b}^*||\vec{c}^*| \cdot \cos(\alpha^*). \quad (\text{D.2})$$

The difference of the squared scattering vectors resulting for the twinned reflections (0 k l) and (0 -k l) is equal to:

$$\begin{aligned} \left(\frac{1}{d_2}\right)^2 - \left(\frac{1}{d_1}\right)^2 &= \left(k^2|\vec{b}^*|^2 + l^2|\vec{c}^*|^2 + 2kl|\vec{b}^*||\vec{c}^*| \cdot \cos(\alpha_2^*)\right) - \\ &\quad \left(k^2|\vec{b}^*|^2 + l^2|\vec{c}^*|^2 + 2kl|\vec{b}^*||\vec{c}^*| \cdot \cos(\alpha_1^*)\right) \\ &= 2kl|\vec{b}^*||\vec{c}^*| \cdot (\cos(\alpha_2^*) - \cos(\alpha_1^*)). \end{aligned} \quad (\text{D.3})$$

Considering that $\cos(\alpha_1^*) = -\cos(\alpha_2^*)$ the expression can be rewritten as

$$\left(\frac{1}{d_2}\right)^2 - \left(\frac{1}{d_1}\right)^2 = 4kl|\vec{b}^*||\vec{c}^*| \cdot \cos \alpha_2^*. \quad (\text{D.4})$$

According to equation D.1 the difference of the squared scattering vectors can be expressed in dependence of a splitting in θ by:

$$\left(\frac{1}{d_2}\right)^2 - \left(\frac{1}{d_1}\right)^2 = 4 \cdot \frac{\sin^2(\theta_2) - \sin^2(\theta_1)}{\lambda^2}. \quad (\text{D.5})$$

Combining equation D.4 with equation D.5 allows the calculation of the reciprocal monoclinic angle α^* as:

$$\alpha^* = \arccos \left(\frac{\sin^2(\theta_2) - \sin^2(\theta_1)}{kl|\vec{b}^*||\vec{c}^*| \cdot \lambda^2} \right) \quad (\text{D.6})$$

and the monoclinic angle α through:

$$\alpha = 180^\circ - \alpha^* = 180^\circ - \arccos \left(\frac{\sin^2(\theta_2) - \sin^2(\theta_1)}{kl|\vec{b}^*||\vec{c}^*| \cdot \lambda^2} \right). \quad (\text{D.7})$$

Appendix E

Measured reflection profiles of CrOCl

In the following reflection profiles are presented which were measured by X-ray diffraction experiments on single-crystals of CrOCl employing a point detector. The experiments were carried out by using synchrotron radiation taking advantage of its high monochromaticity by which a peak splitting caused by twinning was determined.

E.1 Profiles of 2θ -dependent ω -scans

ω - 2θ maps performed by rotating the crystal in angle increments of 0.002 deg about ω and the repetition of the ω -scans for a variation of the detector position by angle increments of 0.002 deg in 2θ . The measuring time for the ω -scans was chosen to be 1 s per step.

E.1.1 Profiles measured on reflection (0 -2 5)

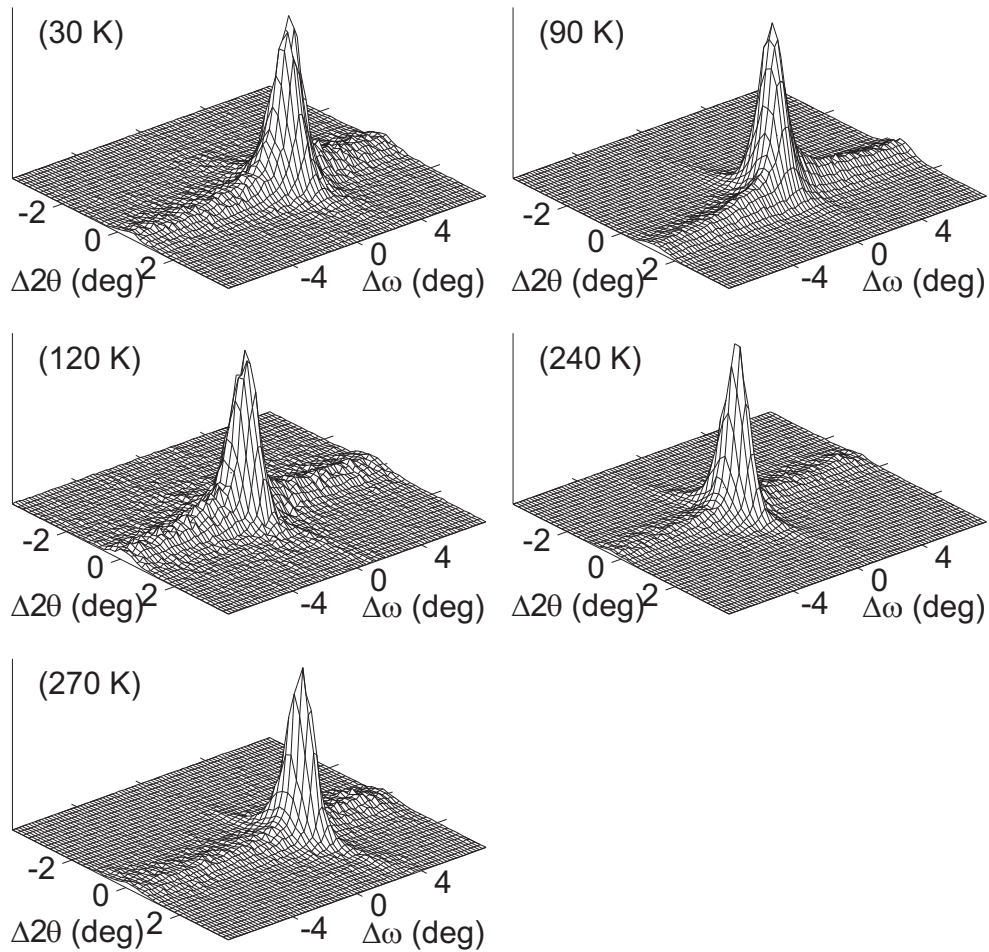


Figure E.1: ω - 2θ maps of (0 -2 5). The scattering angles were $2\theta = 2\theta_c + (\Delta 2\theta/100)$ deg and the crystal orientations were $\omega = \omega_c + (\Delta\omega/100)$ deg. The reflections were centered at $2\theta_c, \omega_c$ (deg): 37.527, 18.677 30 K; 37.507, 18.778 90 K; 37.495, 18.754 120 K; 37.452, 18.775 240 K; 37.428, 18.403 270 K. Crystal temperatures are indicated.

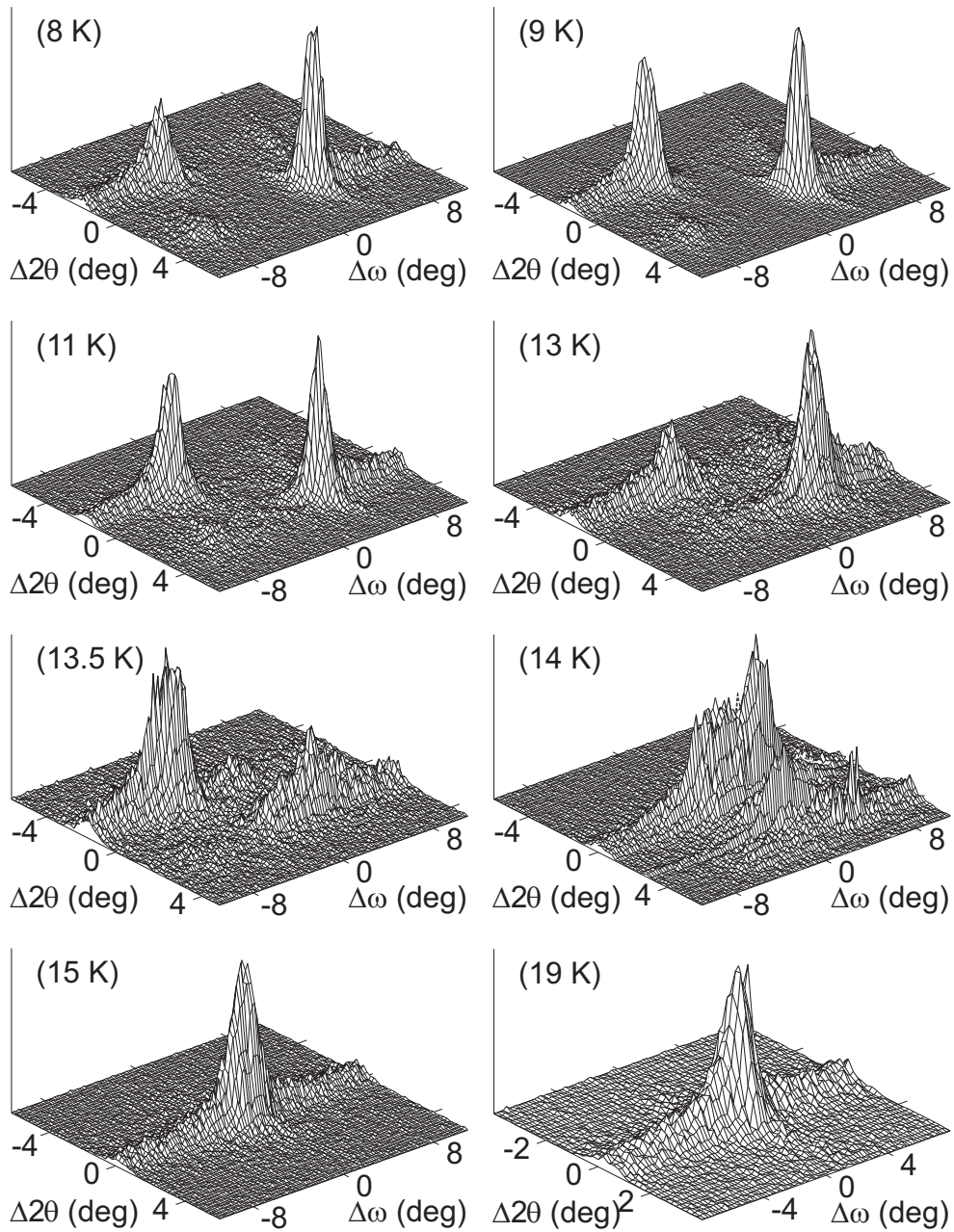


Figure E.2: ω - 2θ maps of (0 -2 5). The reflections were centered at $2\theta_c, \omega_c$ (deg): 37.543, 18.78 8 K; 37.539, 18.78 9 K; 37.544, 18.74 11 K; 37.545, 18.71 13 K; 37.538, 18.75 13.5 K; 37.520, 18.72 14 K; 37.543, 18.76 15 K; 37.539, 18.78 19 K. Crystal temperatures are indicated.

E.1.2 Profiles measured on reflection (2 0 4)

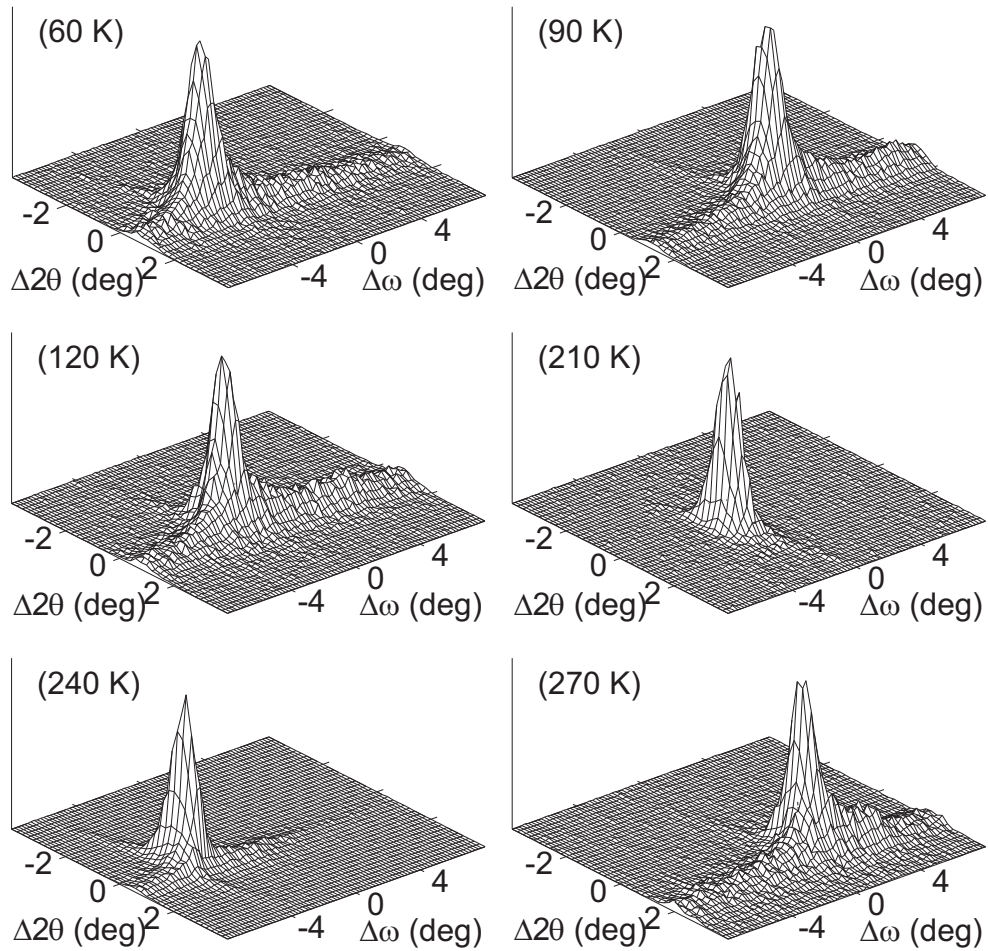


Figure E.3: ω - 2θ maps of (2 0 4). The scattering angles were $2\theta = 2\theta_c + (\Delta 2\theta/100)$ deg and the crystal orientations were $\omega = \omega_c + (\Delta\omega/100)$ deg. The reflections were centered at $2\theta_c$, ω_c (deg): 30.230, 15.212 60 K; 30.218, 15.259 90 K; 30.207, 15.263 120 K; 30.194, 15.274 210 K; 30.178, 15.436 240 K; 30.149, 15.331 270 K. Crystal temperatures are indicated.

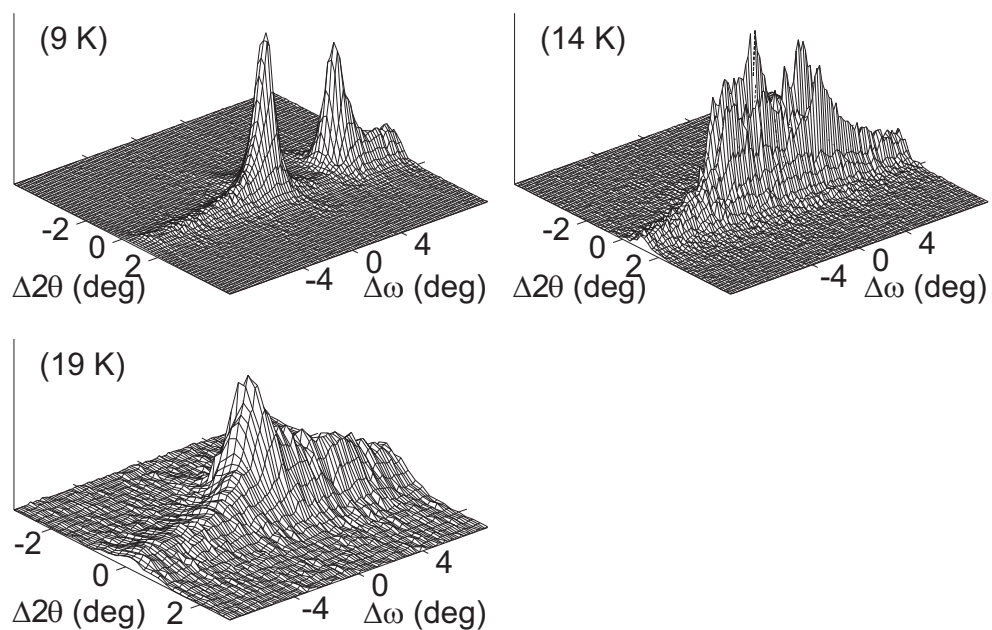


Figure E.4: ω - 2θ maps of (2 0 4). Reflections were centered at $2\theta_c, \omega_c$ (deg): 30.247, 15.148 9 K; 30.241, 15.150 14 K; 30.255, 15.171 19 K. Crystal temperatures are indicated.

E.1.3 Profiles measured on reflection (2 -2 0)

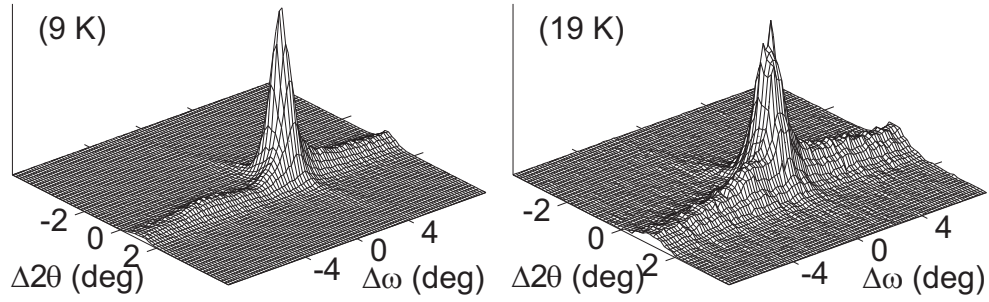


Figure E.5: ω - 2θ maps of (2 -2 0). The scattering angles were $2\theta = 2\theta_c + (\Delta 2\theta/100)$ deg and the crystal orientations were $\omega = \omega_c + (\Delta\omega/100)$ deg. The reflections were centered at $2\theta_c, \omega_c$ (deg): 33.640, 16.847 9 K; 33.640, 16.852 19 K. Crystal temperatures are indicated.

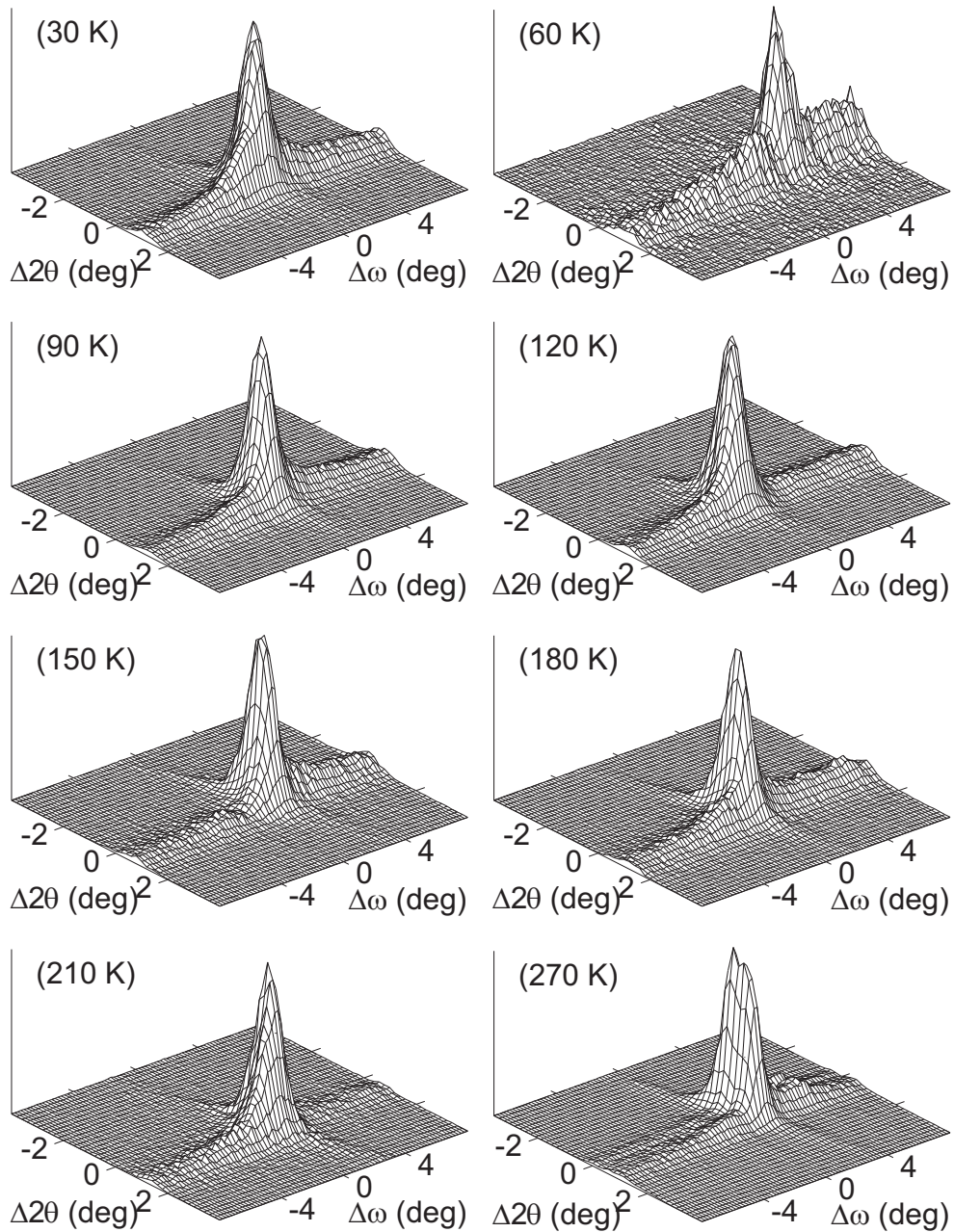


Figure E.6: ω - 2θ maps of (2 -2 0). The scattering angles were $2\theta = 2\theta_c + (\Delta 2\theta/100)$ deg and the crystal orientations were $\omega = \omega_c + (\Delta\omega/100)$ deg. Reflections were centered at $2\theta_c, \omega_c$ (deg): 33.638, 16.842 30 K; 33.645, 16.878 60 K; 33.642, 16.884 90 K; 33.639, 16.883 120 K; 33.641, 16.872 150 K; 33.630, 16.828 180 K; 33.645, 16.884 210 K; 33.633, 16.475 270 K. Crystal temperatures are indicated.

E.2 Scans on superstructure reflections of CrOCl

The superstructure reflections were measured in q -scans using an exposal time of 16 s per step and in ω -scans using an exposal time of 15 s per step.

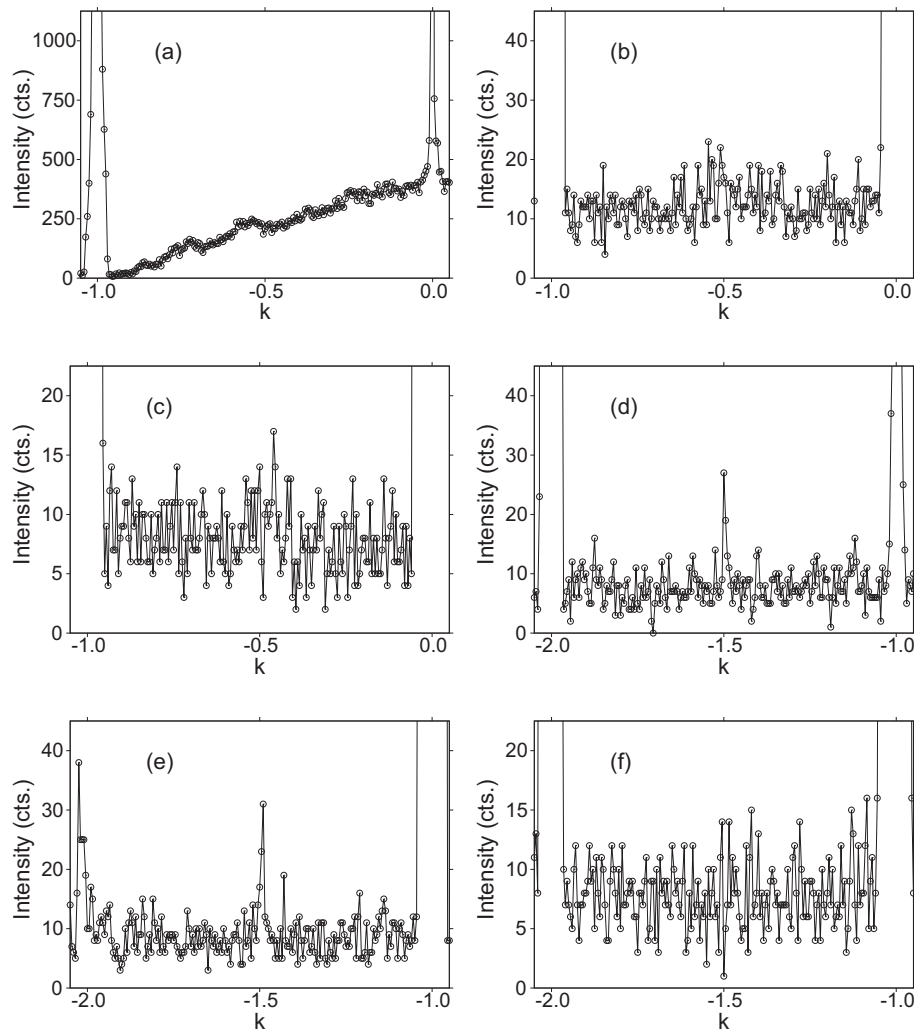


Figure E.7: q -scans measured along \mathbf{b}^* with step increments of 0.0055 in k . The scan center are positioned at 1 -0.5 2 (a), 1 -0.5 3 (b), 1 -0.5 4 (c), 2 -1.5 1 (d), 2 -1.5 2 (e) and 2 -1.5 4 (f) respectively.

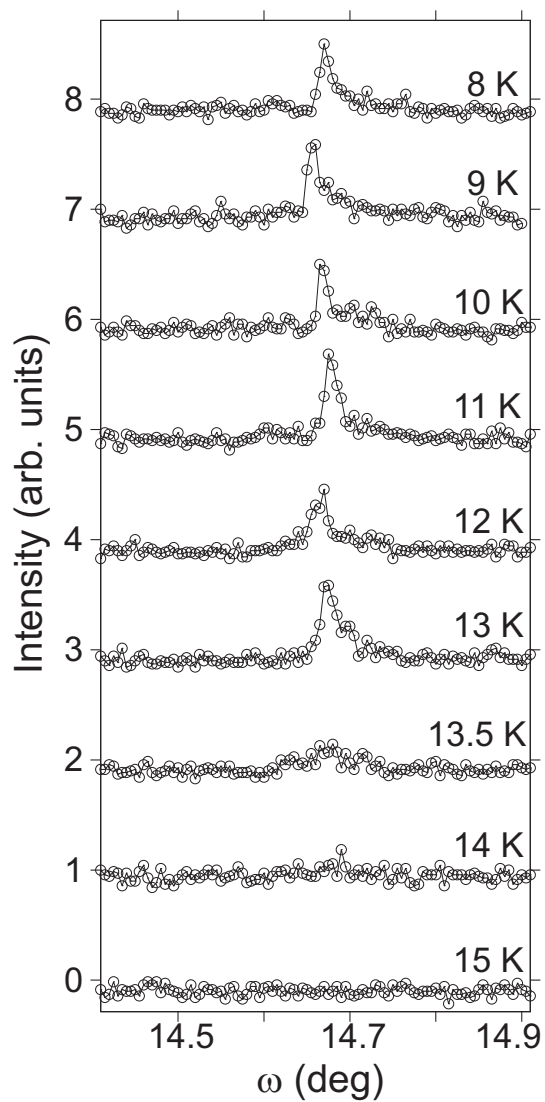


Figure E.8: ω -scans on the superstructure reflection (2 -1.5 1) for different temperatures.

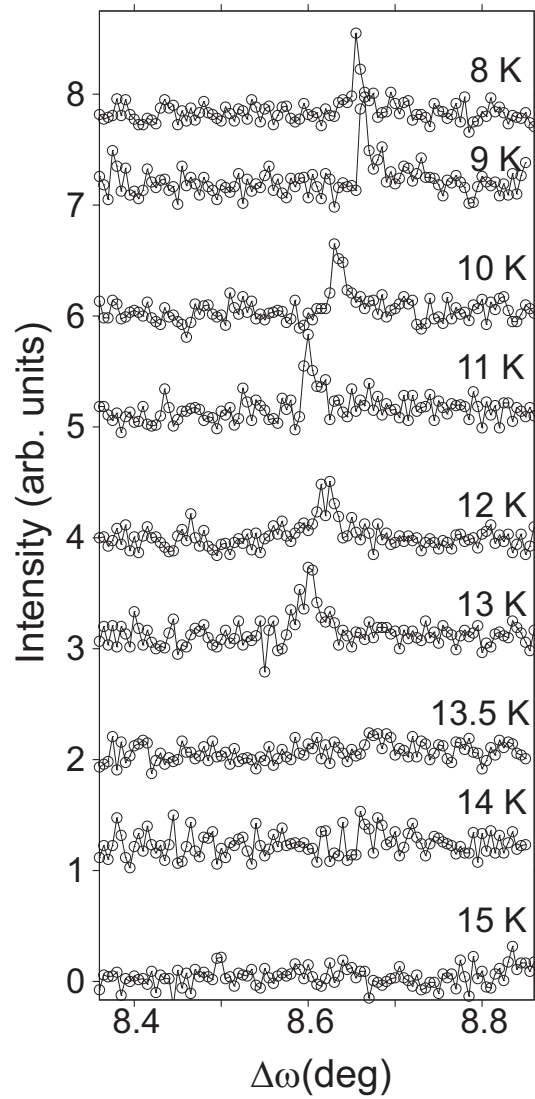
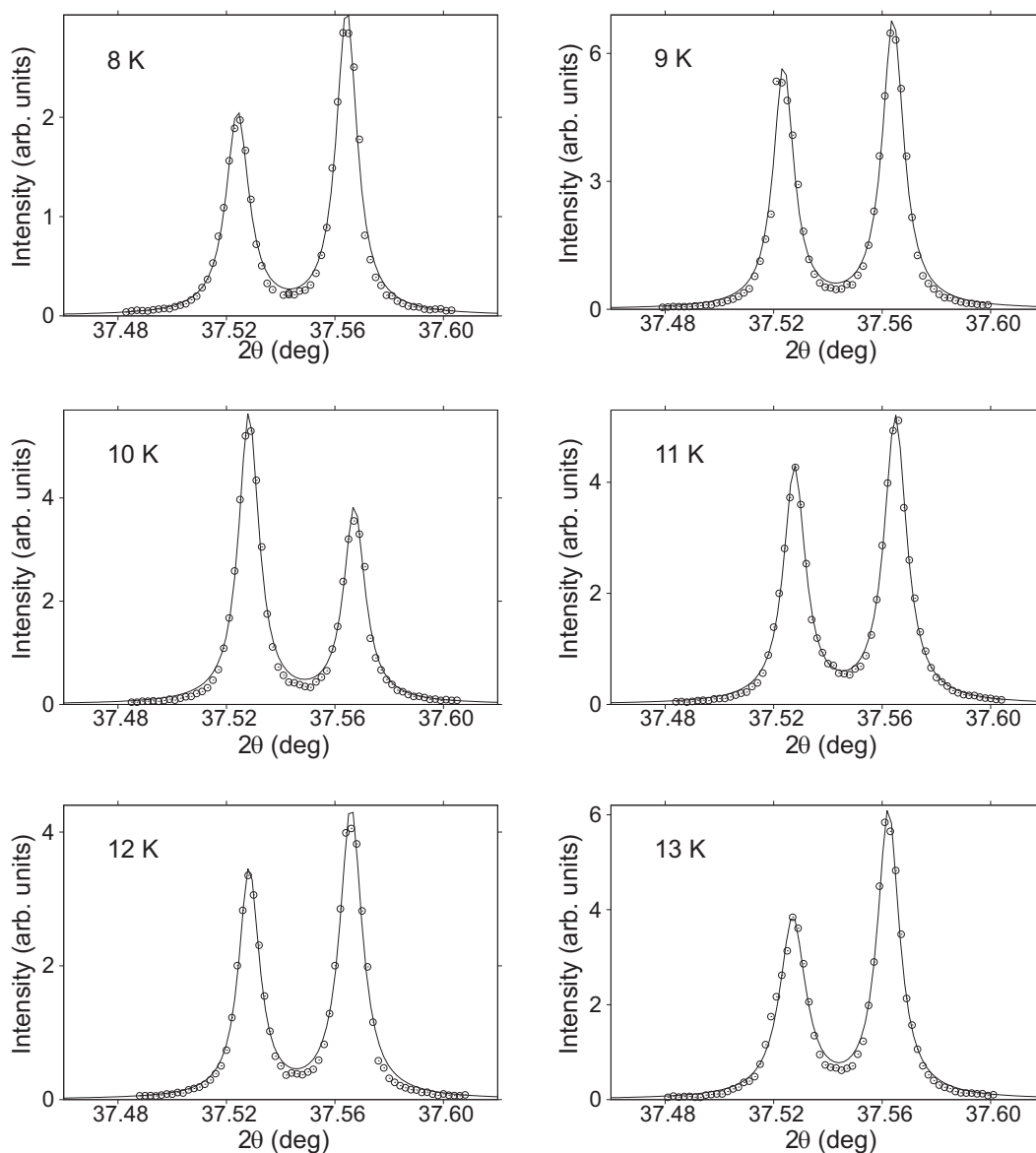


Figure E.9: ω -scans on the superstructure reflection (0 -0.5 3) for different temperatures.

E.3 Profile fitting for determination of the peak positions of CrOCl

To determine the reflection splitting the measured reflection intensities of the 2θ -dependent ω -scans were summed for equal 2θ -values. The resulting intensities plotted against the 2θ values yields a pseudo powder diagram whose profile was fitted using Lorentz functions.



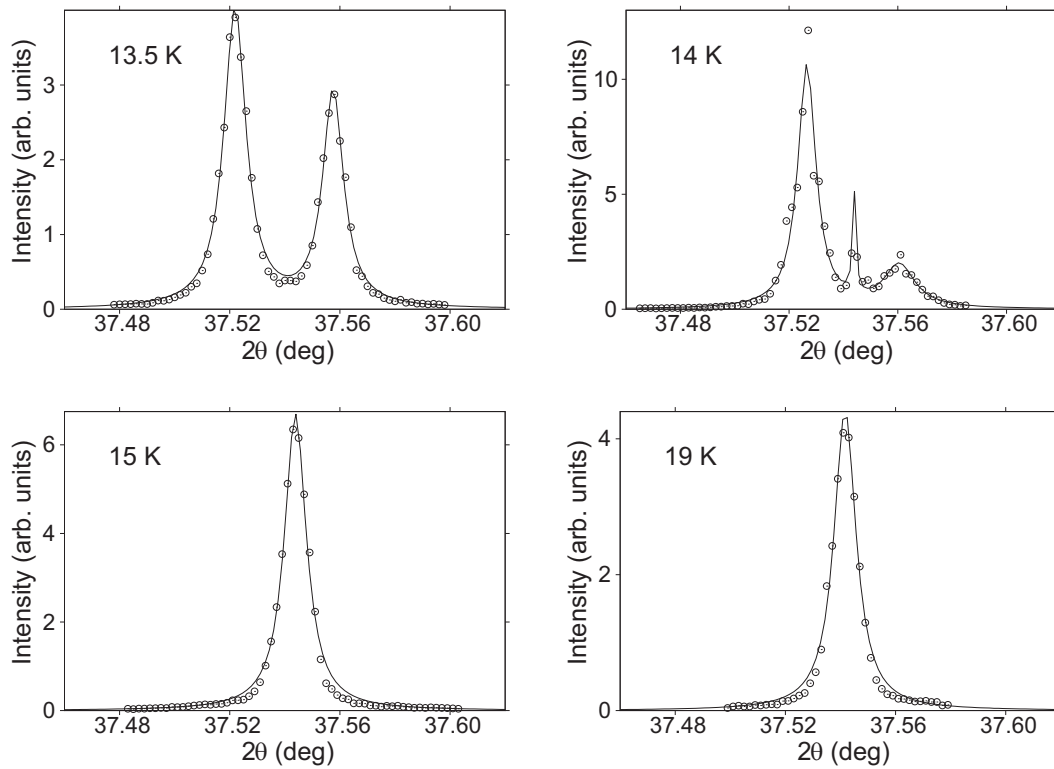


Figure E.10: Reflection profiles of reflection (0 -2 5) were derived from 2θ dependent ω -scans by summing of the reflection intensities for same 2θ values. The solid curve represent the superposed curves of Lorentz-type functions.

Appendix F

Additional structural parameters of CrOCl at different temperatures

Table F.1: Thickness of the layers (d_L) and width of the Van-der-Waals gap (d_{vdW}), as obtained from the crystal structures (Table 8.1).

T (K)	d_L (Å)	d_{vdW} (Å)
100	5.0335(13)	2.6505(13)
250	5.0367(11)	2.6698(11)
310	5.0386(13)	2.6765(13)
340	5.0385(12)	2.6822(12)

Table F.2: Selected interatomic distances (Å) and bond angles (deg) at different temperatures. Labeling of the atoms refer to the labeling used in Fig. F.1

	100 K	250 K	310 K	340 K
Cr1-Cr2 ($\times 2$)	3.1768	3.1787	3.1793	3.1796
Cr2-Cr3 ($\times 4$)	3.0032(16)	3.0044(3)	3.0047(16)	3.0052(3)
Cr1-O3 ($\times 2$)	1.973(2)	1.9741(4)	1.974(2)	1.9747(4)
Cr1-O1 ($\times 2$)	2.0258(16)	2.0266(11)	2.0285(16)	2.0266(11)
Cr1-Cl1 ($\times 2$)	2.3155(13)	2.3173(5)	2.3181(13)	2.3181(5)
Cl1-Cl3'' ($\times 4$)	3.644(2)	3.6587(6)	3.664(2)	3.6680(7)
Cl1-Cl3' ($\times 4$)	5.620(4)	5.6237(8)	5.626(4)	5.6256(8)
O3-Cr1-O3'	156.22(9)	156.23(7)	156.37(8)	156.16(7)
Cl1-Cr2-Cl2	86.63(4)	86.607(18)	86.59(4)	86.603(19)
Cr1-O1-Cr2	103.27(10)	103.30(8)	103.20(9)	103.35(8)
O1-Cr1-Cl1	85.05(5)	85.05(4)	85.11(5)	85.03(4)
O2-Cr2-Cl1	171.68(5)	171.65(4)	171.70(5)	171.63(4)

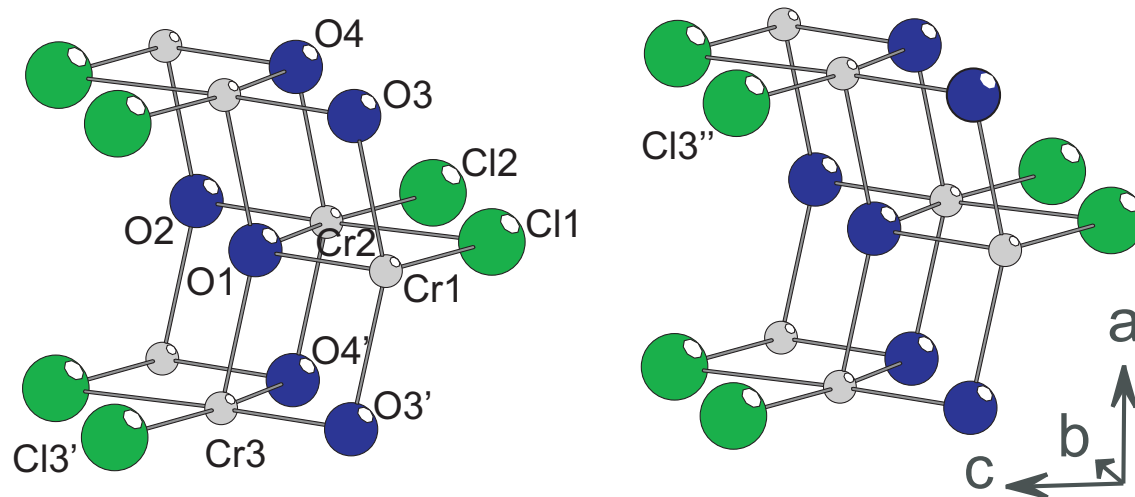


Figure F.1: Section of the crystal structure of CrOCl.

Bibliography

- Abragam, A. and Bleaney, B. (1970). *Electron paramagnetic resonance of transition ions*, Oxford University Press, Oxford.
- Adam, A. and Buisson, G. (1975). Structure magnétique cycloïdale de FeOCl, *Phys. Status Solidi A* **30**: 323–329.
- Angelkort, J., Schönleber, A. and van Smaalen, S. (2009). Low- and high-temperature structures of TiI₃, *J. Solid State Chem.* **182**(3): 525–531.
- Arndt, S. and Okuda, J. (2002). Mono(cyclopentadienyl) complexes of the rare-earth metals, *Chem. Rev.* **102**: 1953–1976.
- Aslanov, L. A., Fetisov, G. V. and Howard, J. A. K. (1998). *Crystallographic Instrumentation*, Oxford University Press.
- Babel, D. (1972). Die Verfeinerung der MoBr₃-Struktur, *J. Solid State Chem.* **4**: 410–416.
- Bailey, A. C. and Yates, B. (1970). Anisotropic thermal expansion of pyrolytic graphite at low temperatures, *J. Appl. Phys.* **41**(13): 5088–5091.
- Baker, W. A. and Janus, A. R. (1964). Magnetic properties of zirconium (III) and hafnium (III) iodides, *J. Inorg. Nucl. Chem.* **26**: 2087–2097.
- Barrera, G. D., Bruno, J. A. O., Barron, T. H. K. and Allan, N. L. (2005). Negative thermal expansion, *J. Phys. Condens. Matter* **17**: R217–R252.
- Barron, T. H. K. (1998). Generalized theory of thermal expansion of solids, in C. Y. Ho and R. E. Taylor (eds), *Thermal expansion of solids*, Vol. I-4 of *CINDAS data series on material properties*, ASM, Materials Park, pp. 1–108.

- Bochkarev, M. N. (2002). Synthesis, arrangement and reactivity of arene–lanthanide compounds, *Chem. Rev.* **102**: 2089–2117.
- Bray, J. W., Hart, H. R., Interrante, J. L. V., Jacobs, I. S., Kasper, J. S., Watkins, G. D. and Wee, S. H. (1975). Observation of a spin-Peierls transition in a Heisenberg antiferromagnetic linear-chain system, *Phys Rev. Lett.* **35**: 744.
- Brese, N. E. and O’Keeffe, M. (1991). Bond-valence parameters for solids, *Acta Crystallogr., Sect. B: Struct. Sci* **47**: 192–197.
- Brodersen, K., Breitbach, H.-K. and Thiele, G. (1968). Die Feinstruktur des Ruthenium(III)-bromids, *Z. Anorg. Allg. Chem.* **357**: 162–171.
- Brodersen, K., Thiele, G., Ohnsorge, H., Recke, I. and Moers, F. (1968). Die Struktur des IrBr₃ und über die Ursachen der Fehlordnungserscheinungen bei den Schichtstrukturen kristallisierenden Edelmetalltrihalogeniden, *J. Less-Common Met.* **15**: 347–54.
- Brown, I. D. (2002a). *The chemical bond in inorganic chemistry*, Oxford University Press.
- Brown, I. D. (2002b). *The chemical bond in inorganic chemistry, The bond valence method*, Oxford University Press, Oxford.
- Brown, I. D. (2006). *Private communication*.
- Burla, M. C., Camalli, M., Carrozzini, B., Cascarano, G., Giacovazzo, C., Polidori, G. and Spagna, R. (2001). SIR200-N, a program for large and small crystal structures, *J. Appl. Crystallogr.* **34**: 523–526.
- Chaikin, P. M. and Lubensky, T. C. (2000). *Principles of condensed matter physics*, Cambridge University Press, Cambridge.
- Chesnut, D. B. (1966). Instability of a linear spin array: Application to Würster’s blue perchlorate, *J. Chem. Phys.* **17**: 4677.
- Christensen, A. N., Johansson, T. and Quézel, S. (1975). Preparation and magnetic properties of CrOCl, *Acta Chem. Scand.* **28**: 1171–1174.
- Cofone, A. and Niemeyer, M. (2006). A monomeric, base-free samarium(III) thiophenolate with a π -encapsulated rare-earth metal, *Z. Anorg. Allg. Chem.* **632**: 1930–1932.

- Dabrowski, B., Xiong, X., Bukowski, Z., Dybziński, R., Klamut, P. W., Siewenie, J. E., Chmaissem, O., Shaffer, J., Kimball, C. W., Jorgensen, J. D. and Short, S. (1999). Structure-properties phase diagram for $\text{La}_{1-x}\text{Sr}_x\text{MnO}_3$ ($0.1 \leq x \leq 0.2$), *Phys. Rev. B* **60**: 7006–7017.
- Dahl, L. F., Chiang, T.-I., Seabaugh, P. W. and Larsen, E. M. (1964). Structural studies of zirconium trihalides and hafnium triiodide, *Inorg. Chem.* **3**: 1236–1242.
- Del Rio, M. and Dejeus, R. (1998). *XOP 2.0 software online reference manual*, 2nd edn, European Synchrotron Radiation Facility (ESRF), Grenoble, France.
- Dorhout, P. K. and Corbett, J. D. (1991). Bonding considerations in metal iodide chain compounds: A_xScI_3 and MI_3 ($\text{A} = \text{Li}, \text{Na}$; $\text{M} = \text{Zr}, \text{Nb}$), *Inorg. Chem.* **30**: 3326–3333.
- Drent, E., Emeis, C. A. and Kortbeek, A. G. T. G. (1975). The magnetic properties of linear chains in $\beta\text{-TiCl}_3$, *Chem. Phys.* **10**: 313–322.
- Duisenberg, A., Kroon-Batenburg, L. and Schreurs, A. (2003). An intensity evaluation method: EVAL-14, *J. Appl. Crystallogr.* **36**: 220.
- Edelmann, F. T., Freckmann, D. M. M. and Schumann, H. (2002). Cyclopentadienylfreie Organolanthanoidchemie, *Chem. Rev.* **102**: 18511896.
- Ehrlich, P. and Seifert, H.-J. (1959). Über Vanadinchloride, *Z. Anorg. Allg. Chem.* **301**: 282–287.
- Fausti, D., Lummen, T. T., Angelescu, C., Macovez, R., Luzon, J., Broer, R., Rudolf, P., van Loosdrecht, P. H., Tristan, N., Büchner, B., van Smaalen, S., Möeller, A., Meyer, G. and Taetz, T. (2007). Symmetry disquisition on the TiOX phase diagram ($\text{X}=\text{Br}, \text{Cl}$), *Phys. Rev. B* **75**: 245114.
- Franzen, H. F. (1990). Distortions in the D_{6h} crystal class to $a \times a\sqrt{3} \times c$ orthorhombic lattices, *J. Solid State Chem.* **85**: 173–175.
- Giacovazzo, C., Monaco, H. L., Artioli, G., Ferraris, D. V. G., Gilli, G., Zanotti, G. and Catti, M. (2002). *Fundamentals of Crystallography*, Oxford University Press.
- Giesbrecht, G. R., Gordon, J. C., Clark, D. L., Hay, P. J., Scott, B. L. and Tait, C. D. (2004). A comparative study of π -arene-bridged lanthanum arylamide and

- aryloxide dimers. Solid behavior, exchange mechanisms, and X-ray crystal structures of $\text{La}_2(\text{NH-2,6-PrCH})\text{La}(\text{NH-2,6-PrCH})(\text{THF})$, and $\text{La}(\text{NH-2,6-PrCH})(\text{py})$, *J. Am. Chem. Soc.* **12**: 63876401.
- Givens, F. L. and Fredericks, G. E. (1977). Thermal expansion of NbSe_2 and TaS_2 , *J. Phys. Chem. Solids* **38**: 1363–1365.
- Haase, A. and Brauer, G. (1975). Vanadium Oxychlorid, *Acta. Crystallogr. B* **31**: 2521–2522.
- Hargittai, M. (2000). Molecular structure of metal halides, *Chem. Rev.* **100**: 2233–2301.
- Hase, M., Terasaki, I. and Uchinoka, K. (1993). Observation of spin-Peierls transitions in linear Cu^{2+} (spin 1/2) chains in an inorganic compound CuGeO_3 , *Phys. Rev. Lett.* **70**: 3651.
- Hauber, S.-O. and Niemeyer, M. (2005). Stabilization of unsolvated europium and ytterbium pentafluorophenyls by π -bonding encapsulation through a sterically crowded triazenido ligand, *Inorg. Chem.* **44**: 8644–8646.
- Hauber, S.-O. and Niemeyer, M. (2007). π -bonding encapsulation in aryl-substituted lanthanide selenolates: monomeric compounds with apparent low-coordinate metal atoms, *Chem. Commun.* (**3**): 275–277.
- Herrendorf, W. and Bärnighausen, H. (1997). *HABITUS*, University of Karlsruhe, Giessen, Germany.
- Hillebrecht, H., Ludwig, T. and Thiele, G. (2004). About trihalides with TiI_3 chain structure: Proof of pair forming of cations in $\beta\text{-RuCl}_3$ and RuBr_3 by temperature dependent single crystal X-ray analyses, *Z. Anorg. Allg. Chem.* **630**: 2199–2204.
- Ho, C. Y. and Taylor, R. E. (eds) (1998). *Thermal expansion of solids*, Vol. I-4 of *Cindas Data series on material properties*, ASM, Materials Park.
- Hou, Z., Zhang, Y., Nishiura, M. and Wakatsuki, Y. (2003). (Pentamethylcyclopentadienyl)lanthanide(II) alkyl and silyl complexes: synthesis, structures, and catalysis in polymerization of ethylene and styrene, *Organometallics* **22**: 129–135.

- Hultsch, K. C., Gribkov, D. V. and Hampel, F. (2006). 3,3'-Bis(trisarylsilyl)-substituted binaphtholate rare earth metal catalysts for asymmetric hydroamination, *J. Am. Chem. Soc.* **128**: 3748–3759.
- International Tables of Crystallography, Volume D: Physical Properties of Crystals* (2006). International Union of Crystallography.
- Jacobs, I. S., Bray, J. W., Hart, H. R., Interrante, J. L. V., Kasper, J. S. and Watkins, G. D. (1976). Spin-Peierls transition in magnetic donor-acceptor compounds of tetrathiafulvalene (TTF) with bisdithiolene metal complexes, *Phys. Rev. B* **14**: 3036.
- Kabsch, W. (1993). Automatic processing of rotation diffraction data from crystals of initially unknown symmetry and cell constants, *J. Appl. Crystallogr.* **26**: 795–800.
- Kaupp, M. (2001). "Non-VSEPR" structures and bonding in d^0 systems, *Angew. Chem. Int. Ed.* **40**: 3534–3565.
- Klemm, W. and Krose, E. (1947). Das magnetische Verhalten der Titantrihalogenide, *Z. Anorg. Allg. Chem.* **253**: 209–217.
- Kleppinger, J., Calabrese, J. C. and Larsen, E. M. (1975). Crystal Structure of β -Zirconium Tribromide, *Inorg. Chem.* **14**: 3128–3130.
- Komarek, A. C., Taetz, T., Fernández-Díaz, M. T., Trots, D. M., Möller, A. and Braden, M. (2009). Strong magneto-elastic coupling in VOCl: Neutron and synchrotron powder X-ray diffraction study, *Phys. Rev. B* **79**.
- Krimmel, A., Strepfer, J., Bohnenbuck, B., Keimer, B., Hoinkis, M., Klemm, M., Horn, S., Loidl, A., Sing, M., Claessen, R. and Zimmermann, M. (2006). Incommensurate structure of the spin-Peierls compound TiOCl, *Phys. Rev. B* **73**: 172413.
- Lachgar, A., Dudis, D. S. and Corbett, J. D. (1990). Revision of the structure of zirconium triiodide. The presence of metal dimers, *Inorg. Chem.* **29**: 2242–2246.
- Larsen, E. M., Wrazel, J. S. and Hoard, L. G. (1982). Single-crystal structures of ZrX_3 ($X = Cl^-, Br^-, I^-$) and $ZrI_{3.40}$ synthesized in low-temperature aluminum halide melts, *Inorg. Chem.* **21**: 2619–2629.

- Lewis, J., Machin, D. J., Newnham, I. E. and Nyholm, R. S. (1962). The magnetic properties of some halides of titanium and zirconium, *J. Chem. Soc.* pp. 2036–41.
- Lin, J. and Miller, G. J. (1993). Dimensional diversity in transition metal trihalides, *Inorg. Chem.* **32**: 1476–1487.
- Lind, M. A. (1970). Refinement of the crystal structure of iron oxychloride, *Acta Crystallogr. B* **26**: 1058–1062.
- Macovez, R., Luzon, J., Schissling, J., Sadoc, A., Kjeldgaard, L., van Smaalen, S., Fausti, D., van Loodsrecht, P. H. M., Broer, R. and Rudolf, P. (2007). Hybridization, superexchange, and competing magnetoelastic interactions in TiOBr, *Phys. Rev. B* **76**: 205111.
- Maniwa, Y., Fujiwara, R., Kira, H., Tou, H., Kataura, H., Suzuki, S., Achiba, Y., Nishibori, E., Takata, M., Sakata, M., Fujiwara, A. and Suematsu, H. (2001). Thermal expansion of single-walled carbon nanotube (swnt) bundles: X-ray diffraction studies, *Phys. Rev. B* **64**(24): 241402.
- Marks, T. J. and Hong, S. (2004). Organoalanthanide-catalyzed hydroamination, *Chem. Res.* **37**: 673–686.
- Maule, C. H., Tothill, J. N., Strange, P. and Wilson, J. A. (1988). An optical investigation into the $3d^1$ and $3d^2$ transition-metal halides and oxyhalides, compounds near to delocalisation, *J. Phys. C: Solid State Phys.* **21**: 2153–2179.
- Merlino, S., Labella, L., Marchetti, F. and Toscani, S. (2004). Order-disorder transformation in RuBr_3 and MoBr_3 : A two-dimensional Ising model, *Chem. Mater.* **16**: 3895–3903.
- Murray, R. and Evans, B. L. (1979). The thermal expansion of 2H-MoS_2 and 2H-WSe_2 between 10 and 320 K, *J. Appl. Crystallogr.* **12**: 312–315.
- Natta, G., Corrandini, P. and Allegra, G. (1961). The Different Crystalline Modifications of TiCl_3 , a Catalyst Component for the Polymerization of α -Olefins, *J. Polymer Sci.* **51**: 399–410.
- Newland, B. G. and Shelton, A. J. (1970). The preparation of α - and β -titanium tribromide, *J. Less-Common Met.* **22**: 369–372.

- Niemeyer, M. (2001). σ -donor versus η^6 - π -arene interactions in monomeric europium(II) and ytterbium(II) thiolates - an experimental and computational study, *Eur. J. Inorg. Chem.* pp. 1969–1981.
- Nocker, K. and Gruehn, R. (1993). Zum chemischen Transport von CrOCl und Cr₂O₃ – Experimente und Modellrechnungen zur Beteiligung von CrOCl_{2,g}, *Z. Anorg. Allg. Chem.* **619**: 699–710.
- Ogawa, S. (1960). Magnetic Transition in TiCl₃, *J. Phys. Soc. Jpn.* **15**: 1901.
- O’Keeffe, M. and Brese, N. E. (1991a). Atom sizes and bond lengths in molecules and crystals, *J. Amer. Chem. Soc.* **113**: 3226–3229.
- O’Keeffe, M. and Brese, N. E. (1991b). Bond-valence parameters for solids, *Acta Crystallogr.* **B47**: 192–197.
- O’Keeffe, M. and Brese, N. E. (1992). Bond-valence parameters for anion-anion bonds in solids, *Acta Crystallogr., Sect. B: Struct. Sci* **48**: 152–154.
- Palenik, G. J. (1997). Bond valence sums in coordination chemistry using oxidation state independent R₀ values. A simple calculation of the oxidation state of titanium in complexes containing Ti–N, Ti–O, and Ti–Cl bonds, *Inorg. Chem.* **36**: 3394–3397.
- Palenik, G. J. (2003). Bond valence sums in coordination chemistry. The calculation of the oxidation state of samarium in complexes containing samarium bonded only to oxygen, *Inorg. Chem.* **42**: 2725–2728.
- Penson, K. A., Holz, A. and Bennemann, K. H. (1976). A theory for first order spin-Peierls phase transition, *J. Chem. Phys.* **65**: 5024–5026.
- Petricek, V., Dusek, M. and Palatinus, L. (2000). *Jana2000. The crystallographic computing system*, Institute of Physics, Praha, Czech Republic.
- Petricek, V., Dusek, M. and Palatinus, L. (2006). *Jana2006. The crystallographic computing system*, Institute of Physics, Praha, Czech Republic.
- Pollini, I. (1983). Electronic transitions in α - and β - titanium trichloride, *Solid State Commun.* **47**: 403–408.

- Redhammer, G. J., Merz, M., Tippelt, G., Sparta, K., Roth, G., Treutmann, W., Lottermoser, W. and Amthauer, G. (2007). Temperature-dependent crystal structure refinement and ^{57}Fe Mössbauer spectroscopy of $\text{Cu}_2\text{Fe}_2\text{Ge}_4\text{O}_{13}$, *Acta Crystallogr. B* **63**: 4–16.
- Saha-Dasgupta, T., Valenti, R., Rosner, H. and Gros, C. (2004). TiOCl , an orbital-ordered system, *Europhys. Lett.* **67**: 63–69.
- Schäfer, H., Huneke, K.-H. and Brendel, C. (1971). Osmium(III)-jodid, *Z. Anorg. Allg. Chem.* **383**: 49–54.
- Schäfer, H. and Wartenpfehl, F. Z. (1961). Das Chrom(III)oxydchlorid CrOCl , *Z. Anorg. Allgem. Chem.* **308**: 282.
- Schönleber, A., Angelkort, J., van Smaalen, S., Palatinus, L., Senyshyn, A. and Morgenroth, W. (2009). Phase transition, crystal structure and magnetic order in VOCl , *Phys. Rev. B* **submitted**: **bd11031**.
- Schönleber, A., Shcheka, G. and van Smaalen, S. (2008). Normal-to-incommensurate phase transition in the spin-Peierls compound TiOCl : An X-ray diffraction study, *Phys. Rev. B* **77**: 094117.
- Schönleber, A., van Smaalen, S. and Palatinus, L. (2006). Structure of the incommensurate phase of the quantum magnet TiOCl , *Phys. Rev. B* **73**: 214410.
- Schumann, H., Meese-Marktscheffel, J. A. and Esser, L. (1995). Synthesis, structure, and reactivity of organometallic π -complexes of the rare earths in the oxidation state Ln^{3+} with aromatic ligands, *Chem. Rev.* **95**: 865986.
- Seidel, A., Marianetti, C. A., Chou, F. C., Ceder, G. and Lee, P. A. (2003). $S=1/2$ chains and spin-Peierls transition in TiOCl , *Phys. Rev. B* **67**: 020405(R).
- Selwood, P. W. (1956). *Magnetochemistry, second Edition*, Interscience, New York.
- Shaz, M., van Smaalen, S., Palatinus, L., Hoinkis, M., Klemm, M., Horn, S. and Claessen, R. (2005). Spin-Peierls transition in TiOCl , *Phys. Rev. B* **71**: 100405(R).
- Sheldrick, G. M. (1998). *SADABS*.
- Software Crysalis RED* (2005). Oxford Diffraction Ltd., Abingdon, England.

- Thorne, R. E., Stum, Z., Kmetko, J., O'Neill, K. and Gillilan, R. (2003). Micro-fabricated mounts for high-throughput macromolecular crystallography, *J. Appl. Crystallogr.* **36**: 1455–1460.
- Troyanov, S. I. and Snigireva, E. M. (2000). Crystal structures of transition-metal halides TiCl_4 , $\alpha\text{-TiCl}_3$, and TiI_2 , *Russian Journal of Inorganic Chemistry* **45**: 580–5852.
- Troyanov, S. I., Snigireva, E. M., Pisarevskii, A. P., Janovskii, A. I. and Strushkov, J. T. (1994). Crystal structure of TiBr_3 , *Zh. Neorg. Khim.* **39**: 374–377.
- Trzesowska, A. (2006). Bond-valence parameters of lanthanides, *Acta Crystallogr., Sect. B: Struct. Sci* **62**: 745–753.
- Trzesowska, A., Kruszynski, R. and Bartczak, T. J. (2004). New bond-valence parameters for lanthanides, *Acta Crystallogr., Sect. B: Struct. Sci* **60**: 174–178.
- van Smaalen, S., Palatinus, L. and Schönleber, A. (2005). Incommensurate interactions and nonconventional spin-Peierls transition in TiOBr , *Phys. Rev. B* **72**: 020105(R).
- von Schnering, H. G. (1966). Zur Struktur des Titan(III)-jodids, *Naturwissenschaften* **53**: 359–360.
- von Schnering, H. G., Brodersen, K., Moers, F., Breitbach, H.-K. and Thiele, G. (1966). Strukturuntersuchungen an $\beta\text{-RuCl}_3$, RuBr_3 und RuI_3 , *J. Less-Common Met.* **11**: 288–289.
- Wiedenmann, A., Vénien, J. P., Palvadeau, P. and Rossat-Mignod, J. (1983). Magnetic ordering of the quasi-two-dimensional system VOCl , *J. Phys. C:Solid State Phys.* **16**: 5539–5350.
- Zhang, Y.-Z., Jeschke, H. O. and Valenti, R. (2008). Two pressure-induced transitions in TiOCl : Mott insulator to anisotropic metal, *Phys. Rev. Lett.* **101**: 136404.

Parts of this thesis published in the international scientific literature

Chapter 5 has been published as:

Angelkort, J., van Smaalen, S., Hauber, S. O. and Niemeyer, M.:
Phase transition and crystal structure of the monomeric
Europium(II) Thiolate $\text{Eu}(\text{SC}_3\text{H}_4)_2$.
Z. Anorg. Allg. Chem. (2007), **633**: 1031-1035

Chapter 6 has been published as:

Angelkort, J., Schönleber, A. and van Smaalen, S.:
Low- and high temperature structures of TiI_3 .
J. Solid State Chem. (2009), **182(3)**: 525-531

Chapter 7 has been submitted for publication:

Angelkort, J., Wölfel, A., Schönleber, A., van Smaalen, S. and Kremer, R.:
Magnetoelastic coupling in CrOCl .
submitted to *Phys. Rev. B*

List of Figures

2.1	Changes of the free energy at different temperatures effected by a variation of the order parameter η	7
3.1	Wavelength dependent change of the absorption coefficient of CrOCl .	13
3.2	Arrangement of crystal rotating axes in goniometers possessing κ - and Euler-geometry	15
3.3	Experimental setup at beamline D3 (DESY, Hamburg)	16
3.4	Setup of a Mach3 diffractometer	18
3.5	Crystal rotation about the ψ -axis	19
3.6	Setup of a Mar345-image plate diffractometer	21
3.7	Single-crystals of CrOCl glued on the top of a boron glass fibre and on the top of carbon fibres	23
3.8	Hygroscopic crystal sealed in a capsule containing inert gas	24
4.1	High-temperature crystal structures of α -TiCl ₃ and TiI ₃ projected parallel to the lattice direction \mathbf{c}	26
4.2	Temperature dependence of the magnetic susceptibility of α -TiCl ₃ and TiI ₃	29
4.3	MOX crystal structure	30
5.1	Asymmetric unit of the high-temperature structure of Eu(SC ₃₆ H ₄₉) ₂ .	36
5.2	Section of the diffraction pattern resulting from measurements on single-crystals of Eu(SC ₃₆ H ₄₉) ₂ at different temperatures	37
5.3	Asymmetric unit of Eu(SC ₃₆ H ₄₉) ₂ of the low-temperature structure .	38
6.1	Projection of the crystal structure of TiI ₃ along \mathbf{c} and the unit cell relations in the low-temperature phase of TiI ₃	48
6.2	Chains of face sharing TiI ₆ -octahedra in TiI ₃	49

6.3	Sections of MAR345-image plate frames obtained from measurements on TiI_3 single-crystals at different temperatures.	53
6.4	Pairing of Ti-atoms in the low-temperature structure of TiI_3	56
7.1	Crystal structure of CrOCl , view on ribbons of CrOCl	64
7.2	Magnetic susceptibility of CrOCl for a variation of temperature	66
7.3	Temperature dependence of the specific heat of CrOCl	67
7.4	Magnetization of CrOCl and its derivative with respect to the magnetic field	68
7.5	Phase diagram of CrOCl with the magnetic field applied along the crystallographic \mathbf{c} axis	69
7.6	Diffacted intensity as a function of the scattering angle 2θ and the crystal orientation ω for several reflections of CrOCl at selected temperatures	71
7.7	Diffacted intensity as a function of the scattering angle 2θ for the reflection (0 -2 5) of CrOCl at selected temperatures	72
7.8	Temperature dependent change of the monoclinic angle α in the low-temperature phase of CrOCl	72
7.9	ω -Scans on the superstructure reflection (2 -1.5 1) of CrOCl at selected temperatures	73
7.10	Schematic representation of the MO double layers in transition-metal oxyhalides projected onto the a, b -plane	75
8.1	Layered crystal structure of CrOCl	78
8.2	Temperature dependence of the relative variations of the lattice parameters of CrOCl , the thickness of the CrOCl layers and the distance between the layers	82
C.1	Reconstructed reciprocal lattice plane $hk0$ of the low-temperature phase of TiI_3	104
E.1	ω - 2θ maps of (0 -2 5) measured in the temperature range from 30 to 270 K.	108
E.2	ω - 2θ maps of (0 -2 5) measured in the temperature range from 8 to 19 K.	109
E.3	ω - 2θ maps of (2 0 4) measured in the temperature range from 60 to 270 K.	110

E.4	ω - 2θ maps of (2 0 4) measured in the temperature range from 9 to 19 K.	111
E.5	ω - 2θ maps of (2 -2 0) measured in the temperature range from 9 to 19 K.	112
E.6	ω - 2θ maps of (2 -2 0) measured in the temperature range from 30 to 270 K.	113
E.7	q-scans measured along \mathbf{b}^*	114
E.8	ω -scans on the superstructure reflection (2 -1.5 1) for different temperatures.	115
E.9	ω -scans on the superstructure reflection (0 -0.5 3) for different temperatures.	116
E.10	Reflection profiles of reflection (0 -2 5) derived from 2θ dependent ω -scans by summing of the reflection intensities for same 2θ values. . .	118
F.1	Section of the crystal structure of CrOCl showing two adjacent layers of CrOCl.	121

List of Tables

2.1	Number, specification and location of extremal points of the free energy as a function of the temperature.	8
4.1	Average metal-metal distances in selected transition-metal trihalides at room-temperature	28
5.1	Crystal parameters and refinement results for the high and the low-temperature phase of $\text{Eu}(\text{SC}_{36}\text{H}_{49})_2$	40
5.2	Selected bond lengths, bond angles, interplanar angles and intramolecular distances in the crystal structures of $\text{Eu}(\text{SC}_{36}\text{H}_{49})_2$	41
5.3	Valences of europium and sulphur in the high -and the low-temperature structures of $\text{Eu}(\text{SC}_{36}\text{H}_{49})_2$	42
6.1	Unit cell parameters of RuBr_3 and TiI_3 structure type phases	50
6.2	Experimental data of the TiI_3 structure for different temperatures	52
6.3	Structural parameters of the high-temperature TiI_3 structure	54
6.4	Relative atomic coordinates and equivalent isotropic atomic displacement parameters of the low-temperature structures of TiI_3	55
6.5	R -values of refinements of the low-temperature structure of TiI_3 at 100 K in different space groups	55
6.6	Selected interatomic distances and bond angles in TiI_3 at different temperatures	57
6.7	Atomic valences in MX_3 compounds	59
6.8	Metal-metal distances in transition metal trihalides with the RuBr_3 type crystal structure	60
8.1	Experimental details and structural data of CrOCl at four temperatures	80

A.1	Relative atomic coordinates and equivalent isotropic displacement parameters of $\text{Eu}(\text{SC}_{36}\text{H}_{49})_2$ at 122 K	92
A.2	Anisotropic displacement parameter of $\text{Eu}(\text{SC}_{36}\text{H}_{49})_2$ at 122 K	98
B.1	Anisotropic atomic displacement parameters of TiI_3 at different temperatures	102
F.1	Thickness of CrOCl layers and of the width between adjacent CrOCl layers at different temperatures	120
F.2	Selected interatomic distances and bond angles of CrOCl at different temperatures	120

Erklärung

Die Dissertation wurde von mir selbstständig und nur unter Verwendung von zulässigen Hilfsmitteln erstellt.

Bayreuth, den 13.7.2009